Design of a Surface Acoustic Wave Sensor for the Detection of Urinary Prostate Cancer Biomarkers

Maarten Zijlmans

Master Thesis
Biomedical Engineering
Delft University of Technology

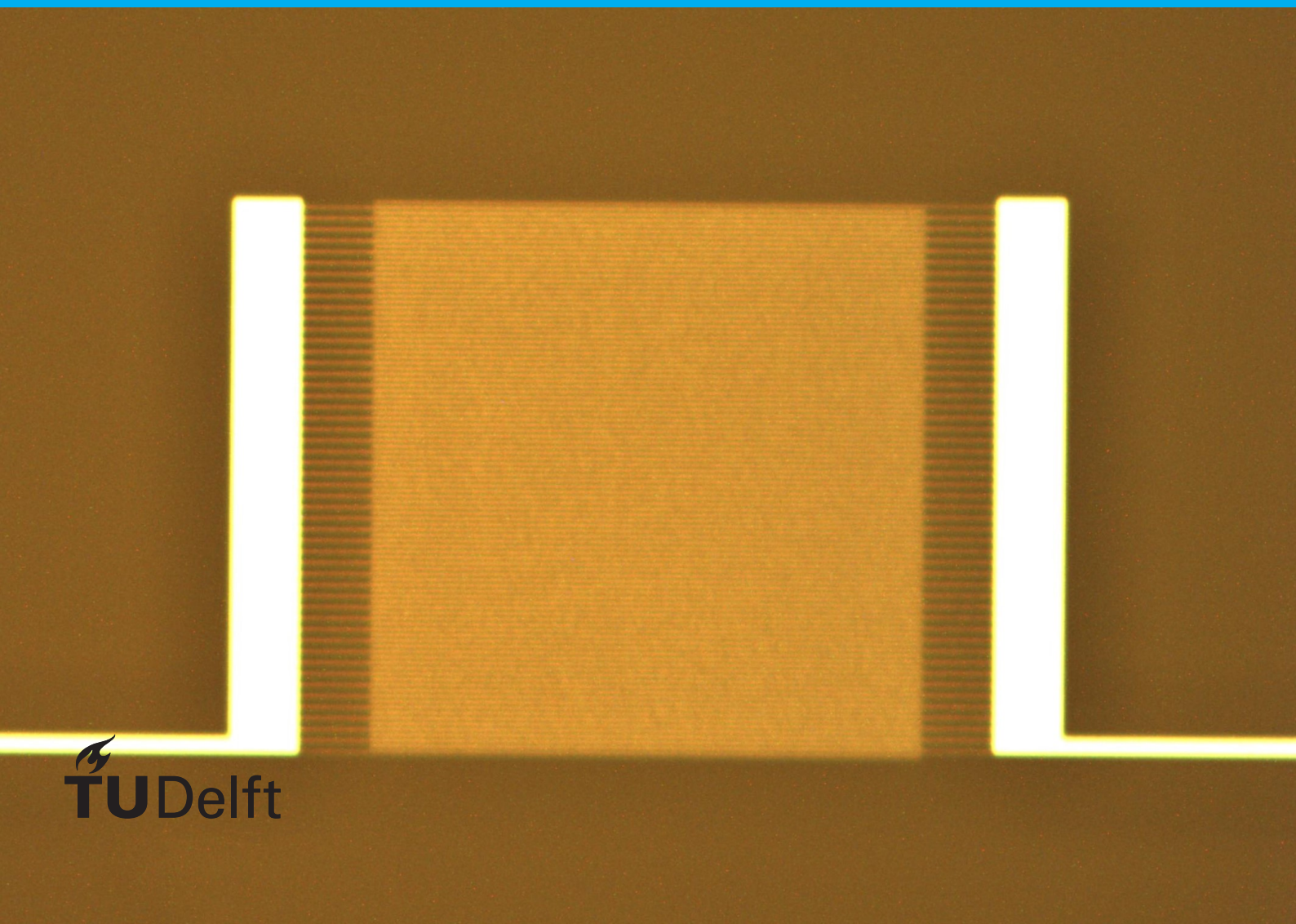

TU Delft

Design of a Surface Acoustic Wave Sensor for the Detection of Urinary Prostate Cancer Biomarkers

by

Maarten Zijlmans

to obtain the degree of Master of Science
at the Delft University of Technology,
to be defended publicly on Monday November 29, 2021 at 13:30 .

Student number:	4691717	
Project duration:	January 4, 2021 – Noveber 29, 2021	
Thesis committee:	Prof. dr. P. J. French, supervisor, chair	Bioelectronics department of Microelectronics EWI Faculty Delft University of Technology
	Assist. Prof. Dr. D.G. Muratore	Bioelectronics, department of Microelectronics EWI Faculty Delft University of Technology
	Dr. ir. E. Korkmaz, daily supervisor	Research group Smart Sensor Systems Faculty of Technology, Innovation and Society The Hague University of Applied Sciences
	Assist. Prof. Dr. A. Şişman, daily supervisor	Electrical and Electronics Engineering department Faculty of Engineering Marmara University and Nanotechnology Research and Application Center Sabanci University

This thesis is confidential and cannot be made public until November 29, 2021.

An electronic version of this thesis is available at `http://repository.tudelft.nl/`.

TU Delft

Abstract

Despite prostate cancer being the most prevalent type of cancer among males above the age of 55, national screening programs are not conducted because of the high rate of false positives this would bring. This thesis introduces surface acoustic wave sensors into the field of prostate cancer diagnosis which has the potential to measure the concentration of several biomarkers at the same time out of a single urine sample. A Love-wave surface acoustic sensor is designed to show a proof-of-concept by measuring urinary CD-9, which down-regulation is linked to the presence of cancerous prostatic tissue. Sending surface acoustic signals at the Love waves' resonance frequency throughout the substrate will change its frequency due to mass-loading on the surface. By placing CD-9 antibodies onto the surface, a frequency shift can be measured as a result of mass-loading which gives an indication of the CD-9 concentration in the urine sample. This design in this thesis consists of an ST-cut quartz piezoelectric substrate, with a PMMA thin waveguide layer on top. Furthermore, a PCB was designed for impedance matching and for connection to measurement equipment. Results showed no evidence of Love waves being visible in the output signal. Several things were tried to improve the readout of the device but due to time limitations, no redesign could be performed. Therefore several changes to improve the device for iterations are given. These include ways to change the bandwidth of the signal, decrease the attenuation in the delay line, improvements on the PCB design and simulation improvements.

Acknowledgements

While writing this thesis, I can count myself lucky to receive a great deal of support and assistance. I would like to start by thanking Erdal Korkmaz for creating and facilitating this exciting thesis subject, as well for his great enthusiasm and positive input during the meetings we had. I would also like to thank Paddy French as well for his help organizing this thesis within the TU Delft. Also, my thanks go to Alper Şişman for his great enthusiasm and the great discussions we had which truly helped to improve the design in numerous ways. I also like to say thanks to Dante Muratore, who takes the time to be a member of the thesis committee and enabling me to graduate.

Last but definitely not least, I would like to acknowledge my friends, family and girlfriend who showed great support throughout this thesis, for all the coffee breaks we took and for their helpful feedback after the numerous drafts I kept on sending.

Maarten Zijlmans
Delft, November 2021

Contents

List of Figures vii

List of Tables ix

List of Acronyms x

1 Introduction 1
- 1.1 Thesis objective . . . 2
- 1.2 Thesis outline . . . 2

2 Background 3
- 2.1 Surface Acoustic Waves . . . 3
  - 2.1.1 SAW wave types . . . 3
  - 2.1.2 Surface Acoustic Wave Biosensors . . . 5
- 2.2 State-of-the-art . . . 5
- 2.3 CD9 antibody . . . 6

3 Design Criteria 8

4 Sensor design 10
- 4.1 Materials . . . 10
  - 4.1.1 Substrate material . . . 10
  - 4.1.2 IDT material . . . 11
  - 4.1.3 Waveguide layer . . . 11
- 4.2 Sensor geometry . . . 11
  - 4.2.1 Substrate . . . 11
  - 4.2.2 IDT . . . 11
  - 4.2.3 Waveguide . . . 13
- 4.3 Determining the frequency . . . 13
  - 4.3.1 Frequency domain study . . . 14
  - 4.3.2 Eigenvalue study . . . 15
  - 4.3.3 Final design . . . 17
- 4.4 Impedance matching circuit . . . 18
  - 4.4.1 Sensor device Impedance . . . 18
- 4.5 Impedance matching and PCB design . . . 20
  - 4.5.1 LT-spice Simulation . . . 23

5 Device Fabrication 26
- 5.1 Sensor production . . . 26

6 Test Setup 28
- 6.1 Urine sample collection . . . 28
- 6.2 Test setup . . . 29

7 Results 30
- 7.1 production . . . 30
  - 7.1.1 Etching . . . 30
  - 7.1.2 Dicing . . . 31
- 7.2 Network analyzer measurements . . . 32
- 7.3 Spectrum Analyzer measurements . . . 33
- 7.4 Measurements with alternate PCB . . . 34

8 Discussion 38
8.1 Sensor Design . . . 38
8.1.1 Bandwidth . . . 38
8.1.2 Attenuation . . . 39
8.1.3 IDT design . . . 39
8.2 PCB performance . . . 39
8.2.1 Reducing RF leakage in PCB . . . 40
8.3 Simulation improvements . . . 42
8.4 Future research . . . 42

9 Conclusion 43

Bibliography 44

A Literature Review 49

B Flow Chart 84
B.1 Starting material . . . 84

C Spectrum Analyzer Results 88
C.1 400MHz input. . . . 88
C.2 900MHz input frequency . . . 88
C.3 1.4GHz input frequency. . . . 88

List of Figures

1.1 Example of a basic Surface Acoustic Wave device. The left grey comb-like structure is its input IDT, while the right is the output IDT. In between, there is a delay line through which the wave (colored black) travels. . . . 2

2.1 Representation of a Rayleigh wave, with both normal and perpendicular wave components . . . 3
2.2 Representation of a Lamb wave. Since the thickness is less than the wavelength, there is no wave energy going into the bulk . . . 4
2.3 Representation of a SH-wave, with shear components only . . . 4
2.4 Representation of a Love wave. The waveguide layer on top contains the wave to the surface . . . 4

4.1 Representation of an IDT pair. Th is the width of a single finger and λ the wavelength of the signal 12
4.3 Frequency domain study of the unit cell structure. It shows the displacement in a single point on the top surface. The blue line represents the displacement in the x-direction and the green line the displacement in the z-direction . . . 15
4.4 3D total displacement plots of the single wavelength structure eigenvalue study results. 16
4.5 3D displacement plot for every waveguide thickness and their optimal frequency 17
4.6 Representation of the full SAW sensor (not in scale) 18
4.7 Division of sections for resistance calculation: contact pad (A), contact line (B), finger connector(C), fingers (D) 18
4.8 Visualization of the capacitance between the fingers 19
4.9 Butterworth - van Dyke model representing an IDT structure 20
4.10 Schematic view of the 2 L-matching section as an intermediate step for calculating the pi-matching network values 21
4.11 Schematic view of the 2 L-matching sections with the load transformed to its parallel equivalent 22
4.12 Schematic view of the 2 L-matching sections with their calculated values for the 1-1 input design 23
4.13 Circuit representation of the sensor and its impedance network 24
4.14 AC analysis of the electrical equivalent model of the 25-500 design 24
4.15 Bandwidth extraction on the AC analysis 25
4.16 AC analysis of the electrical equivalent model of the 25-500 design with the ordered impedance matching components 25
4.17 Bandwidth extraction on the AC analysis on the 25-500 design with ordered components 25

5.1 Production steps describing the process of creating the Surface Acoustic wave sensor by micro-processing. 27

7.1 Microscope pictures of the IDT patterns after etching (before PMMA deposition) 30
7.2 Microscope pictures of overetched IDT patterns after etching (before PMMA deposition) 31
7.3 Schematic circuit of a PCB without the SAW-device connected to it. It contains the input signal (V1) the cable loads (ZL) andthe Pi-matching circuits. The circles represent the open circuit. Each PCB has to of these circuits on it, which would be able to connectto two different SAW devices independently 32
7.4 Network analyzer result of PCB without a SAW device connected to it. The grey lines represent the individual measurements of each output and the blue line shows the mean of the signals of the out and ref output respectively 33
7.5 Network analyzer results of measurements on PCB's connected to a SAW device 34
7.6 Difference of the mean signals of the network analyzer results on the PCB's with and without a SAW device 34
7.7 Two SAW devices (in the white squares), connected to the PCB 35
7.8 Peak magnitudes at 400 MHz, devided by sensor design 35

7.9 Output bandwidth at 400 MHz, devided by sensor design 36
7.10 Selection of the results of the spectrum analyzer. When a 400MHz signal is given at the input, no clear frequency shift at the output can be seen 36
7.11 A 75-500 design SAW device connected to an alternate PCB with only SMA connectors 37
7.12 Network analyzer plot with a SAW device connected to a different PCB 37

8.2 Top view of the PCB design. It shows the different traces and the ground plane that is in between them. 41
8.3 The connection between two pads which transmits the signal to the input IDT's of the two SAW devices on a SAW chip. The trace is highlighted by a green line. The red line shows an alternate path that would lead to fewer corners 41

List of Tables

4.1 Substrate material comparison 11
4.2 Different IDT designs that will be produced and tested 13
4.3 Evaluation of the different waveguide thicknesses at the frequency that creates a Love wave or, if there is one, resembles the closest to a Love wave. 15
4.4 Resistance and capacitance of a single IDT structure for each IDT design 20
4.5 Starting parameters for the calculation of the impedance matching circuit 21
4.6 Values of the pi-matching network components for each design 23

6.1 Characterization of the urine specimens 28

7.1 The yield of the produced SAW devices 32

List of Acronyms

AC	Alternating Current
BVD	Butterworth - Van Dyke
CMOS	Complementary metal oxide semiconductor
DC	Direct Current
DRE	Digital Rectal Examination
EAU	European Association of Urologists
EKL	Else Kooi Lab
ELISA	Enzyme-Linked Immuno-Sorbent Assay
FIDT	Focused Interdigital Transducer
IDT	Interdigital Transducer
FBAR	Film Bulk Acoustic Resonator
K^2	Electrochemical Coupling Coefficient
PCa	Prostate Cancer
PCB	Printed Circuit Board
PDMS	Polydimethylsiloxane
PET-CT	Positron Emission Tomography / Computational Tomography
PMMA	Poly-Methyl Methacrylate
PSA	Prostate Specific Antigen
RF	Radio Frequency
RT-FIA	Real-Time Fluorescense Immunoassay
SAW	Surface Acoustic Wave
SH-SAW	Shear Horizontal Surface Acoustic Wave
SMA	Subminiature version A (connector type)
ST	Stable Temperature
UV	Ultra-Violet

1

Introduction

Prostate cancer (PCa) is the most prevalent type of cancer in the global male population above the age of 55. There were an estimated 1 211 288 new cases worldwide in 2018 [1]. The International Agency for Research on Cancer (World Health Organization) estimates that, at the point of writing this thesis, there are 14.121 men in the Netherlands above the age of 55 that have the diagnosis of prostate cancer (14.580 in total). This makes up 26.6% of all cancer diagnoses among men [2]. Despite these alarming numbers, good and reliable testing for PCa is something that still leaves much room for improvement.

In an effort to detect cancer in its early stages of development, PSA tests are the current golden standard. Blood samples are taken from the patients and tested for the level of prostate-specific antigen (PSA) [3]. However, the effectiveness of nationwide PSA screening is under debate. A systematic study analyzed five of the biggest studies on prostate cancer screening on a cumulative 721 718 men, showing only a small effect on prostate-specific mortality (only one less death from prostate cancer per 1000 men screened over 10 years) [4].

The elevation of PSA levels is not PCa-specific and can be caused by other conditions like benign prostate hyperplasia, prostatitis and urinary tract infection, resulting in a specificity of 60% when a cut-off value of 4 ng/mL is used [5, 6]. Enlargement of the prostate, known as benign prostate hyperplasia, also elevates the blood PSA levels. False positives increase time and money going into PCa testing and create mental discomfort for patients that falsely hear that they might have prostate cancer. Furthermore, a positive PSA test requires further examination including taking biopsies, introducing new risks to the patient like infections, bleeding and erectile dysfunction [7].

As a result of the risk of over-diagnosis and over-treatment, no country decided to do public screening for PCa. Since PCa is such a prevalent cancer, there is a need for a reliable method of early detection. This thesis will focus on the introduction of a Surface Acoustic Wave (SAW) sensor into the field of testing for prostate cancer, by means of a proof-of-concept.

SAW devices are rapidly growing in the field of biosensors. Their ability to detect very small changes in mass makes it possible for them to measure on a cellular scale [8]. A general SAW device consists of a piezoelectric substrate with metal interdigital transducers (IDT) on top (figure 1.1). Applying a positive voltage potential on the input induces capacitive coupling between the fingers of the IDT, resulting in an electric field that deforms the substrate. A negative voltage potential will deform the substrate material in a different direction. Subsequently, applying an AC signal to the IDTs will create a vibration with the AC frequency within the IDT. Under the right circumstances this vibration translates to an acoustic wave that is bound to the substrate's surface, making it a surface acoustic wave.

Due to the reversible nature of piezoelectricity, the SAW will create a local electric field that can be measured by another pair of IDT's. This is considered the output of the device and contains a lot of information on the space in between the input and output IDT's, known as the delay line.

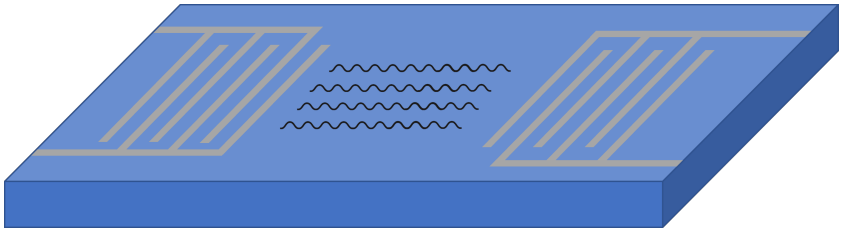

Figure 1.1: Example of a basic Surface Acoustic Wave device. The left grey comb-like structure is its input IDT, while the right is the output IDT. In between, there is a delay line through which the wave (colored black) travels.

The frequency of the acoustic wave can be interfered with at the delay line by numerous different parameters, where mass density is one of them. Attaching structures to the surface of the delay line will interfere with the vibration and consequently modify the frequency. This introduces a difference between the controlled input frequency and the measured output frequency. A bigger mass will create a bigger frequency change and will therefore indicate the presence of attached structures. This kind of usage of a SAW device is called gravitational sensing.

Besides PSA, the male urine contains several biomarkers of which the concentrations give an indication of the presence of prostate cancer [9]. Making the surface able to capture PCa biomarkers selectively out of a urine sample, increases the mass-density of the surface. A higher concentration of the biomarker increases the mass density more, resulting in a bigger frequency shift measured by the output IDT.

This thesis is partly done in collaboration with the urology department of the Erasmus Medical Centre in Rotterdam, the Netherlands. They have collected urine samples in their research in prostate cancer diagnosis and investigated the possibility to use urinary CD-9 as a biomarker. CD-9 is a transmembrane glycoprotein, present in nearly all cells in the human body [10]. Several studies have shown that down-regulation of urinary CD-9 can be used as an indicator for the presence of prostate cancer [11, 12]. Interested in the possibilities that a SAW device for prostate cancer diagnosis can bring, they offered the urine samples to show a proof-of-concept on the detection of the amount of CD-9 in urine.

1.1. Thesis objective

The aim of this thesis is to show, by means of proof-of-concept, that surface acoustic wave sensors are able to detect urinary prostate cancer biomarkers (specifically CD-9) through gravitational sensing.

1.2. Thesis outline

This thesis will start with a chapter on the background of this topic, going more in-depth on what SAW devices are and the state-of-the-art on PCa detection. Chapter 3 will lay out the design criteria that our sensor will have to adhere to, after which the design process itself will be described in chapter 4. The fabrication of the resulting sensor design is described in chapter 5 and the test setup in chapter 6. The results of the experimental data that will have to prove the concept of a Love-mode SAW sensor for the detection of CD-9 in urine is shown in chapter . Finally, Chapter 8 and 9 will discuss the results, describe the room for improvement and will conclude this thesis.

2

Background

2.1. Surface Acoustic Waves

Surface Acoustic Waves, or SAW waves, are a subclassification of acoustic waves [13]. Waves that belong to this group have the property that they are confined to the surface of a material, rather than distributed throughout the bulk as well. The frequency of a wave on a surface is sensitive to the mass density of that surface since the wave speed of a material is influenced by its density. For a fixed wavelength, this translates to a change in frequency by:

$$f_r = \frac{c}{\lambda} \tag{2.1}$$

Here, f_r is the materials resonance frequency, c the wave speed in the material and λ the wavelength of the SAW. A change in density of the material will alter the wave speed changing the frequency of the wave traveling through the material. This change can be measured and will indicate a change in mass. This effect is known as gravimetric sensing. If instead of a surface acoustic wave a regular bulk acoustic wave is used, only a small portion of the wave energy will be influenced by a change in mass density on the surface making it much harder to detect.

Common SAW wave modes for sensor applications are Rayleigh, shear-horizontal, Lamb, Love waves, where the latter two are adaptations of the first two respectively [13]. The choice on what wave type to use has been made prior the start of this thesis. A more elaborate explanation of the benefits of each wave type can be reviewed in the literature study (appendix A). Here, a summary will be given.

2.1.1. SAW wave types

When considering SAWs for sensing applications, usually Rayleigh mode waves are used. Rayleigh waves travel near the surface of solids and have components both longitudinal and perpendicular to the direction it advances, making the waves somewhat elliptical (figure 2.1). They are generally speaking considered easy and cheap to produce [13].

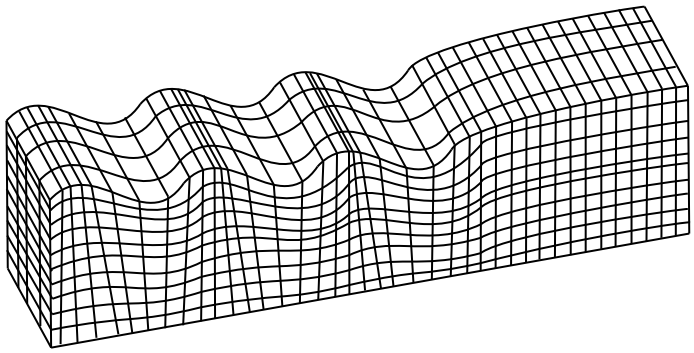

Figure 2.1: Representation of a Rayleigh wave, with both normal and perpendicular wave components

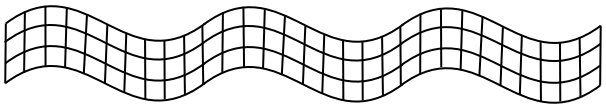

Figure 2.2: Representation of a Lamb wave. Since the thickness is less than the wavelength, there is no wave energy going into the bulk

Lamb waves are similar to Rayleigh waves in the sense that they both have wave components longitudinal and perpendicular to the propagation direction. The difference between the two is that a Lamb wave is traveling through a material that has a thickness typically 5% or less of the wavelength [14]. This allows for more energy to be at the surface of the material, making it more sensitive for gravitational sensing (figure 2.2).

However, both Rayleigh and Lamb waves are not suitable for liquid sensing [14]. The wave components that are normal to the surface interfere with liquids cause high attenuation of the wave. Since the aim of this study is to sense biomarkers in urine, the choice was made to exclude Rayleigh and Lamb waves as potential wave modes for this device.

Shear-horizontal (SH) waves, other than Rayleigh and Lamb waves, have only one wave component which is transversal to the direction of propagation (figure 2.3). This allows for much better performance when sensing in liquids, but a downside of SH waves is that a considerable amount of the wave is dissipated to the bulk of the material. This problem is largely solved when making Love waves (figure 2.4). Adding a layer with a lower phase velocity than that of the substrate onto the surface, creates a Love-wave that is tightly confined to the surface. This allows for the energy of the wave to be in a very small volume, making it highly sensitive for gravitational sensing applications [15].

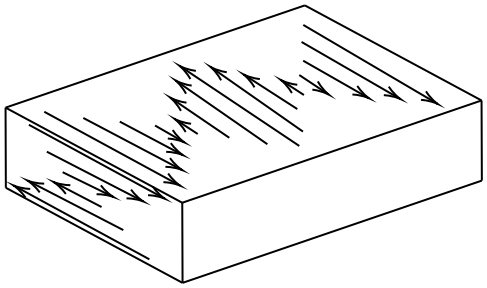

Figure 2.3: Representation of a SH-wave, with shear components only

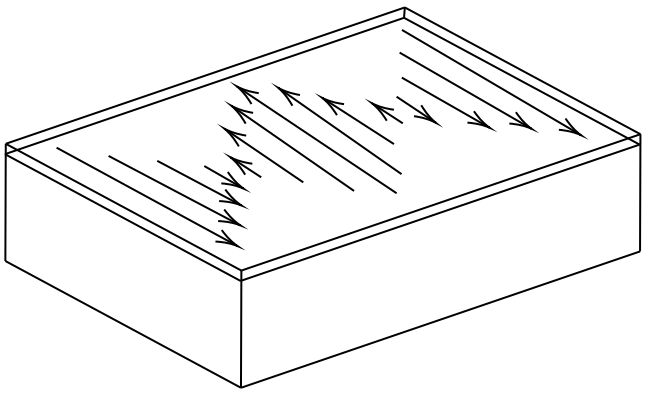

Figure 2.4: Representation of a Love wave. The waveguide layer on top contains the wave to the surface

2.1.2. Surface Acoustic Wave Biosensors

In the literature, there are numerous surface acoustic wave devices used for biosensing applications. Wang et al. [16] designed a SAW device, for the quantification of cancerous cell growth. They used a 36° $LiTaO_3$ piezoelectric substrate, a ZnO thin film and a PDMS top layer which was exposed to oxygen plasma for increased bonding. Interestingly enough, they report on producing an SH-SAW device, while they are in fact making a Love-wave device. They seem to be unaware of this but do state that they measured a sensitivity that was four times higher compared to a bare $LiTaO_3$ device they produced in an earlier study. This higher sensitivity is explained by the fact that $LiTaO_3$ has a higher shear wave velocity than ZnO, which effectively causes the wave to be almost fully caught in the thin ZnO layer.

They also designed a custom oscillatory circuit with the claim that it offered higher stability and sensitivity compared to a network analyzer. Detection of the output frequency was done by including a digital frequency counter. With this setup, they were able to measure cells in a concentration of >12.500 cells per 100 µL.

A different study, conducted by Zhang et al. [17] created a Love-wave device to detect PSA from a PBS buffer. They used a $LiTaO_3$ piezoelectric substrate as well, but with a SiO_2 waveguide layer. Since silicon dioxide is not able to immobilize biomolecules, a 50 nm gold film was added. They reported good PSA detection between 10 ng/mL to 1 µg/mL.

FBAR devices Besides SAW devices, some studies investigated the possibility of using film bulk acoustic wave resonators (FBARs) as a biosensor. FBARs are similar to SAW devices in the sense that it excites a piezoelectric substrate in a certain frequency and measure a shift in this frequency as a result of surface mass-loading to detect the presence of small particles in a sample. However, where a SAW device has interdigitated electrodes placed on top of the piezoelectric bulk, an FBAR device has two electrode plates on either side of the bulk.

Generally speaking they can be used with much higher frequencies (increasing their sensitivity) and have a much smaller footprint than typical SAW devices. The disadvantages are that they are much more difficult to fabricate, have higher fabrication costs, have increased noise and a reduced Q factor [13]. For example, Chen et al. [18] showed that FBARs can be used as a biosensor by detecting IgE antigen on its surface for the application of allergy diagnosis. They used AlN as a piezoelectric material for creating the vibrations, sandwiched between two Pt/Ti electrodes. On the backside they used an Au/Cr layer to attach biochemical components to. Their results showed a device with an electromechanical coupling coefficient of 3.18% and a sensitivity of 1.425×10^5 cm^2/g or 7.02 µg/cm^2.

2.2. State-of-the-art

To accurately describe the relevance of introducing a new type of sensor into the field of prostate cancer diagnosis, first the current state-of-the-art will be shortly described.

Digital Rectal Exam One of the first steps taken when testing for prostate cancer is a Digital Rectal Exam. A doctor palpates the prostate through the rectal opening to determine if the prostate feels firm, has hard nodules or if it has an unusual shape [19]. However, prostate cancer could also produce no physical signs. In a systematic review conducted in 2018 by Naji et al. [20], it was reported after evaluating 7 independent studies with a total of 9241 patients that DRE has a sensitivity between 36%-67% and a specificity between 41%-76%. They explain these low numbers not only by the different causes of prostate enlargement but also by low inter-examiner reliability, especially under non-urologists. They also include insufficient training and physicians feeling unconfident to detect prostate nodules by DRE in Canada, but there is no study confirming that this is also the case in the Netherlands. Therefore DRE on itself should never be used as the single indicator for the presence of prostate cancer and should always be done in combination with different tests.

Prostate Biopsy The current golden standard on prostate cancer diagnosis is a prostate biopsy [21, 22]. A piece of tissue is removed from the prostate using a hollow needle for further examination in the lab. The pathologist will look at the tissue through a microscope to assess if it is cancerous. Although it is the most reliable method for PCa diagnosis, it also introduces risks for the patient. Loeb et al. performed a systematic

study investigating the complications related to prostate biopsy. They found that the frequency of hospitalization as a result of infection after prostate biopsy ranges between 0 and 6.3% [23]. Other complications include internal bleeding, pain and urinary retention. Since prostate biopsy is the only method to accurately diagnose PCa, these are acceptable risks but it does indicate the need for a less invasive method of PCa diagnosis.

PSA: sandwich ELISA The most common and well-known test to determine the presence of prostate cancer is detecting PSA levels in the blood. PSA is a protein with the function to cleave semenogelins in the seminal coagulum. It is produced primarily in the prostate ductal and released into the lumen, where it is stored until ejaculation. PSA is also produced in other glands throughout the body but at nearly undetectable levels. This makes the protein highly specific to the prostate (hence the name prostate-specific antigen) [24]. A healthy prostate has its cell linings at the wall structured and well ordered. A little bit of PSA leaks through this barrier into the bloodstream, but not a lot.

When PCa is present, this barrier is disrupted and allows for more PSA to be secreted into the peripheral circulation. This increases the PSA concentration in the blood which is why it is considered a biomarker [24].

The golden standard for the detection of PSA in serum is sandwich ELISA (Enzyme-Linked ImmunoSorbent Assay). Invented by Evan Engvall and Peter Perlmann [25]. This method of detection starts with a polymer microtitre plate that is prepared to selectively immobilize the PSA antibody. The antibody is diluted in a coating solution and coated on the wells. The coating solution blocks the well surface from immobilizing particles in laters steps, allowing for the antibody to be the only particle that can capture things. Next, the blood samples are added to the wells such that the antibodies capture the PSA. The rest of the blood samples is then washed away with a wash buffer. To detect how much PSA is captured, detection antibodies are added. These will be captured by the surface PSA and will allow for further binding in the net steps. Depending on the used detection antibodies, it is also possible that a color-changing enzyme is already connected to the antibody. For the ones where this is not the case, usually has a biotin protein is connected to the antibodies. Biotin creates one of the strongest connections in biochemistry with streptavidin. If this method is used, the streptavidin will have a color-changing enzyme connected to it. Now, adding a color reagent gives color to the well sites where PSA is bound. The more PSA is captured, the more clear this color is which can be used to interpret the PSA concentration in the blood sample.

ELISA tests are widely used for their simplicity and high specificity and sensitivity since antigen-antibody reactions are used [26]. However, ELISA is labor-intensive and expensive to prepare the antibody

Imaging techniques One way of diagnosing and investigating PCa is by the means of imaging techniques. Transrectal ultrasound, MRI and PET-CT. Schiavina et al. [27] conducted a literature study on the state-of-the-art imaging techniques related to prostate cancer. Methods like transrectal ultrasound, MRI, PET/CT are described in their paper. All of the imaging techniques show low sensitivity when it comes to diagnosing someone with prostate cancer. However, the power of imaging is much more apparent in the staging of an already established cancer. Here parameters like the size and topology of a tumor are of importance when determining the risks of the cancer. Imaging techniques are also very useful for re-staging PCa after treatment to assess its effectiveness.

2.3. CD9 antibody

CD9 is a transmembrane glycoprotein that belongs to the tetraspanin family [10]. There are at least 33 distinct tetraspanins, which are involved in physiological and pathological processes related to fertility, cellular adhesion, motility and tumor invasion [28]. CD9 in, particular, plays an important role in the myelination of peripheral nerve cells and sperm-egg fusion [10]. On top of that, CD9 has been identified as an inhibitor for the spread of cancer [28].

CD9 is present in nearly all human cells and tissues. However, its expression is down-regulated in the prostates cancerous tissue. In a study done by Wang et al. [12], 167 primary tumor protein samples were collected and examined using western blotting. They showed a significant inverse correlation between CD9

expression and PSA level at diagnosis, tissue differentiation, pathological stage and the metastasis status of the tumor. This inverse correlation is especially apparent in metastatic prostate cancer.

In contrast to PSA blood levels, benign prostate hyperplasia does not influence the expression of CD9. In the same study conducted by Wang et al. [12],

normalization for prostate fluid volume When measuring the amount of CD9 in urine, it needs to be taken into account that the amount of prostatic fluid that is dissolved in the urine varies with each urination. Therefore some form of correction needs to be used. A common way to increase the amount of prostatic fluid in urine is by first performing a prostatic massage to drain fluid in the urethra and collecting the first portion during urination. A high prostatic fluid to urine ratio will increase the concentration of biomarkers in the sample and will increase the sensitivity of the test.

The aim of this thesis is to show a proof-of-concept of using a SAW-sensor to detect the presence of prostatic tumors by measuring the concentration of a certain biomarker in urine. To show this, CD9 will be used, but it has the potential of measuring the concentration of any protein for that matter. EN-2 is another example of a protein where studies show the great potential of using it for the detection of prostate cancer and is also able to be immobilized on the surface of a SAW sensor [29–31]. Proving that the sensor can detect CD-9 concentrations out of urine, will indicate that other biomarkers can be detected as well. This opens up the possibility that a single SAW sensor can measure multiple biomarker concentrations in a matter of seconds. Investigating this, however, is out of the scope of this thesis

As with any PCa biomarker except for PSA, CD9 is yet to be accepted as a suitable marker. Proving that CD9 is appropriate to use as a biomarker is not in the scope of this thesis. Therefore urinary samples with known CD9 concentrations will be used, to prove that the sensor shows different results with different CD9 concentrations. Determining what biomarkers are suitable for PCa diagnosis is not in the scope of this thesis and is left for others to research.

3

Design Criteria

Resonant frequency: at least 100 MHz The most important characteristic of our device is its sensitivity to changes in mass on the surface. The sensor needs to be able to measure very small changes in mass in the range of nanograms and the sensor will have to be sensitive enough to distinguish between delay lines with or without the biomarker being present. Since the device will measure changes in frequency as an effect of changes in mass, the best way to ensure high sensitivity is to have a high resonant frequency.

Usually, the frequency is determined by the weight and concentration of the measurand. However, CD9 is a transmembranous protein which means that if you capture the CD9 you will capture the cell it is attached to as well. The diameters of these cells range from 30 - 10 000 nm making it difficult to exactly determine the minimum frequency. Therefore the minimum frequency will be determined by looking at other similar studies. Good performing SAW biosensors have their resonance frequency in the range of tens to hundreds of MHz with good results [16, 32–34]. This device will therefore also measure in this range and the minimum resonance frequency in this design is 100 MHz.

Specific Adhesion of CD-9 Since the sensor will indicate the presence of CD-9 as a result of a change of mass on its surface, it is important to make sure that the adhesion process is specific to CD-9. If other proteins or cells are captured as well, the sensor will overestimate the amount of CD-9 on its surface resulting in false results.

Bandwidth: 10 MHz The goal of the SAW device is to measure the difference between input and output frequency due to the mass loading effect. In order to get results that can be interpreted, a low input and output bandwidth is necessary. If the bandwidth at the output is large compared to the frequency shift, too much of the wave energy will be spread out at other frequencies, attenuating the signal at the desired frequency. On the other hand, a bandwidth that is too small results in a very limited measurable frequency difference.

Based on similar Love-wave device designs, the expected frequency shift due to mass loading will be in the order of several MHz [35–37]. Therefore, the Love wave device should have an output bandwidth of 10 MHz.

Able to create Love-mode waves Love-mode waves are known to have very high mass sensitivity due to their characteristic of having most of the wave's energy at the surface of the device [13]. Love waves are created when a Shear-Horizontal wave is excited in a piezoelectric substrate with a thin guiding layer on top. This layer must have a lower shear phase velocity than that of the substrate [38]. In the literature study, the choice has been made for an ST-cut quartz substrate and PMMA guiding layer, with a shear phase velocity of 5099 m/s and 1100 m/s respectively. However, the thickness of the waveguide layer is also a very important parameter to create Love-mode waves. The shear phase velocity of the Love wave (v_L) depends that of the substrate (v_o) and of the guiding layer (v_g) and varies between these two depending on the thickness of the guiding layer ($v_g < v_L < v_s$) [13]. Thick guiding layers will decrease the velocity of the Love wave, resulting in a frequency drop that affects the sensitivity. Thin guiding layers result in Love wave velocities that are close to that of the substrate which will decrease the frequency drop when CD-9 is attached to the surface, decreasing

the sensitivity of the device. Too thin guiding layers will have trouble capturing the wave which will result in a wave that diffracts into the bulk, decreasing the sensitivity as well [36].

Selective surface adhesion of CD9 Surface Acoustic wave sensors are able to measure a change in surface mass by noticing a change in frequency. However, in order for our sensor to be useful, we need to be able to selectively adhere CD-9 to the surface. This asks for careful design of the biochemistry that will allow us to do that.

Affordability Another design criterion is that the sensor is affordable. Since it measures the number of biomarkers that are caught by the antibodies, the SAW device can only be used for one urine sample. If expensive materials and processing steps are being made, the use of such a device will be too expensive. A cheap solution is therefore preferable, although not of high importance for this proof-of-concept.

Producible in the Else Kooi Lab For this thesis, the prototype will be produced in the Else Kooi Lab of the TU Delft. It is therefore necessary that the processing steps can be done with the materials and equipment available.

4

Sensor design

This chapter will focus on the design of the Love-mode SAW sensor. A top-down approach will be used. By first creating a general outline of how the device will be built, the choices on further details will be made correspondingly. A large portion of the sensor design and the choice of materials have been covered in a prior literature study, which can be seen in appendix A. A summary of these findings will also be covered here.

4.1. Materials

As discussed in chapter 2, the sensor will use a Love wave mode for sensing. This means it will consist of a piezoelectric substrate, an IDT metal structure and a waveguide layer on top. The shear-horizontal wave excited by the IDT in the substrate will be captured in the waveguide layer, creating the Love-mode wave.

4.1.1. Substrate material

Often used piezoelectric materials are $LiTiO_3$, $LiNbO_3$ and ST-cut quartz. The most important property that the substrate material should have is that it is able to create Love-waves. For this to happen, the shear wave velocity of the substrate should be higher than that of the waveguide. The highest shear wave velocity is that of ST-cut quartz (5050 m/s), followed by$LiNbO_3$ (4800 m/s) and $LiTaO_3$ (4200 m/s). However, ST-cut quartz is the only material that is able to make pure shear waves which allows it to lose the least amount of wave energy into the liquid, increasing efficiency and sensitivity [39].

Another important substrate material parameter that is needed to create efficient Love waves, is the electromechanical coupling coefficient [40]. The electromechanical coupling coefficient is a measure that is defined by the transformation ratio from mechanical to electrical energy. The higher this number is, the more efficient this conversion is. For ST-cut quartz, this is very low: 0.12% [41]. For $LiNbO_3$ it is 16 % and for $LiTaO_3$ it is 5%

One more thing to take into account when using piezoelectric materials as a medium for a wave is that the temperature of the material will affect the frequency of the wave. The amount of the change in frequency as a function of temperature is represented as the temperature coefficient of frequency (TCF) as is measured in ppm/K. It is beneficial to keep this number as low as possible to maintain consistent results, despite the temperature of the room. ST-cut quartz (stable temperature quartz) has an extremely low TCF of 0.0025 ppm [42]. $LiNbO_3$ has a TCF between 70 and 95 ppm/K and for $LiTaO_3$ it is 18 and 32ppm/K [8].

A comparison of the comparison between the different substrate materials is shown in table 4.1. Despite ST-cut quartz having a low electromechanical coupling coefficient, the shear wave velocity is high compared to the other materials. This will lead to a more efficient Love-wave creation. Another big advantage is that ST-cut quartz is insensitive to temperature differences. Finally, it is the only material that produces a pure shear wave [13]. As described in chapter 2, this increases performance in liquid sensing. Therefore the choice was made to use ST-cut quartz as a substrate material.

Table 4.1: Substrate material comparison

Material	Electromechanical coefficient	Shear wave velocity [m/s]	TCF [ppm/K]
ST-Quartz	0.12	5050	0.0025
$LiNbO_3$	16	4800	70-95
$LiTaO_3$	5	4200	18-32

4.1.2. IDT material

The IDT structure will apply an alternating electrical field across the substrate. While the geometry of the IDT is very important for the performance of the device, the used material is of lesser importance. Properties it should have is that it has low resistance and can be deposited on top of the quartz substrate, but most metals are able to do this.

A widely used material for SAW IDT is aluminium. It has low resistivity ($2.65\,\mu\Omega\cdot cm$), has good corrosion resistance and is low in cost [38]. Although copper has a lower resistivity ($1.68\,\mu\Omega\cdot cm$), this material is in the EKL cleanroom considered as a contaminant. Using this will increase the difficulty of fabrication and is therefore dismissed as an option. Therefore aluminium will be the choice as the IDT material.

4.1.3. Waveguide layer

The waveguide layer has two functions. First of all, it captures the shear horizontal wave emitted by the quartz substrate to increase the device's sensitivity [38]. The most important parameter for this to be done efficiently is the shear wave velocity. To convert shear horizontal waves into Love-mode waves, it has to have a lower shear wave velocity compared to that of the piezoelectric substrate [36]. Second, the waveguide layer will also be used to immobilize biomolecules. Some studies deposit another material like gold on top if the used waveguide material does not allow for good adhesion, but this will not be done here to maintain design simplicity [43]. Therefore the waveguide material needs to be chosen in such a way that it has also good adhesion to biomolecules. Materials the are often used for the waveguide are PMMA, silicon dioxide and zinc oxide [13, 38].

Zinc-oxide is a very good material as a waveguide. It has a low shear wave velocity (2650 m/s). However, it is considered a CMOS contaminant and is not allowed to use in the cleanroom and will therefore not be further considered as a viable option for this thesis. Silicon dioxide is often used as another waveguide material but has the disadvantage that because of its dielectric constant, it losses a lot of its acoustic energy when in contact with liquids. Since we are trying to measure urinary solvents, this is too much of a disadvantage and will therefore not be used as our waveguide material.

PMMA however, is much more suited for our applications. It has a very low shear wave velocity (1100 m/s) and has very good adhesion to biomolecules. PMMA is often used as a material for the wells in ELISA tests, which use similar adhesion steps. Therefore, PMMA will be used as the waveguide material of the SAW sensor.

4.2. Sensor geometry

4.2.1. Substrate

The substrate will be made out of an ST-cut quartz wafer. The lab where the devices will be produced is best equipped to handle 4-inch wafers. The wafers that will be used for production are therefore 4 inch, 500 ± 25 µm, 2-side polished, ST-cut quartz wafers from MicroChemicals. The actual thickness is not that much of importance, since we are creating a surface-bound wave which amplitude will dissipate with increasing thickness. It has to have a thickness of at least multiple wavelengths, which means that this wafer will be more than enough.

4.2.2. IDT

When designing interdigital transducer structures for SAW applications, four primary design parameters need to be taken into account: the number of fingerpairs, the finger width, the aperture (overlap) of the fingers and the delay line length [44].

Number of finger pairs Generally speaking, increasing the number of finger pairs will increase the amplitude and limit the bandwidth of the wave. But, according to Wu et al. [45] the amplitude of the wave will not significantly increase after 120 fingerpairs. Having to many fingers increases the mass density at the surface which will eventually decrease the mass-sensitivity of the sensor. Recommended number of finger pairs are between the 20 and 100 [38]. Since it is yet unclear how many finger pairs will be the most effective for the device designed here, three different designs will be used with 25, 50 and 75 finger pairs.

Finger width EKL's lithography technology has a resolution of 1 micrometer. In this study, the fingers will have a width of 2 µm to increase the quality of the fingers while still maintaining a small wavelength. Since one of the fingerpairs consists of 2 fingers and 2 empty spaces with the same distance, the wavelength of the SAW device will be 8 µm (figure 4.1).

Aperture The aperture is the amount of overlap finger pairs. It determines the width of the wavefront traveling through the delay line. With a sufficient aperture, the wavefront can be considered to be a straight line. At the edges it rounds off, reducing the efficiency of the wave. Therefore a large aperture needs to be chosen, relative to the wavelength. To create a good wavefront, the aperture needs to be at least 20 times λ [46]. The size of the aperture also affects the capacitance of the IDT. The larger the capacitance, the more efficient the power transfer from the electrical to the mechanical (acoustic) domain. However, having a too large capacitance will create a cutoff frequency below the resonance frequency of the sensor. A finger aperture of 50 times is deemed sufficient to use as an aperture.

Delay line This is defined as the distance between the input and output IDT. Too large of a delay line will attenuate the wave too much, causing the output IDT to receive a signal with a very low magnitude. However, having a large delay line will increase the surface over which captured antibodies will affect the frequency of the wave. To find the appropriate balance between having a signal with low attenuation on the amplitude and allowing for enough antibodies to be captured, three different delay line lengths will be produced and measured.

IDT thickness For the thickness of the aluminium IDT, a balance must be found between low electric resistance and low weight to avoid acoustic interference. Usually, a thickness between 100 nm and 200 nm is used [38]. However, since a layer of PMMA will be spin-coated on top, it would be better to get a thinner layer to increase the chances of a homogeneous layer without any shadowing effects. Therefore the aluminium IDT thickness will be 50 nm.

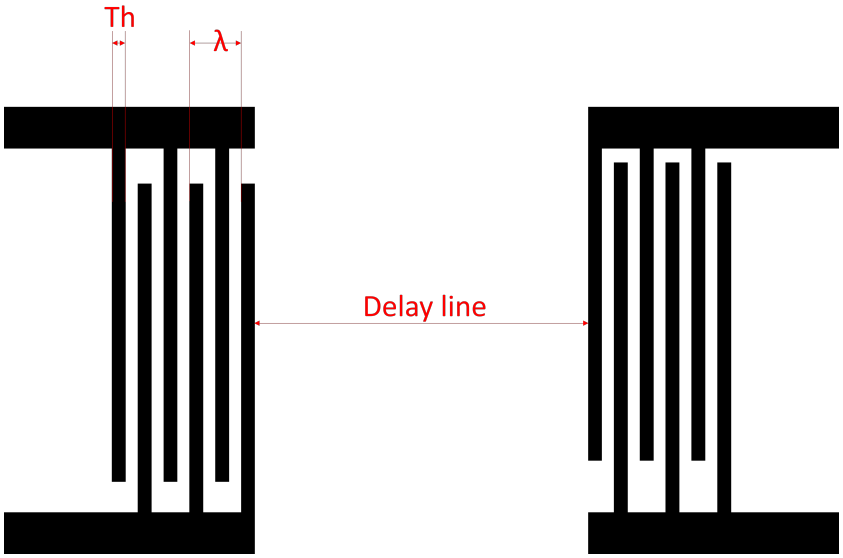

Figure 4.1: Representation of an IDT pair. Th is the width of a single finger and λ the wavelength of the signal

Several papers reported on a Focused Interdigital Transducer structure (FIDT) which has concentric fingers which focus the wave to a point at half the delay line length [47–49]. This structure compresses the

acoustic wave and increases the sensitivity of the device. This has not been used for Love wave excitation yet and to investigate the potential increase in sensitivity, this study will also include one FIDT design. Based on a study conducted by Wu et al. [47], the fingers will overlap in an angle of 25 degrees and have a focal length of 500 µm.

In total 10 different IDT designs will be produced and tested. The different parameters and coding of each design are shown in table 4.2.

Table 4.2: Different IDT designs that will be produced and tested

Design code	**Number of finger Pairs**	**Delay line length** [µm]
25-500	25	500
25-1000	25	1000
25-5000	25	5000
50-500	50	500
50-1000	50	1000
50-5000	50	5000
75-500	75	500
75-1000	75	1000
75-5000	75	5000
FIDT	25	1000

4.2.3. Waveguide

Choosing the thickness of the waveguide is an important part of the Love wave sensor design and needs careful consideration. The conversion of an SH-wave to a Love wave is heavily dependent on having a waveguide that is thin enough that as little energy as possible goes lost into the bulk of it. On the other hand, it can't be too thin since that would decrease the phase velocity throughout too much.

Gizeli, et al. have studied the effect of different PMMA waveguide thicknesses on a quartz substrate [50]. Their study showed that a waveguide thickness of around 0.2 times the wavelength gives the best results in terms of signal attenuation and change in operating frequency. However, since the SAW device they used differs in geometry and operating frequency, a COMSOL simulation will be conducted to determine what the ideal film thickness is for this device.

4.3. Determining the frequency

Making a Love-wave requires a specific frequency in order to excite the material in the correct way. A Love wave can be created if the shear wave velocity of the substrate is higher than that of the waveguide. If this is the case, the Love wave will have a shear wave speed that is between that of the substrate and waveguide $V_{sw} < V_{Love} < V_{ss}$, depending on the thickness of the waveguide [51]. Given the relationship between the waves frequency and propagation speed $f = v/\lambda$, the interval of velocities give an interval of frequencies for a fixed wavelength λ. This can be used to determine the ideal excitation frequency.

Simulations in Comsol Multiphysics 5.4 were used to find an approximation of this frequency. A video made by Greve et al. and published by Comsol [52] was used as an example. Rather than simulating the whole sensor, a block was made that functions as a unit cell of the whole sensor. This unit cell represents a block that is enclosed by the fingers of the IDT's. Therefore the dimensions of this block need to be chosen accordingly. Periodic conditions were added to the side surfaces so that the unit cell behaves like it is part of a block extending to infinity in the x and y directions.

A block of quartz was made which had the depth of λ (8 µm), a width of 20λ and thickness of 5λ. Since the Love wave that will be simulated will have a dissipating z-direction, it would make no significant difference to make it bigger. The material of the block is *Quartz RH (1978 IEEE)* rotated with Euler angles (0, 42.75, 0) to get the ST crystal orientation [53, 54]. On top of the quartz block layer of *PMMA - Poly Methyl Methacrylate*

was made with the same width and depth as the quartz. The thickness of the layer has a big effect on whether or not a Love wave can be produced, and if so on what frequency, so this was considered a variable.

Determining the frequency that is going to be used to excite the Love wave in the sensor was done in two steps:

1. Frequency domain study to determine the frequency that gives a Love wave
2. Eigenvalue study with a parametric sweep on the waveguide thickness around the approximation of the frequency

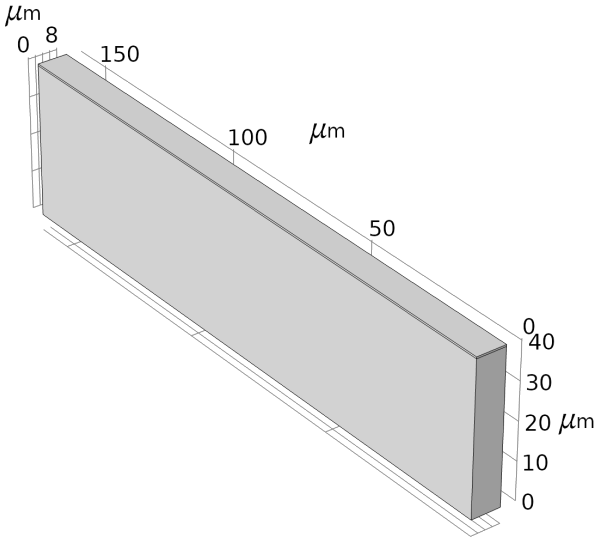

(a) Model of the unit cell representation of the SAW device

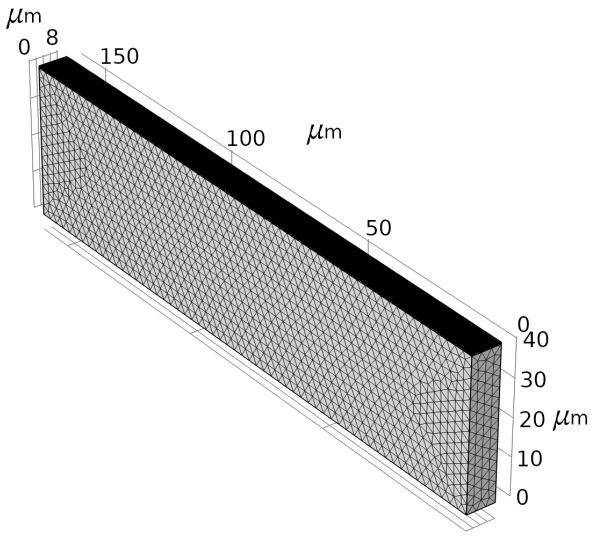

(b) A meshed version of the model

4.3.1. Frequency domain study

As explained earlier, a criterion to produce a Love wave is that the shear wave velocity of the waveguide material is lower than that of the substrate material. The produced Love wave will have a shear wave velocity that is in between this interval. Given a fixed wavelength, we can calculate the bandwidth where the Love wave certainly will be produced. A frequency-domain simulation evaluates the reaction of the material to each frequency in the interval, showing where Love waves are produced.

For the ST-cut quartz substrate, the shear wave velocity is 5050 m/s and for the PMMA waveguide it is 1100 m/s. Using:

$$f = \frac{v}{\lambda} \tag{4.1}$$

where λ is 8 µm, it can be calculated that the bandwidth where the Love wave is produced can be narrowed down to 137.5 MHz $\leq f_{Love} \leq$ 637.5 MHz. These values have been chosen as the start and stop frequencies for this study, with a step size of 5 MHz. Since only an approximation is needed, this step size will suffice.

Results of the frequency plot are shown in figure 4.3. A Love wave characterizes itself by a high lateral displacement and a low displacement into the bulk at its resonance frequency. In figure 4.3, multiple peaks show this characteristic: 380, 400, 420, 445, and 550 MHz. To validate if these really are Love-wavemodes, 3D displacement plots were evaluated. These can be viewed in figure 4.4. The characteristic displacements of Love waves can be seen at 380, 400 and 420 MHz, where there is a clear lateral wave at the surface of the PMMA while there is low displacement in the bulk of the block. Furthermore, the distance between peaks of the displacement is equal to that of the wavelength, further indicating that a Love wave is created. The highest displacement can be seen around 400MHz. At 445 MHz there is a slight displacement that looks similar to that of a Love wave, but its period is much larger than the wavelength and the lateral displacement is low. No indication of a Love wave can be seen at 550 MHz actuation. The other peaks in the frequency range are other wavemodes that cannot be used for the applications of the sensor designed here.

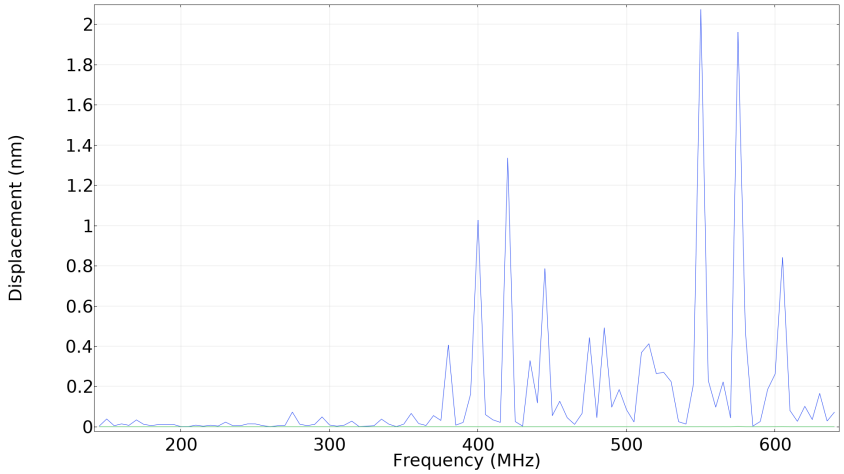

Figure 4.3: Frequency domain study of the unit cell structure. It shows the displacement in a single point on the top surface. The blue line represents the displacement in the x-direction and the green line the displacement in the z-direction

4.3.2. Eigenvalue study

Now that it is known around what frequency we need to look for Love waves, a parametric sweep combined with an eigenvalue study can show what waveguide thickness and exact frequency gives the largest surface displacement and therefore the best performance. An eigenvalue study looks for different eigenfrequencies of a model around a given frequency. By evaluating the results it can be determined which frequency will create a Love wave at its surface and how big the surface displacement will be. This is repeated for different waveguide thicknesses by using a parametric sweep to determine the optimal surface displacement. The settings for the eigenvalue study where:

- Search for eigenfrequencies around: 400 MHz
- Desired number of frequencies: 20
- Eigen frequency search method around shift: Closest in absolute value
- Use real symmetric eigenvalue solver: Automatic

The displacement plot for each waveguide thickness' corresponding Love wave frequency can be shown in figure 4.5. These figures show that Love waves are created for a waveguide with a thickness between 400 nm and 560 nm. Substrates with a thicker waveguide do not show any frequency that creates a Love wave. Evaluation for the max. displacement is shown in table 4.3. For the evaluation, the x/y displacement is compared to the z displacement. From the three waveguide thicknesses that show a Love wave, the 560nm design performs the best with the largest lateral displacement while maintaining a low z displacement. Therefore, based on these simulations, the thickness of the waveguide of the SAW sensor will be 560 nm.

Table 4.3: Evaluation of the different waveguide thicknesses at the frequency that creates a Love wave or, if there is one, resembles the closest to a Love wave.

Relative thickness (Th/lambda)	**res. freq. (MHz)**	**Max. xy-displacement [nm]**	**z-displacement [nm]**
0.05 (400 nm)	400.09	2.1	<0.001
0.06 (480 nm)	404.26	5.3	<0.04
0.07 (560 nm)	398.86	12	0.1
0.08 (640 nm)	400.83	3	0.1
0.09 (720 nm)	399.12	3	0.1
0.1 (800 nm)	400.77	3	0.1

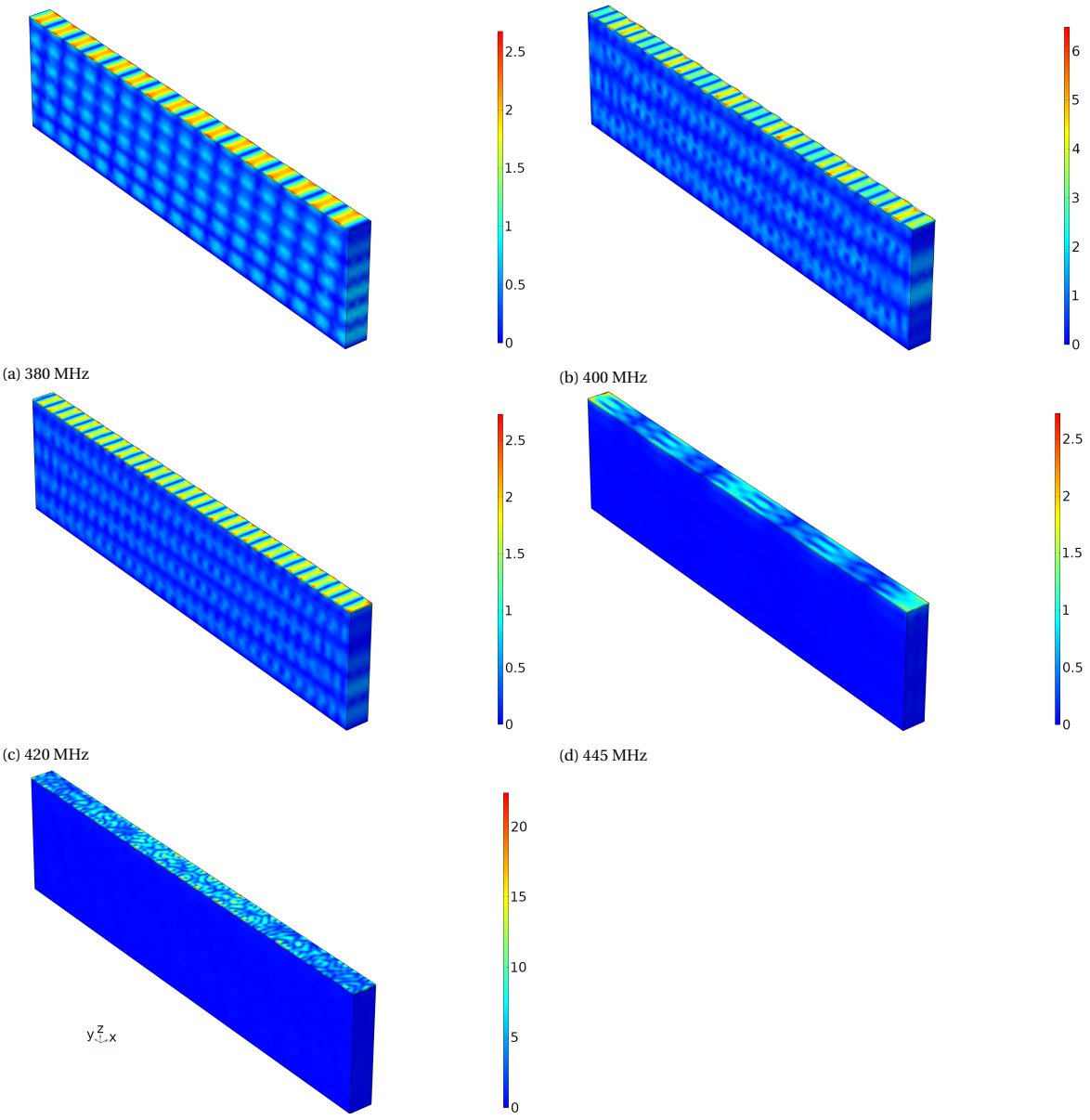

(a) 380 MHz

(b) 400 MHz

(c) 420 MHz

(d) 445 MHz

(e) 550 MHz

Figure 4.4: 3D total displacement plots of the single wavelength structure eigenvalue study results.

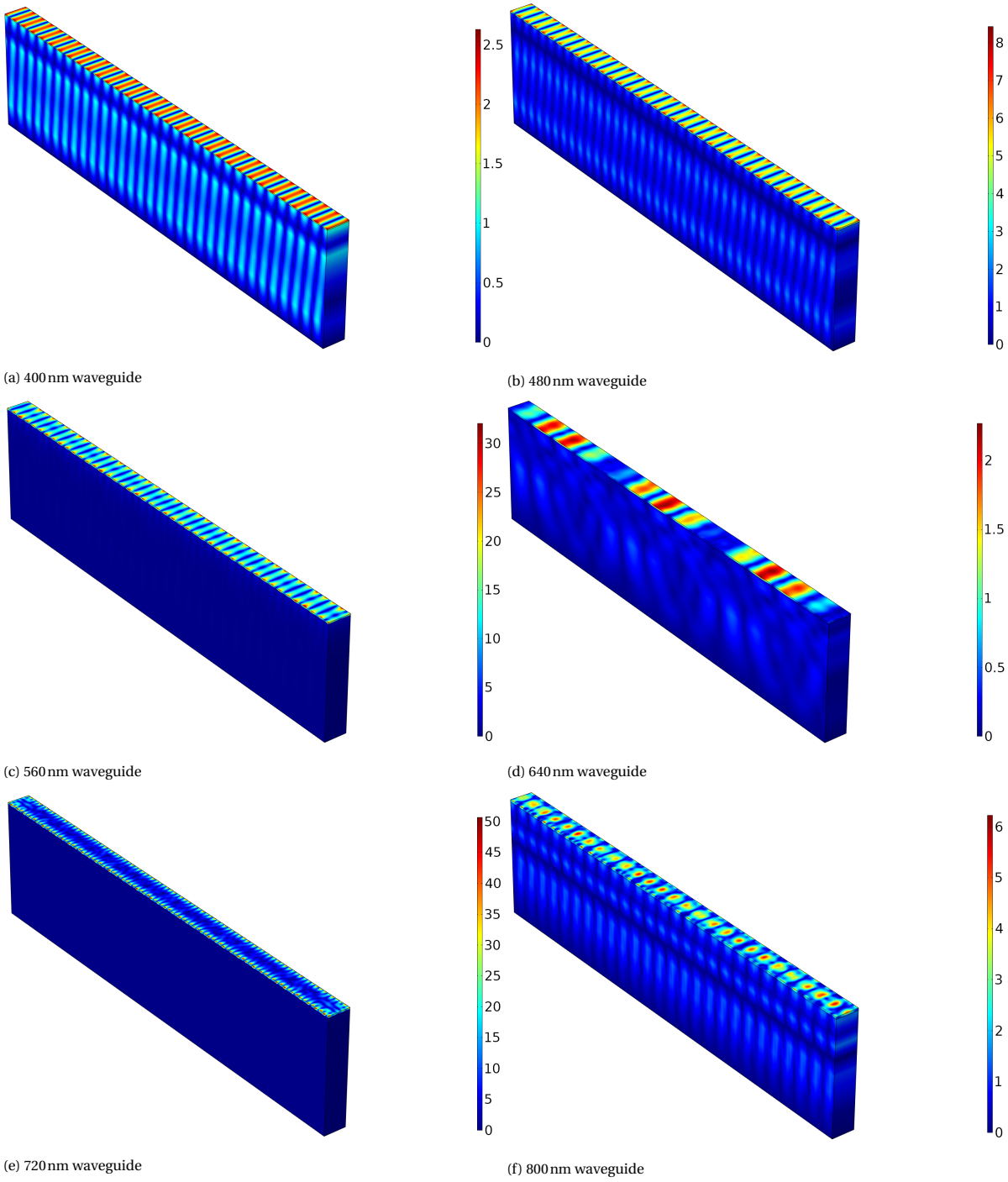

(a) 400 nm waveguide

(b) 480 nm waveguide

(c) 560 nm waveguide

(d) 640 nm waveguide

(e) 720 nm waveguide

(f) 800 nm waveguide

Figure 4.5: 3D displacement plot for every waveguide thickness and their optimal frequency

4.3.3. Final design

Now that the full device is designed, a complete description can be given. The surface acoustic wave sensor will create a Love wave by using a ST-cut quartz substrate, aluminium IDTs and a 560 nm thick PMMA waveguide. The IDT finger width is 2 µm, resulting in a 8 µm wavelength and a 400 MHz resonance frequency. The aperture of the IDTs is 50 times the wavelength or 400 µm. Several designs for the IDTs are made, with different number of finger pairs (25, 50 and 75) and different delay line lengths (500, 1000 and 5000 µm). A representation of the SAW device is shown in figure 4.6.

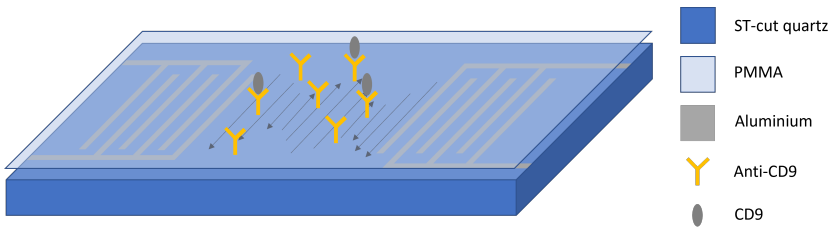

Figure 4.6: Representation of the full SAW sensor (not in scale)

4.4. Impedance matching circuit

When attaching the sensor to a network analyzer, where a 400 MHz signal will be given as an input, we need to take into account that the sensor has both resistive and reactive components. For efficient power transfer, creating an impedance matching circuit between the network analyzer probe and the sensor input is essential. The impedance matching network will be created on a PCB to where the sensor chip is attached to. This section will calculate the impedance of the sensor, and calculate the appropriate impedance matching circuit. The resulting circuit will be simulated in LT-spice for validation.

4.4.1. Sensor device Impedance

Resistance The resistive component of the sensor device is fully determined by the IDT material (aluminum) and geometry. For each design, the resistance is estimated by lumping different sections of the IDT and calculating the resistance for each respective component. Each IDT is divided into a contact pad, contact line, finger connector in series and individual fingers in parallel (figure 4.7). This setup ignores the resistance of the wire bonding is considered to be negligible compared to that of the IDTs and is not taken into account. It should be noted that the width of the contact line varies between each design to let the total input resistance approach 50 Ω to allow for easier impedance matching.

The resistance of the IDT structure is calculated by:

$$R_{tot} = R_{\mathrm{A}} + R_{\mathrm{B}} + R_{\mathrm{C}} + R_{\mathrm{D}} \tag{4.2}$$

$$R_i = \frac{\rho * L_{\mathrm{i}}}{A_{\mathrm{i}}} \tag{4.3}$$

Where $i = (A, B, C, D)$, ρ the resistivity of aluminium, L the length of the structure and A the surface area of the structure where the current flows through

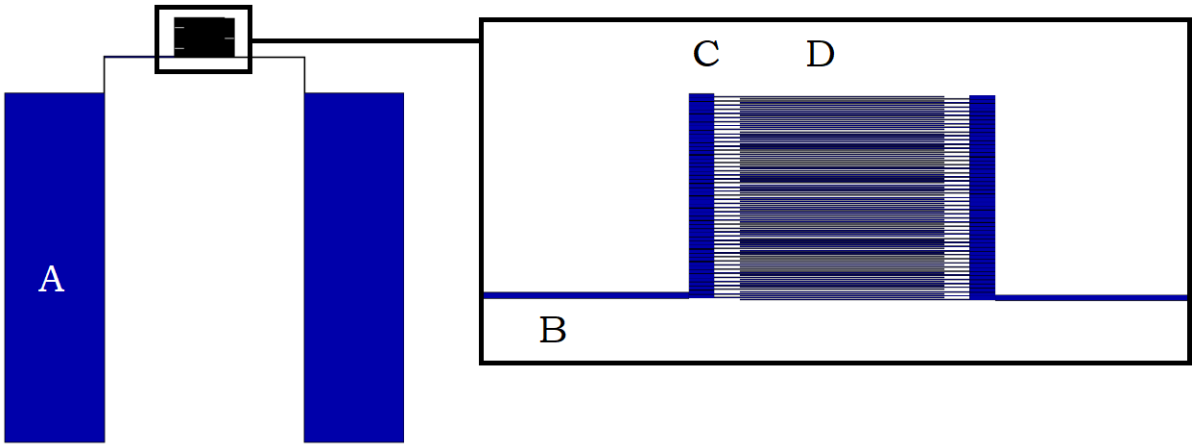

Figure 4.7: Division of sections for resistance calculation: contact pad (A), contact line (B), finger connector(C), fingers (D)

Capacitance The largest capacitance of the IDTs is in between its fingers. To calculate the capacitance of the total IDT structures, each finger's capacitance is separated into a top and bottom part. The top part has PMMA as dielectric, whereas the bottom part has quartz (figure 4.8). The sides of the fingers are orders of magnitude smaller in surface area than the top and bottom, so these are neglected.

The capacitance of an IDT structure is calculated by:

$$C_{\text{IDT}} = C_{\text{PMMA}} + C_{\text{Quartz}} \tag{4.4}$$

$$C_{\text{PMMA}} = \frac{\epsilon_{\text{PMMA}} * A}{d} * N_{\text{f}} \tag{4.5}$$

$$C_{\text{Quartz}} = \frac{\epsilon_{\text{Quartz}} * A}{d} * N_{\text{f}} \tag{4.6}$$

Where ϵ_{PMMA} and ϵ_{Quartz} is the dielectric constant of PMMA and quartz respectively, A the surface area of a finger, d the distance between fingers and N_{f} the number of fingerpairs

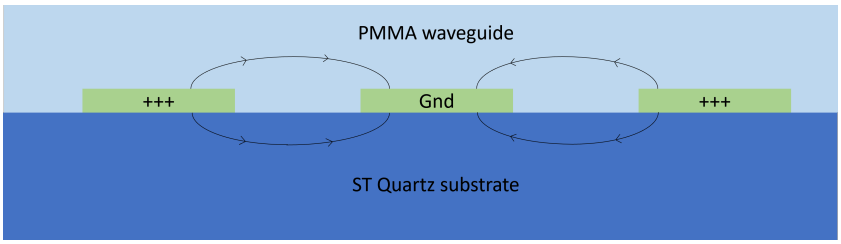

Figure 4.8: Visualization of the capacitance between the fingers

Acoustic vibration electrical equivalent In order to accurately characterize the IDT structures, the losses due to acoustic resonation. This can be done by calculating modeling it as an electric circuit. The Butterworth - van Dyke (BVD) model is an example of how this can be done assuming the acoustic frequency is close to resonance and will be used here [55].

Figure 4.9 shows the equivalent circuit of the IDT structure at resonance according to the BVD model. It consists of two arms. The bottom arm is the electrical arm and represents the electrical behavior of the IDT as a capacitance C_0, which is calculated earlier. The mechanical arm represents the piezoelectric vibration and is modeled by a capacitor C_m, inductor L_m and a resistance R_{m}. C_{m} for the first harmonic of resonance is calculated by [56]:

$$C_{\text{m}} = C_{\text{IDT}} \frac{8k^2}{\pi^2} \tag{4.7}$$

where $k^2 = 0.0012$ is the electromechanical coupling coefficient of quartz. The inductance is calculated by [55]:

$$L_m = \frac{1}{\omega_{\text{res}} C_{\text{m}}} \tag{4.8}$$

Where w_s^2 is the resonance angular frequency. Finally, R_m is calculated by[55]:

$$R_m = \frac{p i^2 \eta}{8k^2 \rho * v^2 C_{\text{IDT}}} \tag{4.9}$$

where v is the wave velocity, ρ is the density of quartz and η is the acoustic viscosity.

IDT impedance Now that an electrical equivalent representation of the complete IDT structure is known, the impedance of the IDT can be calculated as well. The impedance of the motional arm is [55]:

$$Z_m = j(\omega L_{\text{m}} - \frac{1}{\omega C_{\text{m}}}) + R_{\text{m}} \tag{4.10}$$

At resonance, L_m can be expressed as a function of C_m by equation 4.8. Replacing L_m in equation 4.10, cancels out the imaginary part which means that the impedance of the motional arm is purely real at resonance. From this, it follows that the impedance of the complete IDT structure is equal to:

$$Z_{IDT} = j\omega C_{IDT} + \frac{1}{R_m} + R_{Al} \tag{4.11}$$

where C_{IDT} is the capacitance of the IDT structure, R_m the motional resistance of the acoustic wave and R_{Al} the resistance introduced by the aluminium material of the IDT structure. However, since C_{IDT} is very small, it follows from equation 4.9that R_m be very large. Compared to R_{Al}, $\frac{1}{R_m}$ will therefore be negligible and equation 4.11 can be simplified to:

$$Z_{IDT} = j\omega C_{IDT} + R_{Al} \tag{4.12}$$

of which the values for each design can be viewed at table 4.4.

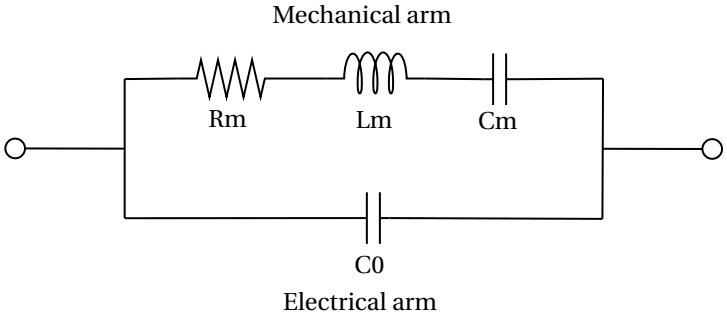

Figure 4.9: Butterworth - van Dyke model representing an IDT structure

Table 4.4: Resistance and capacitance of a single IDT structure for each IDT design

Sensor Design	Resistance (Ohm)	Capacitance (pF)
1-1	49.94	0.301
1-2	53.08	0.602
1-3	52.26	0.903
2-1	52.38	0.301
2-2	49.34	0.602
2-3	52.95	0.903
3-1	53.17	0.301
3-2	51.84	0.602
3-3	52.00	0.903
FIDT	54.03	0.392

4.5. Impedance matching and PCB design

Based on the impedances of the IDTs, a Pi-matching network is created to increase the efficiency of the power transfer from the source to the sensor. The total circuit for each IDT design is simulated in LTSpice for validation, which can be seen in figure 4.13.

The value of the components in the matching network was calculated following a document published by SiliconLabs [57]. The quality factor chosen in these calculations is ideally high such that there is a clear signal around the resonance frequency, but not too high that a frequency shift as a result of gravimetric sensing will be attenuated too much. It also needs to be taken into account that the calculated impedance matching network would show the ideal circuit. When ordering the components, these exact values will most likely not be available and an approximation must be made. This will increase bandwidth. Therefore a circuit will be designed with a higher quality factor than needed, to compensate for the bandwidth increase. A Q-factor of 500 will leave an 800 kHz bandwidth at 400 MHz in the ideal situation, but using real components this will turn out to be bigger.

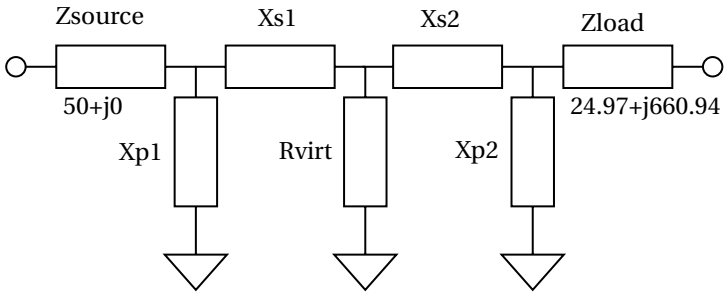

Figure 4.10: Schematic view of the 2 L-matching section as an intermediate step for calculating the pi-matching network values

For all devices, the input and output impedances will be 50 Ω, given by the signal generator and the spectrum analyzer. However, the impedance of the devices themselves is different for every design. A different impedance matching network is therefore necessary for each design. A numerical example of the calculations will be done here for the input of design 1-1. The impedance matching networks will be calculated in a similar way, but with different values for the load.

Table 4.5: Starting parameters for the calculation of the impedance matching circuit

Parameter	**Value**	**Unit**
Z_{source}	50+j0	Ω
Z_{load}	24.97 + 660.94	Ω
f_{res}	400	MHz
Q	500	

Calculation The starting parameters are shown in table 4.5. The calculation strategy starts with considering the pi-structure as two L-matching sections, with a virtual resistance in between them (figure 4.10). From this, it will then be easy to convert this to a pi-matching circuit. The value of the virtual resistance can be calculated using the following formula:

$$R_{\text{virt}} = \frac{R_{\text{H}}}{Q^2 + 1} \tag{4.13}$$

Here, R_H is the highest real impedance value between the source and load which is in this case 50 Ω. Putting in the Q value from table 4.5, we can calculate a virtual resistance:

$$R_{\text{virt}} = \frac{50}{500^2 + 1} = 0.2\,\text{m}\Omega \tag{4.14}$$

Now, we can calculate the first L-network: Xs1 and Xp1. This can be done by using:

$$X_{\text{p1}} = \frac{R_{\text{source}}}{Q} \tag{4.15}$$

$$X_{\text{p1}} = \frac{50}{500} = 0.1\,\Omega \tag{4.16}$$

$$X_{\text{s1}} = R_{\text{virt}} Q \tag{4.17}$$

$$X_{\text{s1}} = 2.0 \times 10^{-4} * 500 = 0.1\,\Omega \tag{4.18}$$

For the second L-network, we have a complex load. To effectively absorb the reactive load, we convert the series load resistance and reactance to its parallel equivalent. The value of X_{p1} can then be chosen to absorb the loads' parallel equivalent reactance. We first need to calculate the quality factor of the load Q_{load}. From this, we can calculate the equivalent parallel circuit components of the load $R_{\text{P}_{\text{Load}}}$ and $X_{\text{P}_{\text{load}}}$:

$$Q_{\text{load}} = \frac{X_{\text{load}}}{R_{\text{load}}} \tag{4.19}$$

$$Q_{\text{load}} = \frac{660.94}{24.97} = 26.47 \tag{4.20}$$

From this, we can convert the series load and reactance to their parallel equivalents:

$$R_{\text{P}_{\text{Load}}} = R_{\text{load}}((Q_{\text{load}})^2 + 1) \tag{4.21}$$

$$R_{\text{P}_{\text{Load}}} = 24.97 * (26.47)^2 + 1) = 17.52\,\text{k}\Omega \tag{4.22}$$

$$X_{\text{P}_{\text{load}}} = \frac{R_{\text{P}_{\text{Load}}}}{Q_{\text{load}}} \tag{4.23}$$

$$X_{\text{P}_{\text{load}}} = \frac{17520}{26.47} = 661.88\,\Omega \tag{4.24}$$

Now we have determined that the loads parallel equivalent reactance is 661.88 Ω, we can calculate its equivalent capacitive value using equation 4.24 and table 4.5:

$$C_{load} = \frac{1}{2\pi f_{res} X_{P_{load}}} \tag{4.25}$$

$$C_{load} = \frac{1}{2\pi * 400 \times 10^6 * 661.88} = 0.6\,\text{pF} \tag{4.26}$$

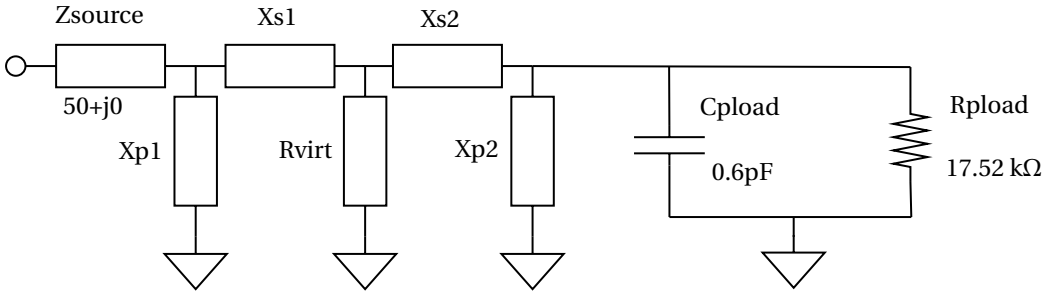

Figure 4.11: Schematic view of the 2 L-matching sections with the load transformed to its parallel equivalent

With the parallel equivalent load (4.11), we can now calculate the Q factor for the second L network:

$$Q_2 = \sqrt{\frac{R_{\text{P}_{\text{Load}}}}{R_{\text{virt}}} - 1} \tag{4.27}$$

$$Q_2 = \sqrt{\frac{17.52 \times 10^3}{0.2 \times 10^{-}3} - 1} = 9359.4 \tag{4.28}$$

This can than be used to calculate the components of the second L-network:

$$X_{\text{p2}} = \frac{R_{\text{P}_{\text{Load}}}}{Q_2} \tag{4.29}$$

$$X_{\text{p2}} = \frac{17.52 \times 10^3}{9359.4} = 1.87 \tag{4.30}$$

$$X_{\text{s2}} = R_{\text{virt}} Q_2 \tag{4.31}$$

$$X_{\text{s2}} = 0.2 \times 10^{-2} * 9359.4 = 1.87 \tag{4.32}$$

Equations 4.16, 4.18, 4.30 and 4.32 give us the values we need to complete the two L-matching networks (figure 4.12). Now we can calculate the component values for the pi-matching network:

$$C_1 = \frac{1}{2\pi f_{res} X_{\text{p1}}} \tag{4.33}$$

$$C_1 = \frac{1}{2\pi * 400 \times 10^6 * 0.1} = 3978.87\,\text{pF} \tag{4.34}$$

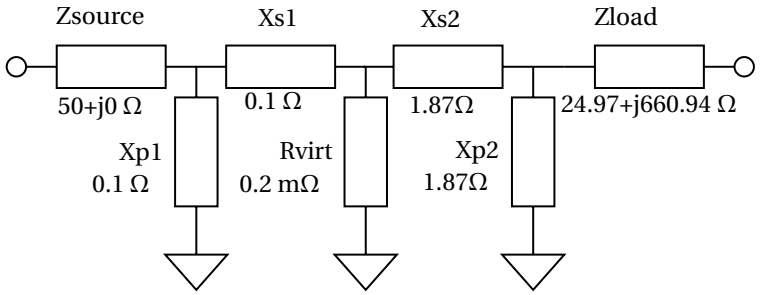

Figure 4.12: Schematic view of the 2 L-matching sections with their calculated values for the 1-1 input design

$$C_2 = \frac{1}{2\pi f_{\text{res}} X_{\text{p2}}} \tag{4.35}$$

$$C_2 = \frac{1}{2\pi * 400 \times 10^6 * 1.87} = 213.16\,\text{pF} \tag{4.36}$$

$$L = \frac{X_{\text{s1}} + X_{\text{s2}}}{2\pi f_{\text{res}}} \tag{4.37}$$

$$L = \frac{0.1 + 1.87}{2\pi * 400 \times 10^6} = 0.78\,\text{nH} \tag{4.38}$$

The same calculations are done for the output of the sensor, where the output is considered the source impedance and the spectrum analyzer is the 50+j0 Ω load impedance. All the resulting values are listed in table 4.6. However, the components that could be bought do not have these exact values and approximations needed to be made.

Table 4.6: Values of the pi-matching network components for each design

Matching circuit	**C_1 (pF)**	**L (nH)**	**C_2 (pF)**
1-1 input	3978.87	0.78	213.16
1-1 output	150.70	1.09	3978.87
1-2 input	3978.87	0.40	438.40
1-2 output	300.63	0.57	3862.00
1-3 input	3978.87	0.28	650.00
1-3 output	449.25	0.39	3892.00
2-1 input	3978.87	0.77	218.28
2-1 output	150.68	1.09	3887.40
2-2 input	3978.87	0.42	422.90
2-2 output	298.80	0.57	3978.87
2-3 input	3978.87	0.28	654.20
2-3 output	449.20	0.39	3866.40
3-1 input	3978.87	0.76	219.90
3-1 output	150.68	1.09	3858.40
3-2 input	3978.87	0.41	433.30
3-2 output	300.70	0.57	3908.00
3-3 input	3978.87	0.28	648.50
3-3 output	449.30	0.39	3901.60
FIDT input	3978.87	0.59	288.50
FIDT output	196.10	0.85	3827.60

4.5.1. LT-spice Simulation

Now that the complete electrical representation of the SAW device and its impedance matching components are known, simulations can validate the calculations. Simulations are performed in LTspice XVII. A drawing of the circuit is shown in figure 4.13. V_1 and Z_{source} represent the signal generated at the input and the lead

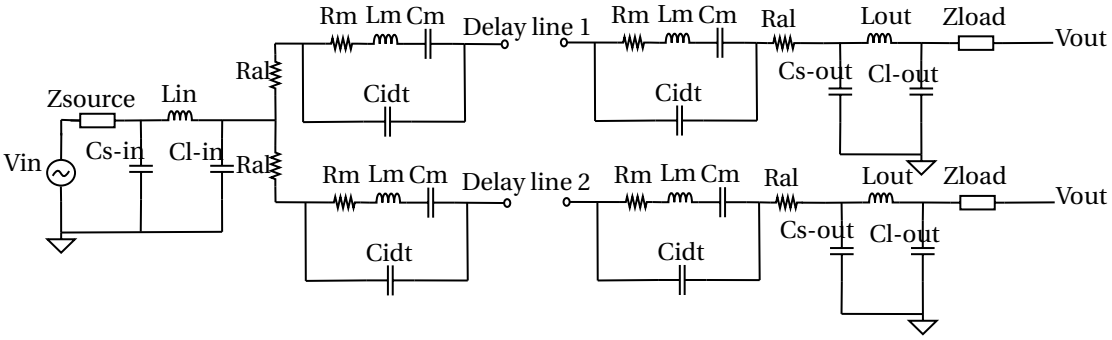

Figure 4.13: Circuit representation of the sensor and its impedance network

source impedance (50 Ω). L_{in}, $C_{\text{s-in}}$ and $C_{\text{l-in}}$ represent the input impedance matching circuit for both input IDT structures. These are both equivalent to eachother and are R_{m1}, L_{m}, C_{m} and C_{IDT}. In reality, the signal will now travel through the delay line as an acoustic wave which is represented by *trans*. Attenuation in the delay line is ignored for this simulation.

At the output, the IDT's are electrically identical to the input IDT's and are therefore represented by the same components. The impedance matching circuit for the output IDT's are identical to each other and are represented by $C_{\text{s-out}}$, l_{out} and $C_{\text{l-out}}$. The signal that can be read at the outputs is marked by V_{out} and V_{ref} and the impedance of the lead is represented by Z_{load}.

Figure 4.14 and 4.15 show the AC analysis of the electrical equivalent model of the 25-500 design simulation. At the output, the signal is attenuated with 18.2 dB and has a bandwidth of 762kHz. Figure 4.15 also shows that there are two resonance peaks indicating that there is a slight mismatch between the input and output impedance matching circuit.

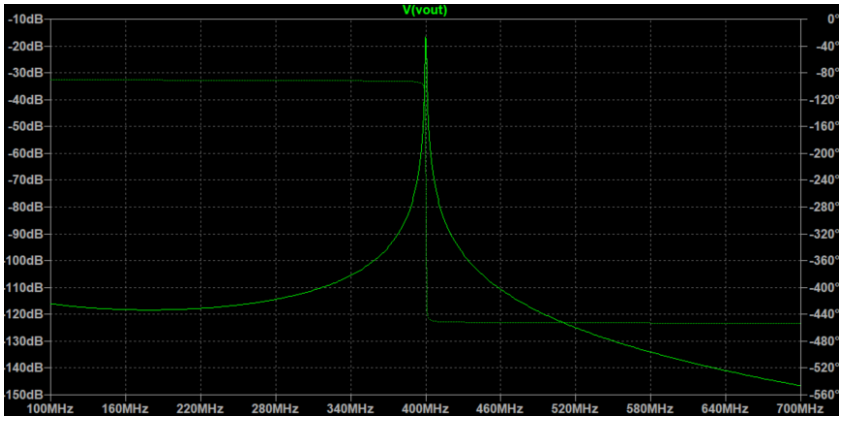

Figure 4.14: AC analysis of the electrical equivalent model of the 25-500 design

Recall that a quality factor of 500 was chosen to compensate for the increase in bandwidth when buying components which will only approximate the calculated values. When replacing the impedance matching circuit with the ordered components, the bandwidth has indeed increased to 13.4 MHz as can be seen in figure 8.3. Furthermore, the mismatching of the ordered components has pulled the two resonance frequencies further apart and has increased the attenuation of the signal to -53.72 dB.

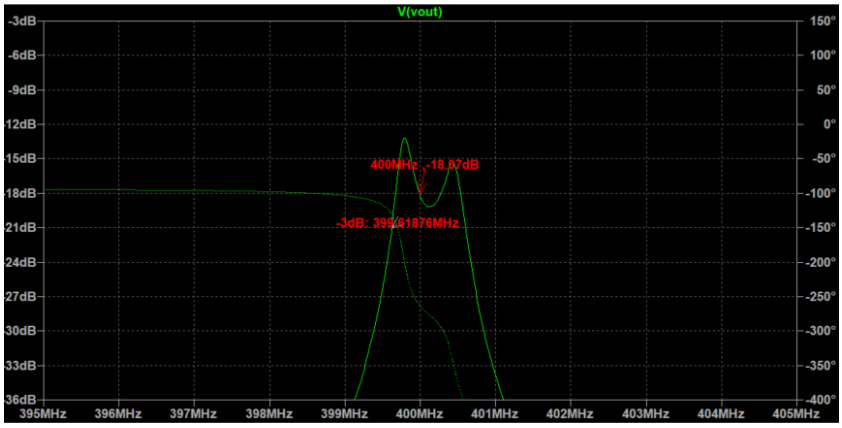

Figure 4.15: Bandwidth extraction on the AC analysis

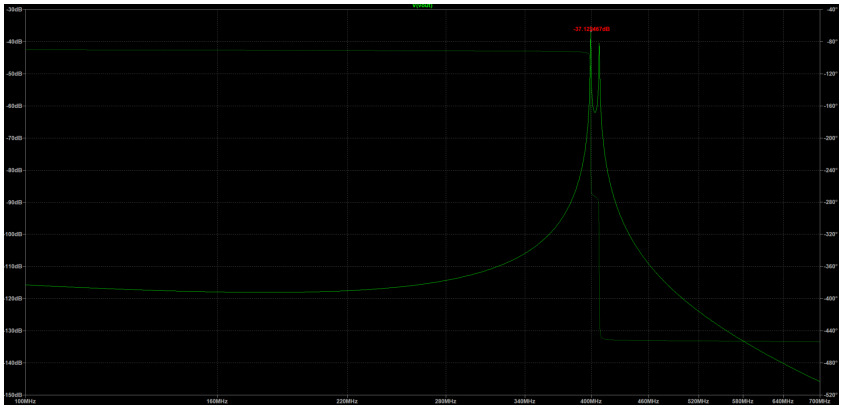

Figure 4.16: AC analysis of the electrical equivalent model of the 25-500 design with the ordered impedance matching components

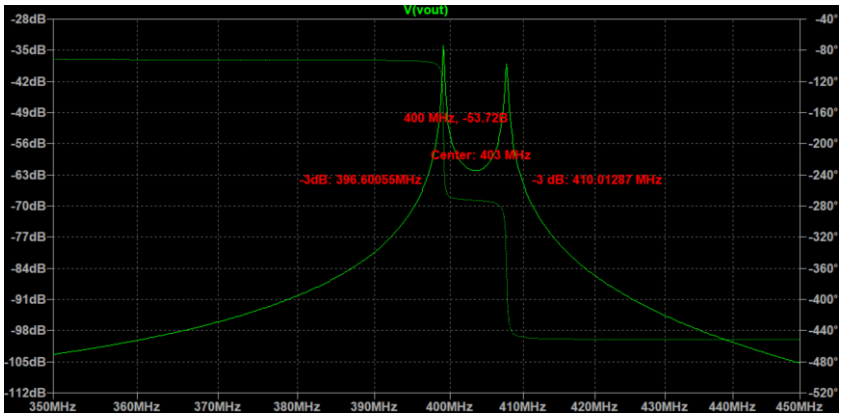

Figure 4.17: Bandwidth extraction on the AC analysis on the 25-500 design with ordered components

5

Device Fabrication

This chapter summarizes the steps taken to produce the SAW device by microfabrication. A more detailed, step-by-step description can be viewed in appendix B

5.1. Sensor production

Fabrication of the SAW biosensors began with a 4 inch diameter, 500 ± 25 µm thick, double polished ST-cut quartz wafer from MicroChemicals (figure 5.1a). The wafers were first cleaned in a HNO_3 bath for ten minutes to get rid of small particles and impurities. The pure aluminium was sputtered on the top side of the wafers in a Trikon Sigma Dealer at 350 °C to create a layer of 50 nm thickness (figure 5.1b).

The IDT and contact pads structures were patterned by a single-mask lithography process. 2.3 µm of AZ ECI 3027 positive photoresist from MicroChemicals was spin coated on top of the aluminium (figure 5.1c). After UV-light exposure under the mask (Compugraphics), development was done by first having a post-exposure bake at 115 °C for 90 seconds, using Shipley MF322 as a developer and a hard bake at 100 °C for 90 seconds (figure 5.1d).

Aluminium was patterned using wet-etching processes. The wafers were dipped in a Triton X-100 solution for 20 seconds to remove 50 nm of aluminium (figure 5.1e). Afterwards the wafers were immediately flushed with dionized water to stop the etching. Residual photoresist was then removed in a bath of acetone at 40 °C for at least 1 minute (figure 5.1f).

Next, the wafers were coated with 495k molecular weight PMMA in 6% anisole solution. It was spin coated onto the wafer at 1500 rpm for 30 seconds with a 500 rpm/s ramp. The PMMA was cured by baking it at 180 °C for one minute (figure 5.1g). To allow for an electrical connection between the aluminium contact pads and measurement equipment, the PMMA that is laying on top of the contact pads will be removed. This is done with acetone and a swab, while making sure the IDT's and delay lines are fully covered with PMMA.

At this point, the devices are functional and the wafer is diced into 10x10 mm chips to separate the individual devices from each other. The diced devices are then surface activated by putting them in plasma etcher for 10 seconds in a 75 Pa chamber with an operating frequency of 27.12 MHz with a power of 200 W. From this point onwards, the next steps need to be done within 24 hours to ensure that the surface remains sufficiently activated. Once this is done, the chips will be fixed to the PCB's and connected using wire bonding.

Now, the sensor is ready for use. If you put a 400 MHz signal at the input a Love wave will propagate through the delay line and can be measured at the output. However, nothing can be measured yet since the surface is not able to capture anything which will increase the surface mass density. This will done by activating the surface and making it sensitive for CD-9.

First, the devices are exposed to a 40 kHz, 200 W plasma in a 75 Pa chamber for ten seconds . This activates the surface and make adhesion in the following steps more efficient [58]. This is followed by dripping

a solution of 73 mg EDC (ThermoFischer Scientific) and 8.9 mg NHS (ThermoFischer Scientific) in 5 mL milli-Q water onto the surface until the delay line is fully covered 5.1h. After one hour of incubation at room temperature, the solution is washed away using phosphate buffered saline (PBS). Next a protein streptavidin (Merck-Millipore) and milli-q water solution (0.1 mg/mL) is deposited on the surface and incubated at room temperature for one hour. Again, the solution is washed away using PBS. As a final step, the surface is exposed to anti CD-9 (eBioscience) in a 1 ug/ml concentration which is incubated for 2 hours. At this point, the sensor surface is activated and ready to attach CD-9. The urine samples are taken out to reach room temperature and droplets are deposited on the device surfaces 5.1j.

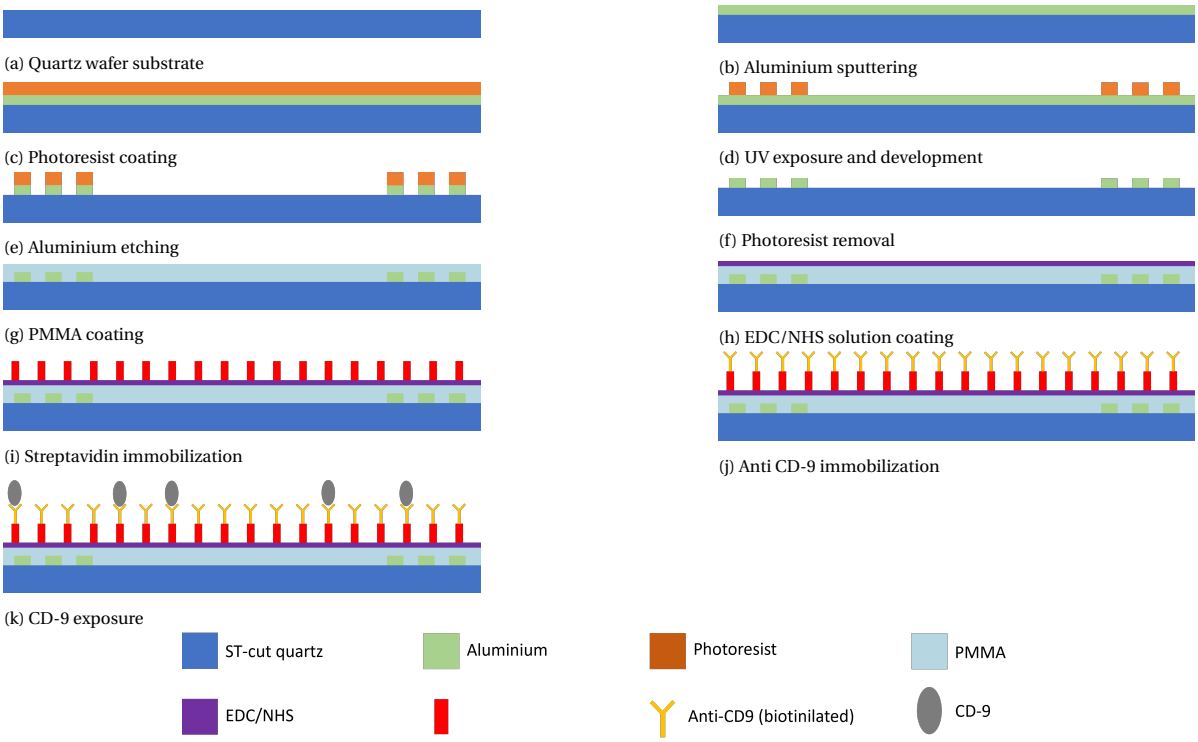

Figure 5.1: Production steps describing the process of creating the Surface Acoustic wave sensor by microprocessing.

6

Test Setup

6.1. Urine sample collection

The collection of the urine samples has been done by urologists of the Erasmus Medical Centre for other scientific purposes, but we were allowed to use some monsters as well. The collection process is done according to the European Association of Urologists (EAU) Standard Operating Procedure [59].

Urine samples were taken from 10 PCa positive and 10 PCa negative patients (see table 6.1) in 2013 and 2014. The first 50 mL of urine after a DRE is collected in a specimen cup and stored in a 2-8° fridge or cool box. Within 4 hours after collection, the samples are centrifuged at 4° for 20 minutes at 500 G, with the brakes of the centrifuged turned off. The resulting urinary supernatant is separated from the urinary sediment and stored in vials in −80° freezers.

From the urinary supernatant, small monsters of 1 mL are taken from each specimen. Next to that, two pools were made where 0.2 µL of all the PCa positive are pooled together. The same has been done with all the PCa negative specimens. The monsters were then stored at −20° until they were needed for testing.

Table 6.1: Characterization of the urine specimens

Patient no.	Prostate cancer	Gleason score	PSA
1	Positive	6	5.6
2	Positive	6	1.8
3	Positive	6	7.0
4	Positive	6	10.4
5	Positive	6	6.7
6	Positive	6	5.9
7	Positive	6	4.5
8	Positive	3+3	9.4
9	Positive	6	15.0
10	Positive	3+3	-
11	Negative	-	5.3
12	Negative	-	0.9
13	Negative	-	0.6
14	Negative	-	2.1
15	Negative	-	1.6
16	Negative	-	8.6
17	Negative	-	3.9
18	Negative	-	3.5
19	Negative	-	1.2
20	Negative	-	12.0

6.2. Test setup

The performance of the devices is measured using a network analyzer (Rhode & Schwartz ZND) and a spectrum analyzer (Rhode & Schwartz FPL 1007). The PCB's outputs are SMA connectors which will be connected to the analyzers using 50 Ω leads. For the network analyzer, the main interest is signal attenuation and distinguishable resonance frequencies. For the spectrum analyzer, it is the frequency shift and signal bandwidth.

Measurements start by conducting a S_{21} measurement on the network analyzer of a PCB without a SAW device to characterize its open circuit response. A 0 dBm signal will be given at the input while the output is connected back to the network analyzer to determine its response. Next, each PCB will be prepared with two SAW device chips to be connected to the network analyzer and the spectrum analyzer. After conducting the same S_{21} measurements as with the PCB without the SAW device, a comparison is made to determine the SAW device its response.

Next, the PCBs will be connected to the spectrum analyzer and signal generator with an input signal of 0 dBm. This is to determine the frequency shift caused by the mass of the PMMA layer and IDT structure. Since the mass of PMMA and IDT on the surface is known, this allows for the determination of the sensitivity of the sensor. Afterward, the devices are taken to the lab to perform the biochemical steps to immobilize anti-CD9 at the PMMA surface. Each device consists of two SAW structures. One of them will be exposed to the urine samples (connected to the output port of the PCB), while the other remains with only the anti-CD9 (connected to the reference port). Once the urine exposure is completed, the PCBs are taken back to the measurements setup to perform measurements with the spectrum analyzer. The difference in frequency between the input and the output port will indicate the frequency shift caused by the captured CD9.

7

Results

7.1. production

7.1.1. Etching

After etching, the wafers were inspected on their patterns using a microscope. Figure 7.1 shows an example of the 50-500 IDT pattern.

Although most of the patterning went well, roughly a quarter of both wafers turned out to be over etched. Examples are given in figure 7.2. This significantly reduced the yield of the devices and resulted in all of the FIDT devices being unusable for testing.

First it was checked if this could be caused by the etching process. Since wet-etching is used, it is possible that part of the etchant remained on the wafers which over-etched the pattern. However, both wafers were over-etched on the same location and in the same way. As this would mean that the wafers must have had residual etchant on the same location, this explanation seems unlikely. On top of that, the wafers were dumped in a water rinser within roughly 2 seconds after the 20 second etching period. Since it takes around 20 seconds to etch away 50 nm of aluminium, this extra time would result in an additional 5 nm in the worst case. Since the width of a single finger is 2 µm, the amount of over-etching would be negligible.

The overetching could also be caused by a faulty lithography mask. However, putting the mask under the microscope showed no defects or thinner lines.

The most likely explanation of the overetching is that it is caused by the contact aligner. The contact aligner was used with the assistance of experienced technicians in the cleanroom, but some small defects in the lens could cause the UV light to not be focused properly. It will then expose regions that are underneath the masked that should not be exposed.

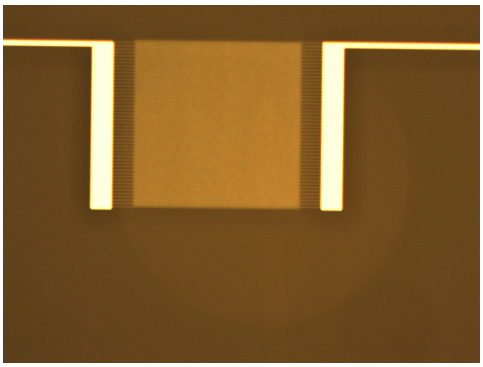

(a) IDT pattern for the 50-500 design (magnified with factor 5)

(b) IDT pattern for the 50-500 design (magnified with factor 20

Figure 7.1: Microscope pictures of the IDT patterns after etching (before PMMA deposition)

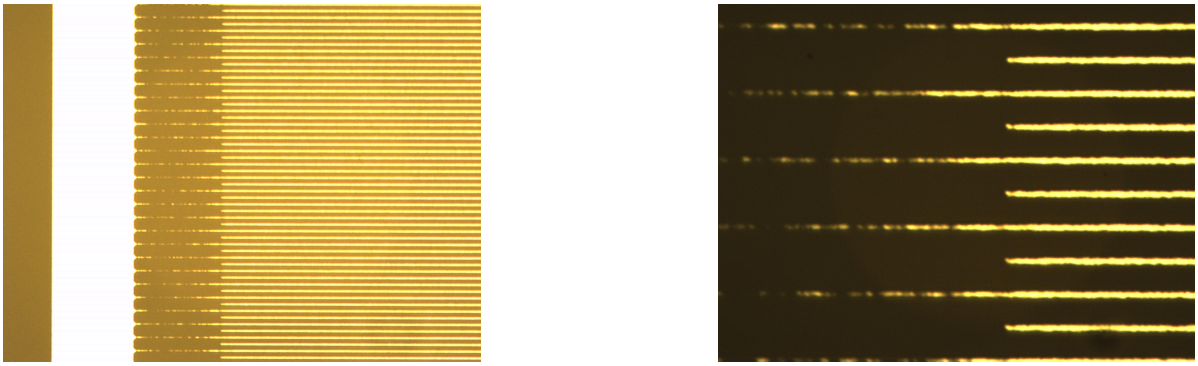

(a) IDT pattern of a 75-1000 design (magnified with factor 20)

(b) IDT pattern of a 75-1000 design (magnified with factor 100

Figure 7.2: Microscope pictures of overetched IDT patterns after etching (before PMMA deposition)

7.1.2. Dicing

As described earlier, multiple sensors were produced on a single wafer. The idea is then to cut them up into individual chips which then can be connected to the PCB and tested. Usually, the dicing of wafers is an easy process. However, our wafers unexpectedly proved to be much harder to cut than usually is the case.

Dicing of the wafers was done by the Disco DAD321 carrying a diamond glass saw with a feeding speed of 5 mm/s. The wafers were placed in the Disco as per the instructions with the assistance of a lab technician. Once the machine was done and upon inspection of the dice, the PMMA had come off the wafers and was spread out over the adhesive foil caused by the cooling system of the saw. To prevent the saw from overheating and being damaged during the dicing of the wafer, a water jet is sprayed on the top surface which blew off the PMMA layer.

Therefore, before going any further in the process, this needed to be overcome. The first option was to look for a laser dicer. This is a dry process that does not require any liquid cooling. However, there is no laser dicer that could be used within TU Delft and using one of an external company would consume too much time.

The possibility of protecting the PMMA surface was investigated as well. Another layer of foil could be placed on top but this would also adhere to the PMMA itself, potentially ripping it off when removing the foil. To prevent this, a custom processing method was created. Instead of cutting the wafer with the front side up, the wafer was flipped so that the PMMA side was facing away from the saw and its cooling jet. To prevent the PMMA from sticking on the adhesive foil that keeps the wafer in its place during dicing, something was placed in between the two layers at the functional area of the wafer. Filtration paper worked very well as a non-stick layer and a square was cut that covers the area of the wafers where the devices are. To make sure the PMMA is protected from the cooling water during sawing as well, the saw height was increased such that it would cut only 70% into the wafer. After the dicing is completed the chips could then be separated by breaking along the lines by hand

To test this process, three silicon dummy wafers were covered with PMMA. There were no spare quartz wafers available so these could not be used as dummies. The second dummy wafer was cut correctly, but when the vacuum that keeps the wafer in place was removed, the wafer already broke along its cutting lines, causing water that was laying on top of the wafer to seep through and wet the filtration paper. This caused the filtration paper to stick on the PMMA and peel it off once removed.

To prevent this, the saw height was increased so that it would cut 50% into the wafer. On top of that, the water was first removed with a nitrogen gun before removing the vacuum. This process showed excellent results and there was no PMMA visibly removed from the wafer.

The next quartz wafer was therefore processed the same way as was done with the third dummy wafer. However, when cutting the wafer in the x-direction towards the flats, there was some water collecting underneath the wafer. When cutting in the y-direction, the saw and wafer broke and cutting was stopped, resulting

in strips of the wafer. Upon inspection of the strips, it could be seen that the wet filtration paper removed the PMMA layer from the surface. Also, this broke the saw. The exact reason why water was collecting underneath the wafer was not clear, but this caused an increase in thickness of the filtration paper by absorption, which damaged the saw.

Since there now was only one good wafer left and the saw just broke, the decision was made to try a different way of dicing the wafers. The strips of wafer that were still good were cut into the chips by hand. Although this method resulted in messy and some broken chips, this resulted in 12 diced chips. Two of these chips were over-etched and could not be used for the original measurements, but were still hooked up to the test setup to see the results. The total yield of devices after production can be viewed in table 7.1 .

Table 7.1: The yield of the produced SAW devices

Design	**Number of useable chips**
25-500	3
50-500	2
75-500	2
25-1000	1
50-1000	2
75-1000	1
25-5000	2
50-5000	1
75-5000	2
FIDT	0

7.2. Network analyzer measurements

To determine the effect of the PCB on the measurements, PCBs without a SAW present were first connected to a network analyzer for open circuit analysis. The corresponding schematic circuit is shown in 7.3). After calibrating with an S21-through connection to correct for the loss in the cables the results were viewed. The results of these measurements are shown in figure 7.4 for a 0 dBm input.

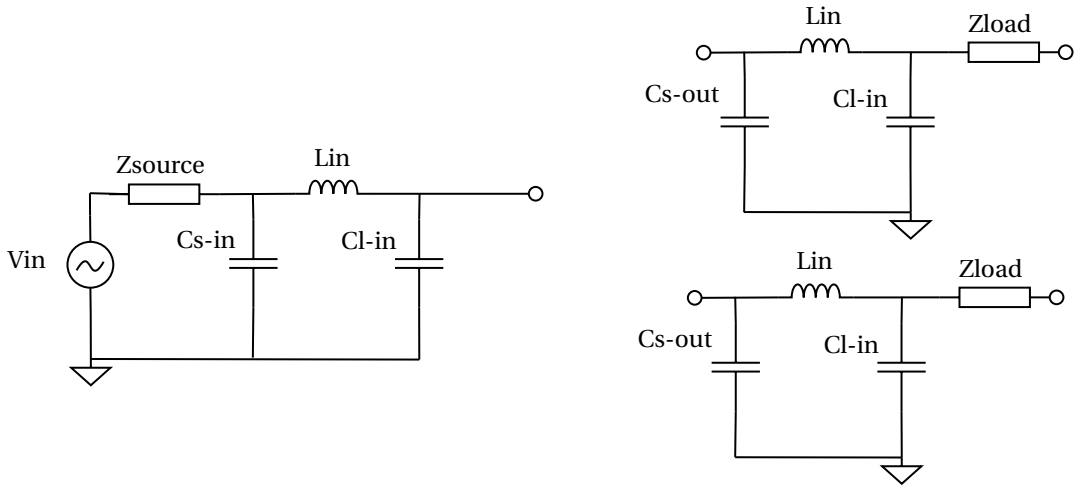

Figure 7.3: Schematic circuit of a PCB without the SAW-device connected to it. It contains the input signal (V1) the cable loads (ZL) andthe Pi-matching circuits. The circles represent the open circuit. Each PCB has to of these circuits on it, which would be able to connectto two different SAW devices independently

When connecting a PCB without a SAW device to a network analyzer, it is expected that a very high attenuation will be measured. The 400 MHz signal coming from V_{in} would in an ideal circuit only reach the inputs pi-matching circuit and none of the signals will reach either output because of the open circuit. However,

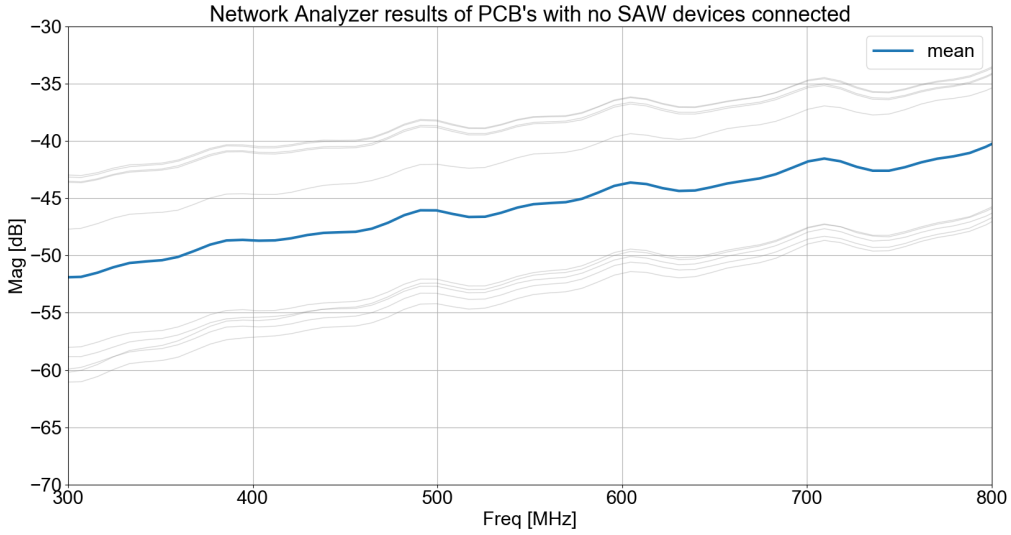

Figure 7.4: Network analyzer result of PCB without a SAW device connected to it. The grey lines represent the individual measurements of each output and the blue line shows the mean of the signals of the out and ref output respectively

figure 7.4 clearly shows a signal reaching the output of around -40 dBm at the desired range of 400 MHz. This indicates that the PCB itself is transmitting the signal from the network analyzer directly to the output.

This theory is further substantiated when connecting the input connector of the other SAW device to the input of the network analyzer. These two circuits should be completely isolated from each other, even with the presence of a SAW device. However, the network analyzer shows a clear signal.

The consequences of this become clear when the PCBs were connected that included the SAW devices (figure 7.7). Figure 7.5 shows the network analyzer plots for all measured devices together in grey. The mean of the signals is calculated and subtracted to easily compare it to PCBs that are not connected to a SAW, which is shown in figure 7.6. These results show that there is no significant difference between the output signal from a PCB with or without a SAW device, indicating that there is no resonance in this frequency range.

7.3. Spectrum Analyzer measurements

Figure 7.10 shows a selection of the measurements of the devices connected to the spectrum analyzer setup with a 400 MHz 0 dBm input signal. All the plots can be viewed in appendix C Results on the output signal magnitude and bandwidth are shown in figures 7.8 and 7.9. A selection of the spectrum analyzer plots is shown in figure 7.10. It was expected that the created surface acoustic wave would see a frequency shift, due to the mass of the PMMA that is deposited on top of each device. However, none of the measured devices show any frequency shift. Every gathered plot shows an output with the same frequency as was given at the input.

This is in accordance with the results from the network analyzer. Considering that there is a portion of the input signal directly transmitted to the output, the spectrum analyzer now measures two signals at the same time. We have seen that this interference signal is around -40 or -60 dB. Enabling the spectrum analyzer to show the SAW signal, means that this signal must be higher in amplitude than the interference signal. However, none of the spectrum analyzer results show a signal higher than -40 dB. This implies that the SAW signal is too much attenuated to be distinguished from the interference which causes no frequency shift to be seen.

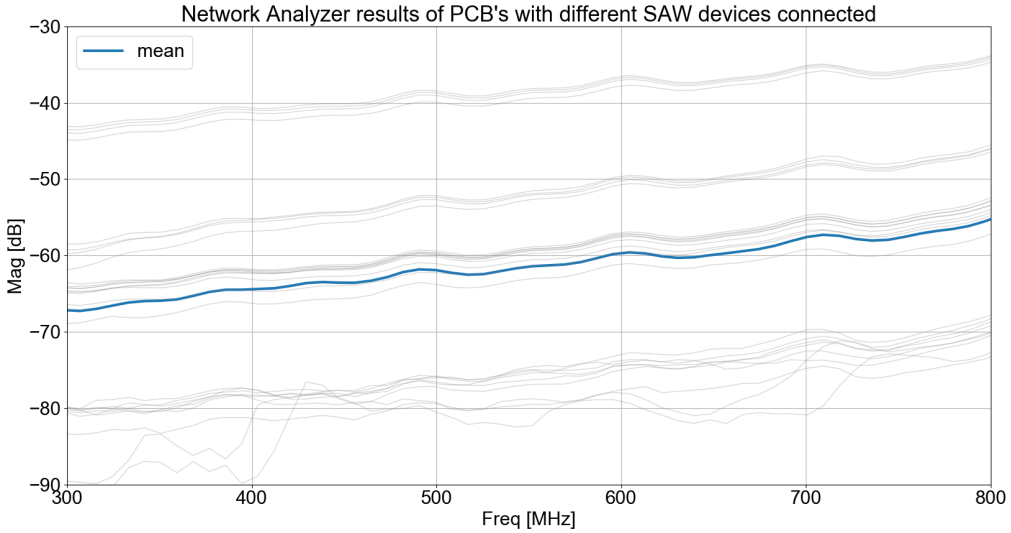

Figure 7.5: Network analyzer results of measurements on PCB's connected to a SAW device

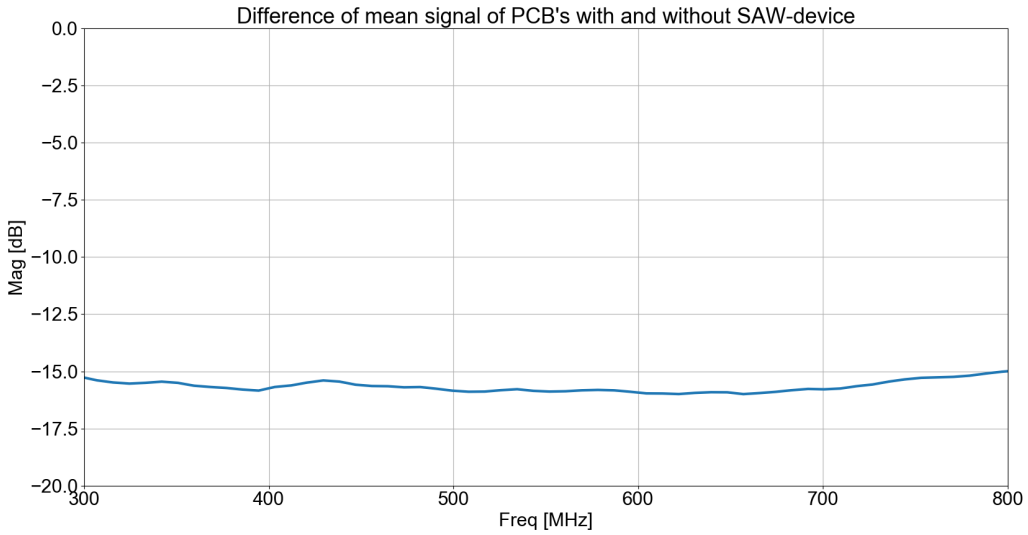

Figure 7.6: Difference of the mean signals of the network analyzer results on the PCB's with and without a SAW device

7.4. Measurements with alternate PCB

Since the measurements and the results in figure 7.6 made clear that the PCB leaked too much of the input signal directly to the output, more measurements were made with a different PCB. This PCB was a spare PCB from a different study and consists of only 3 SMA ports and direct traces to the SAW device but connecting it to a network analyzer showed a much more attenuated signal at the output. The results of a SAW device with the 75-500 design connected to the PCB are shown in figure 7.12. Although the PCB itself introduces a much more attenuated signal to the output, there is still no clear resonance that can be observed.

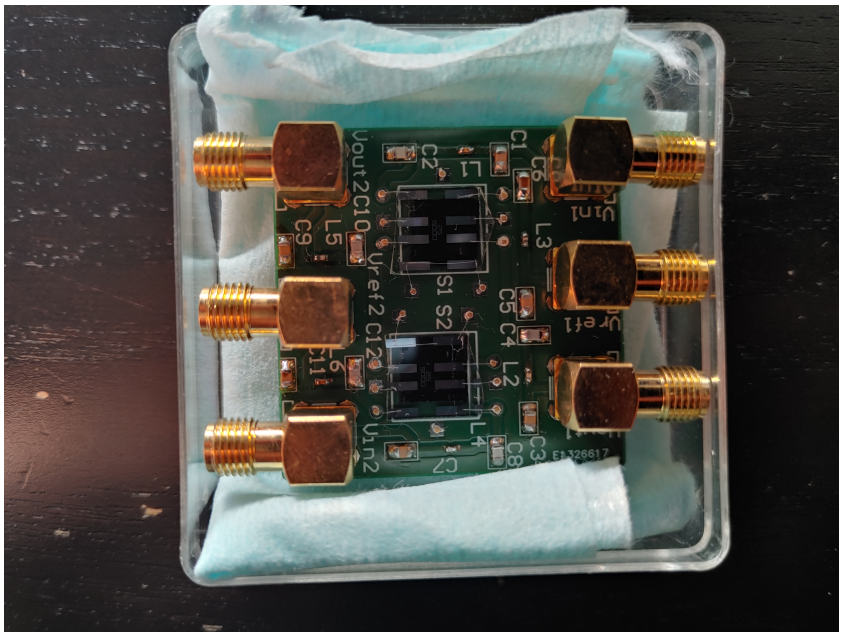

Figure 7.7: Two SAW devices (in the white squares), connected to the PCB

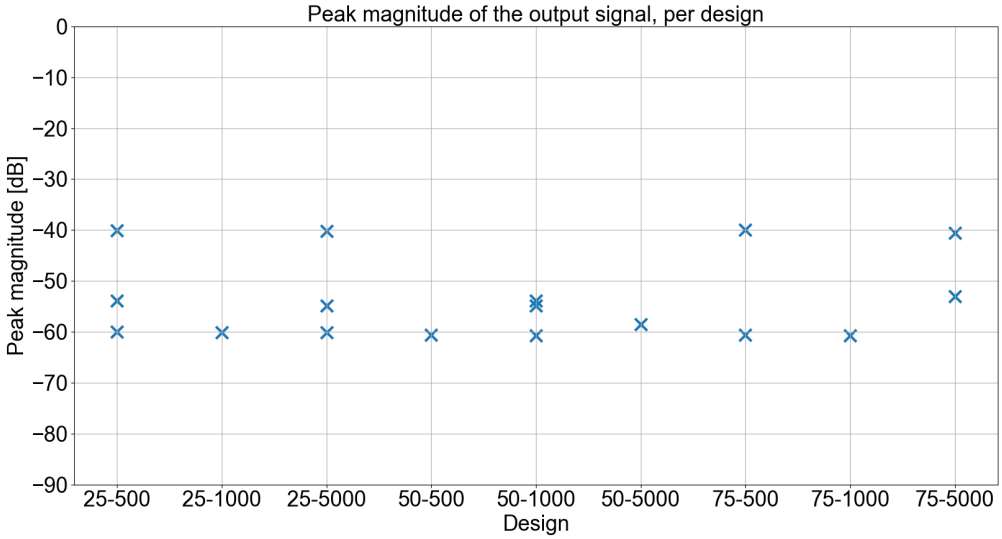

Figure 7.8: Peak magnitudes at 400 MHz, devided by sensor design

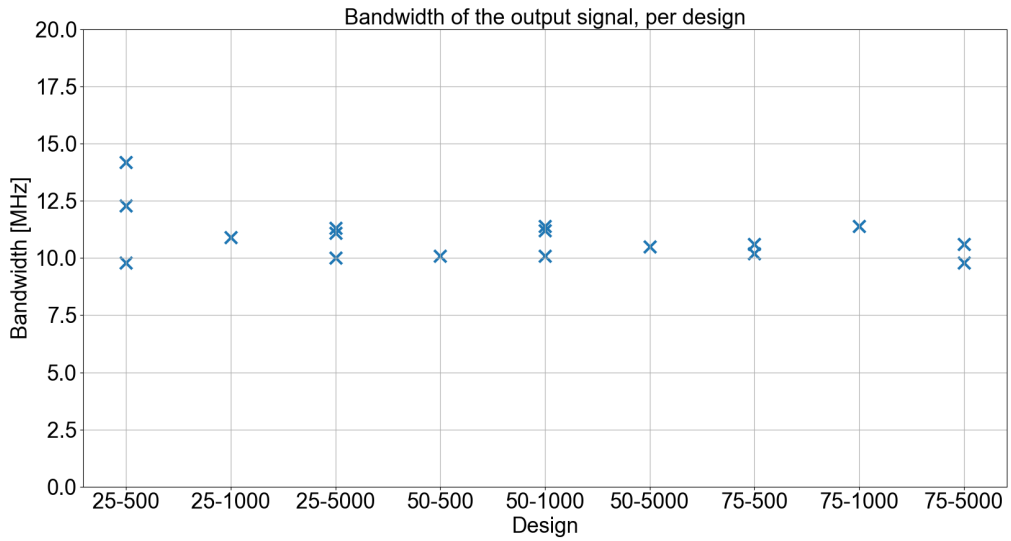

Figure 7.9: Output bandwidth at 400 MHz, devided by sensor design

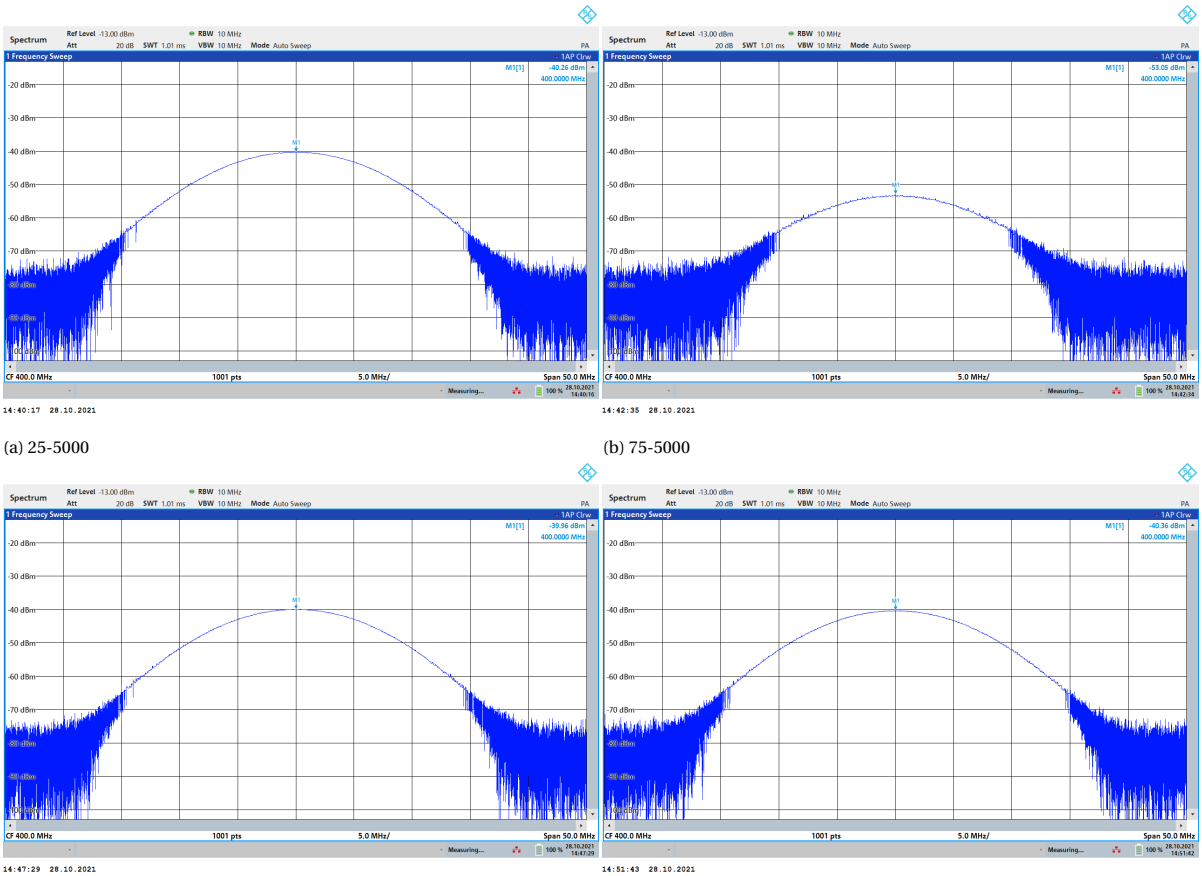

(a) 25-5000

(b) 75-5000

(c) 75-500

(d) 50-1000

Figure 7.10: Selection of the results of the spectrum analyzer. When a 400MHz signal is given at the input, no clear frequency shift at the output can be seen

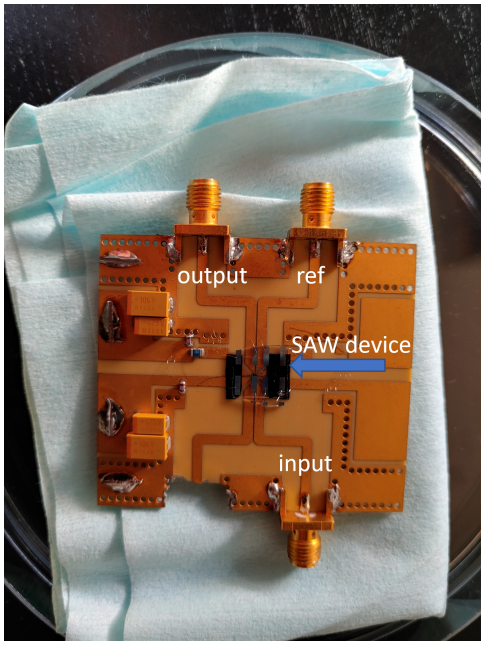

Figure 7.11: A 75-500 design SAW device connected to an alternate PCB with only SMA connectors

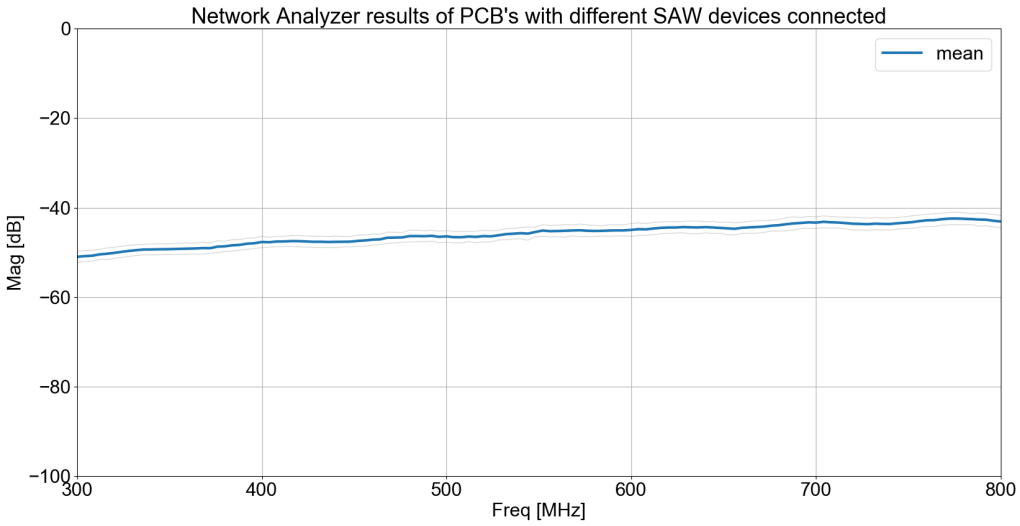

Figure 7.12: Network analyzer plot with a SAW device connected to a different PCB

8

Discussion

Results in figure 7.10 show that for a 400 MHz input signal, the measured signal at the output is unchanged in its frequency. However, a Love wave traveling through the delay line will come across mass-loading by the guiding layer. Therefore the frequency of the wave will be changed and the output IDT should measure a signal that differs from the output. Several studies have measured and reported on this effect. Newton et al. [60] performed a study where they characterized the effect of a PMMA guiding layer on a ST-cut quartz Love wave sensor. They reported a decrease of a decrease in the measured frequency between 1 and 5 MHz on a 110 MHz input signal, when the guiding layer thickness increased from 0.25 to 1.5 µm. Furthermore, Wu et al. [61] showed that the mass loading of the IDT electrodes already introduces a slight frequency shift. In this study, 0.57 µm of PMMA was deposited. Combined with the fact that we measure at a much higher frequency, it is expected a significant frequency difference would be measured.

Figure 7.5 shows that around 400 MHz, or any other frequency in the expected range, further indicating that there is no resonance peak that would be created by the SAW device.

At the beginning of this study, multiple designs were made with a different number of fingerpairs and delay lines. This would lead to a comparison of the different output signals to investigate what design would have the best performance when measuring the presence of CD-9 on the surface of the device, which will be discussed in this section. However, the measurements have led to the conclusion that no Love-wave signal can be distinguished from the background signal through the PCB. This means that there can be no reasonable comparisons made on the performance of the different designs, or proven that CD-9 can be detected in urine by means of a Love wave device. Therefore the aim of this section has shifted to investigating the possible causes as to why there are no Love-wave signals measured at the output.

8.1. Sensor Design

Different possibilities as to why there is no clear signal measured are. These possibilities will be first covered independently, followed by a discussion on their relationships to each other and the results.

8.1.1. Bandwidth

In section 3 it was established that a bandwidth of 10 MHz would be sufficient bandwidth for the output signal to detect the frequency shift of a Love mode wave. Figure 7.9 showed that the bandwidth of the measured devices was between 9.8 and 14.2 MHz for a 400MHz signal. The choice of the bandwidth was based on other studies since it was unclear how much of a frequency shift will be created. This also means that the possibility remains that the frequency shift due to the deposited PMMA is bigger than the bandwidth allows to measure. The device that is designed for this thesis, is operating on a much higher frequency than was done before in other studies which makes it more sensitive for differences in mass density on the surface. Therefore there is the possibility that the resonance frequency of the Love wave has shifted more than the bandwidth allows for.

As discussed in chapter 4.2, a lower number of fingerpairs in the IDT's will increase the bandwidth of the acoustic signal. However, when comparing the output signals of each design, the designs with the lowest number of finger pairs do not show a resonance.

8.1.2. Attenuation

Since there is no resonance frequency measured at both the network and signal analyzer, it is a reasonable possibility that the Love wave is attenuated too much throughout the delay line. Although other studies use similar or even larger delay lines, the quartz substrate is known for its low electromechanical coupling coefficient (K^2 = 0.12%) [13, 15, 62, 63]. A low electromechanical coupling coefficient introduces more insertion loss in a shear horizontal wave [40]. The addition of a PMMA guiding layer increases the electromechanical coupling coefficient but it is unclear how much it compensates for in this study. A different material that is often used for SAW devices, is lithium-niobate which has an electromechanical coupling coefficient of 0.16 [38, 64].

A different cause of attenuation of the Love wave is the delay line length. Acoustic waves are attenuated the further they travel and Love waves are no exception to this [65]. As described earlier in section 4.2.2, increasing the delay line length will allow for more anti-bodies to be captured which increases the sensitivity. To find the right balance in this trade-off, three different delay line lengths were incorporated into the designs. None of the three different delay-line lengths could read a Love wave at its output. Therefore no clear distinction can be made about the difference in performance in the different delay line lengths. Just as with the different number of fingerpairs however, there still is the possibility that the delay line should be even shorter to decrease the attenuation in the delay line. When comparing the delay line with other studies with Love-wave sensors for the detection of biomolecules, this seems unlikely. Viespe et al. [66] used a delay line of 10 mm, Francis et al. [15] a 5 mm delay line and Newton et al. [60] a 7.2 mm delay line, all with good results.

8.1.3. IDT design

During the design stage of creating the SAW device, the decision was made to use a standard IDT structure. This would reduce the complexity of the design which is beneficial when creating a SAW device from scratch. However, the standard IDT structure has the downside that it is bidirectional. It does not only create surface waves into the delay line but in the opposite direction as well. As a consequence, half of the wave's energy is lost which means that the input signal already suffers from a 3dB loss. This can be dealt with in two ways: adding Bragg reflectors behind the input IDT or by changing the IDT structure itself to make it unidirectional [13].

Making a reflector is done by creating grating of materials behind the IDT structure with alternate high and low acoustic impedances [67]. This can easily be done by placing metal strips behind each other spaced by one wavelength. If the reflector is placed an integer N times the wavelength behind the IDT structure, the reflected wave will be in phase with the wave going into the waveguide and reduced the loss induced by a bidirectional IDT design.

Limiting bidirectional wave emission can be done in the IDT itself as well, by using a couple of techniques. The first technique is using split IDT's (see figure 8.1a). By alternating two of the fingers of the same polarity instead of one, a small part of the wave in the backward direction will be reflected [13]. Another technique is using single-phase unidirectional transducers (SPUDT's). Here, two adjacent finger widths are used. By making one finger a quarter of the wavelength and the other one-eighth of the wavelength, the wave will be created in one direction and reflected in the other direction(figure 8.1b) [68].

8.2. PCB performance

Results of measurements including the PCB have shown that the signal going through the SAW device was too weak to be distinguished from the leakage signal of the PCB. To solve this, one can either redesign the PCB such that the leakage signal is much lower in magnitude, reduce the attenuation of the signal in the SAW device, or a combination of the two. This section will investigate both of the options

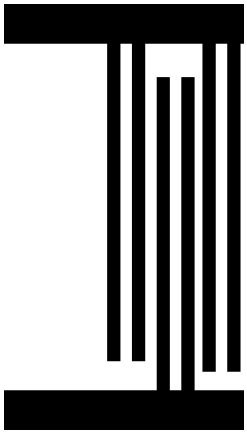

(a) Split IDT structure

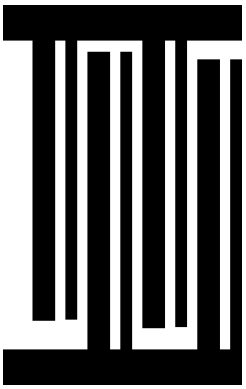

(b) SPUDT IDT structure

8.2.1. Reducing RF leakage in PCB

Connecting the PCB circuits without the SAW device to the network analyzer showed that, depending on the output channel, a -40 dB and -60 dB signal was measured at the output. Since a SAW-less PCB should behave like an open circuit, clearly there is significant leakage that interfered with the measurements.

Because the signal that is sent to the input port of the PCB is in the RF range, it is necessary to take into account the effects of capacitive coupling, radiated coupling and leakage. During the design of the PCB, these measures were taken to limit these effects, but this proved to be insufficient and a more careful PCB design is required.

Capacitive coupling Capacitive coupling occurs when a signal carrying trace is placed next to a different trace. Even though there is no physical connection between the two lines, there is still a capacitive connection between the two. If the frequency of the input signal is sufficiently high, the electric field around the input trace will induce the signal at the other trace. A common way to prevent this is by shielding the traces. Placing a grounded conductive material between the two traces will break the electronic field and prevent electrostatic coupling.

Figure 8.2 shows the top layer of the PCB taken from the design software (Circuitmaker version 2.0.3). The traces (orange) are separated from ground by a dielectric. The remaining space has been filled with conductive material which is connected to the PCB's ground. This is also connected to an additional ground plane placed on the bottom side of the PCB, increasing the surface area of the ground (shown in figure 8.2 in blue). This reduces the capacitive coupling between the different traces, but it is possible that this was not enough.

Radiated coupling When designing a PCB for RF use, it is important to take into account that radiated coupling can interfere with the signal. At these frequencies, conductors can behave like an antenna and transmit the signal to the output port by electromagnetic radiation. Good practice at RF line routing are: traces are short and straight, as few abrupt changes as possible, drill as few holes as possible and add as many ground vias as possible around the RF signal line [69].

During the design of the PCB, these factors were taken into account as much as possible. Most lines are very straight, but sometimes it was not possible to keep everything straight due to a lack of surface area to work with. For example, the input line powers two devices at once and therefore has two separate pads to connect with a device's input IDT (figure 8.3). Since a ground pad needed to be placed in between the input pads, it was not possible to connect them with a straight trace. Instead, they were connected using a bypass structure introducing more corners. This may have led to loss in the input signal and interference in the output signal. An alternative trace that could have been made is drawn in red in figure 8.3. This keeps the trace straighter and decreases the loss of the signal.

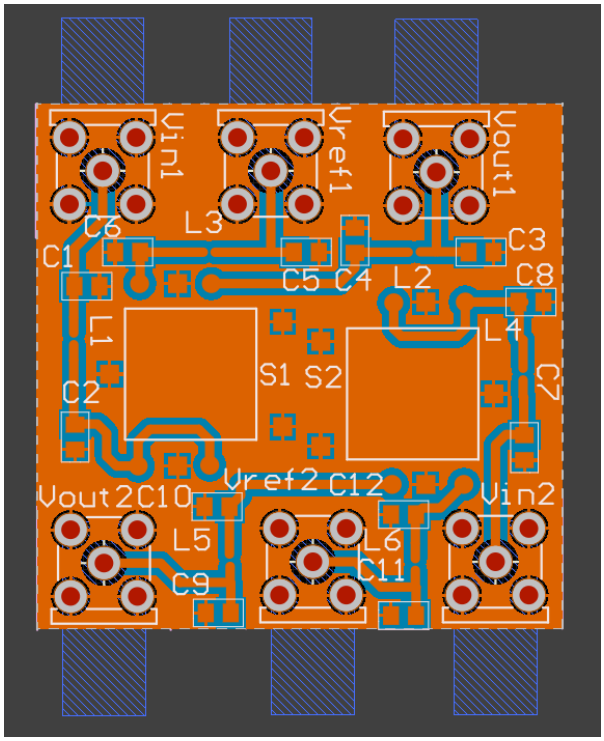

Figure 8.2: Top view of the PCB design. It shows the different traces and the ground plane that is in between them.

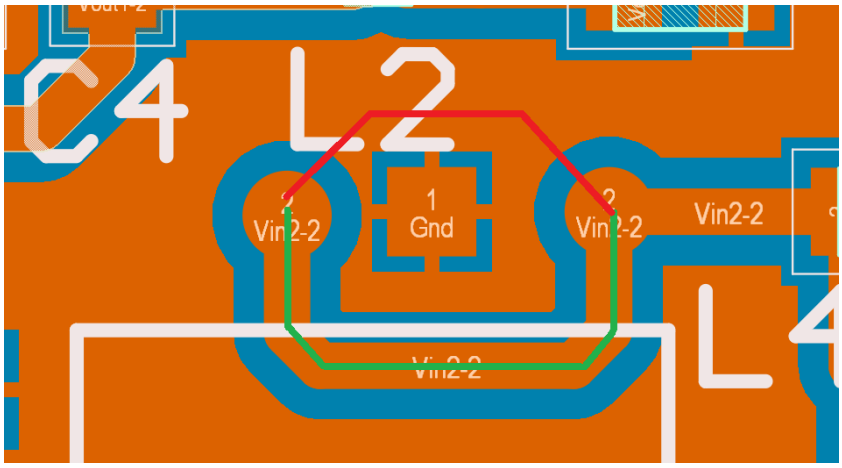

Figure 8.3: The connection between two pads which transmits the signal to the input IDT's of the two SAW devices on a SAW chip. The trace is highlighted by a green line. The red line shows an alternate path that would lead to fewer corners

A different way to reduce radiated coupling is to keep the traces as short as possible. Although it was the goal during design to adhere to this, different layouts may lead to shorter traces which will improve the PCB performance.

Probe station measurements The SAW device was in this thesis designed to be connected to a network analyzer and spectrum analyzer, with an impedance matching circuit to improve power transfer to and from the sensor. Since wire-bonding was used to electrically connect the PCBs and the contact pads on the SAW device, the choice was made to create large (1x3 mm) aluminium contacts. This allows for easier connection using the wire bonding machine. However, this configuration does not allow for a probe station to be used as well. This requires contact pads where the ground and input/output are a few micrometers removed from each other.

A probe station would be able to accurately characterize the device performance independent of the PCB. Especially with the results presented here, it is interesting to investigate the characteristics using the probe station. Future research should therefore include contact pads that have dimensions that allow for probe station measurements.

8.3. Simulation improvements

While reviewing the simulations done to determine the resonance frequency of the SAW device, it came apparent that an error has been made. To simulate the properties of ST-cut quartz, a rotated system has been introduced which gives the quartz material the correct orientation. The chosen Euler angles were based on the orientation used for ST-cut quartz crystal growth, as described in [53, 54]. However, later review revealed that there is a confusing conversion of these angles to Euler angles: (0, (42.75+90)°, 0) [70]. This means that although the simulations showed evidence of Love waves, the model's quartz substrates orientation is different than that of the quartz wafer used during production. Redoing simulations using this rotated system shows a much higher resonance frequency of 630 MHz. This error has cascaded through parts of the design, like determining the waveguide thickness and the calculation of the impedance matching circuit. Sadly, this realization was made too late into the study to redesign, create and test a new version of the SAW design based on new simulations and calculations. Instead, the consequences of the results will be discussed here for future research.

Since the new simulation show a higher resonance frequency than was expected, the simulations on the waveguide thickness needs to be redone as well. However, in the short time that was left for this study, we did not succeed in finding a new optimal thickness for the waveguide. It is therefore possible that PMMA layer attenuates the shear horizontal waves created on the quartz substrate, rather than capturing them. More extensive simulations need to be done to makes sure if this is the case.

Using a different resonance frequency for the calculation of the impedance matching circuit has some important consequences on the input and output signal. Figure shows that the output signal around 600 MHz is -136 dB, completely removing the signal from the output. This could potentially explain the results seen when connecting the devices to a network analyzer and spectrum analyzer. However, there are also measurements done with an alternate PCB without any impedance matching components, which also do not show a resonance peak around 600 MHz when connected to the network analyzer. This indicates that although the PCB cancels out the frequency at which the Love wave is created, the Love wave itself is too much attenuated as well. Future iterations on this SAW device design therefore still have to focus on decreasing signal attenuation in the delay line.

8.4. Future research

Although the created SAW devices did not work like expected, a lot was learned on how to improve for future iterations. Earlier, several propositions have been made for future iterations. In summary, this is:

1. increase the bandwidth of the output signal to allow for a bigger frequency shift
2. focus on decreasing attenuation of the acoustic wave in the piezoelectric substrate
3. experiment with different IDT structures which are able to create a focused and/or unidirectional wave
4. improve simulations to get more representative results
5. reduce RF leakage in the PCB
6. Include experiments using a probe station

9

Conclusion

This study described the design of a surface acoustic wave sensor to detect urinary CD-9. Multiple wave-modes and materials were investigated and the choice was made to create a Love mode SAW device consisting of an ST-quartz substrate, PMMA waveguide and aluminium IDT's. Comsol simulations were performed to determine the resonance frequency and waveguide thickness, which were 400 MHz and 560 nm respectively.

Despite promising simulations, no resonance frequencies could be seen on the network analyzer. When connecting to a spectrum analyzer, it was expected that a frequency shift due to mass-loading of PMMA and aluminium would be seen. However, the result showed the same input and output frequency. Therefore the created design cannot act as a proof-of-concept for a SAW sensor to detect CD-9 out of urine.

These results indicated that the signal produced by the SAW wave sensor is too much attenuated to be measured by either the network analyzer or the spectrum analyzer. A low device yield due to difficulties during production and a limited time resulted in little room to redesign and test possible causes. Future work should focus on investigating ways to decrease attenuation and improve Love-wave creation. Proposed ways to do this include increasing the bandwidth to allow have a bigger interval to detect frequency changes, considering using different materials with better electromechanical coupling coefficients, performing improvements on the simulations, introducing reflectors and different IDT designs to decrease bidirectional wave emission and redesigning the PCB to decrease the signal leaking through.

Bibliography

[1] K. Länge, B. E. Rapp, and M. Rapp, "Surface acoustic wave biosensors: A review," *Analytical and Bioanalytical Chemistry*, vol. 391, no. 5, pp. 1509–1519, 2008.

[2] GCO, "Estimated number of new cases in 2021, worldwide, males, ages 55+," 2021. [Online]. Available: https://gco.iarc.fr/today

[3] P. Stichting, "Onderzoek en diagnose bij prostaatkanker," 2021. [Online]. Available: https://prostaatkankerstichting.nl/prostaatkanker/onderzoek-en-diagnose-bij-prostaatkanker/

[4] D. Ilic, M. Djulbegovic, J. H. Jung, E. C. Hwang, Q. Zhou, A. Cleves, T. Agoritsas, and P. Dahm, "Prostate cancer screening with prostate-specific antigen (PSA) test: a systematic review and meta-analysis." *BMJ (Clinical research ed.)*, vol. 362, p. k3519, 9 2018.

[5] J. T. Wei, "Urinary biomarkers for prostate cancer," *Current Opinion in Urology*, vol. 25, no. 1, pp. 77–82, 1 2015. [Online]. Available: http://journals.lww.com/00042307-201501000-00014

[6] S. S. Wilson and E. D. Crawford, "Screening for prostate cancer," *Clinical Prostate Cancer*, vol. 3, no. 1, pp. 21–25, 2004. [Online]. Available: http://dx.doi.org/10.3816/CGC.2004.n.008

[7] F. M. Wagenlehner, E. Van Oostrum, P. Tenke, Z. Tandogdu, M. Çek, M. Grabe, B. Wullt, R. Pickard, K. G. Naber, A. Pilatz, W. Weidner, and T. E. Bjerklund-Johansen, "Infective complications after prostate biopsy: Outcome of the Global Prevalence Study of Infections in Urology (GPIU) 2010 and 2011, A prospective multinational multicentre prostate biopsy study," *European Urology*, vol. 63, no. 3, pp. 521–527, 2013.

[8] B. Liu, X. Chen, H. Cai, M. A. Mohammad, X. Tian, L. Tao, Y. Yang, and T. Ren, "Surface acoustic wave devices for sensor applications," *Journal of Semiconductors*, vol. 37, no. 2, pp. 1–9, 2016.

[9] K. Fujita and N. Nonomura, "Urinary biomarkers of prostate cancer," pp. 770–779, 9 2018. [Online]. Available: http://doi.wiley.com/10.1111/iju.13734

[10] M. E. Hemler, "Tetraspanin functions and associated microdomains," *Nature Reviews Molecular Cell Biology*, vol. 6, no. 10, pp. 801–811, 2005.

[11] D. Duijvesz, C. Y. L. Versluis, C. A. M. van der Fels, M. S. Vredenbregt-van den Berg, J. Leivo, M. T. Peltola, C. H. Bangma, K. S. I. Pettersson, and G. Jenster, "Immuno-based detection of extracellular vesicles in urine as diagnostic marker for prostate cancer." *International journal of cancer*, vol. 137, no. 12, pp. 2869–2878, 12 2015.

[12] J. C. Wang, L. R. Bégin, N. G. Bérubé, S. Chevalier, A. G. Aprikian, H. Gourdeau, and M. Chevrette, "Down-regulation of CD9 expression during prostate carcinoma progression is associated with CD9 mRNA modifications," *Clinical Cancer Research*, vol. 13, no. 8, pp. 2354–2361, 2007.

[13] Y. Q. Fu, J. K. Luo, N. T. Nguyen, A. J. Walton, A. J. Flewitt, X. T. Zu, Y. Li, G. McHale, A. Matthews, E. Iborra, H. Du, and W. I. Milne, "Advances in piezoelectric thin films for acoustic biosensors, acoustofluidics and lab-on-chip applications," *Progress in Materials Science*, vol. 89, pp. 31–91, 2017.

[14] M. J. Vellekoop, "Acoustic wave sensors and their technology," *Ultrasonics*, vol. 36, no. 1-5, pp. 7–14, 1998.

[15] L. A. Francis, J. M. Friedt, R. De Palma, C. Zhou, C. Bartic, A. Campitelli, and P. Bertrand, "Techniques to evaluate the mass sensitivity of Love mode surface acoustic wave biosensors," *Proceedings of the IEEE International Frequency Control Symposium and Exposition*, vol. 00, no. c, pp. 241–249, 2005.

[16] T. Wang, R. Green, R. R. Nair, M. Howell, S. Mohapatra, R. Guldiken, and S. S. Mohapatra, "Surface acoustic waves (SAW)-based biosensing for quantification of cell growth in 2D and 3D Cultures," *Sensors (Switzerland)*, vol. 15, no. 12, pp. 32 045–32 055, 2015.

[17] F. Zhang, S. Li, K. Cao, P. Wang, Y. Su, X. Zhu, and Y. Wan, "A microfluidic love-wave biosensing device for PSA detection based on an aptamer beacon probe," *Sensors (Switzerland)*, vol. 15, no. 6, pp. 13 839–13 850, 2015.

[18] Y. C. Chen, W. C. Shih, W. T. Chang, C. H. Yang, K. S. Kao, and C. C. Cheng, "Biosensor for human IgE detection using shear-mode FBAR devices," *Nanoscale Research Letters*, vol. 10, no. 1, 2015.

[19] Prostate Cancer International, "Signs and symptoms of prostate cancer," 2008. [Online]. Available: https://prostatecancerinfolink.net/diagnosis/signs-symptoms-prostate-cancer/

[20] L. Naji, H. Randhawa, Z. Sohani, B. Dennis, D. Lautenbach, O. Kavanagh, M. Bawor, L. Banfield, and J. Profetto, "Digital rectal examination for prostate cancer screening in primary care: A systematic review and meta-analysis," *Annals of Family Medicine*, vol. 16, no. 2, pp. 149–154, 2018.

[21] T. Tuytten and R. Raaijmakers, "Het oncologie formularium," in *Het oncologie formularium*. Houten: Bohn Stafleu van Loghum, 2015, ch. 1. [Online]. Available: https://mijn.bsl.nl/prostaatkanker/747182

[22] J. Streicher, B. L. Meyerson, V. Karivedu, and A. Sidana, "A review of optimal prostate biopsy: indications and techniques," *Therapeutic Advances in Urology*, vol. 11, no. 6, p. 175628721987007, 1 2019. [Online]. Available: http://journals.sagepub.com/doi/10.1177/1756287219870074

[23] S. Loeb, A. Vellekoop, H. U. Ahmed, J. Catto, M. Emberton, R. Nam, D. J. Rosario, V. Scattoni, and Y. Lotan, "Systematic review of complications of prostate biopsy," *European Urology*, vol. 64, no. 6, pp. 876–892, 2013. [Online]. Available: http://dx.doi.org/10.1016/j.eururo.2013.05.049

[24] S. P. Balk, Y. J. Ko, and G. J. Bubley, "Biology of prostate-specific antigen," *Journal of Clinical Oncology*, vol. 21, no. 2, pp. 383–391, 2003.

[25] E. Engvall and P. Perlmann, "Enzyme-linked immunosorbent assay, Elisa. 3. Quantitation of specific antibodies by enzyme-labeled anti-immunoglobulin in antigen-coated tubes." *Journal of immunology (Baltimore, Md. : 1950)*, vol. 109, no. 1, pp. 129–35, 1972. [Online]. Available: http://www.ncbi.nlm.nih.gov/pubmed/4113792

[26] S. Sakamoto, W. Putalun, S. Vimolmangkang, W. Phoolcharoen, Y. Shoyama, H. Tanaka, and S. Morimoto, "Enzyme-linked immunosorbent assay for the quantitative/qualitative analysis of plant secondary metabolites," *Journal of Natural Medicines*, vol. 72, no. 1, pp. 32–42, 2018. [Online]. Available: https://doi.org/10.1007/s11418-017-1144-z

[27] R. Schiavina, F. Chessa, M. Borghesi, C. Gaudiano, L. Bianchi, B. Corcioni, P. Castellucci, F. Ceci, I. Ceravolo, G. Barchetti, M. Del Monte, R. Campa, C. Catalano, V. Panebianco, C. Nanni, S. Fanti, A. Minervini, A. Porreca, and E. Brunocilla, "State-of-the-art imaging techniques in the management of preoperative staging and re-staging of prostate cancer," *International Journal of Urology*, vol. 26, no. 1, pp. 18–30, 2019.

[28] Y. Murayama, K. Oritani, and S. Tsutsui, "Novel CD9-targeted therapies in gastric cancer," *World Journal of Gastroenterology*, vol. 21, no. 11, pp. 3206–3213, 2015.

[29] E. Killick, R. Morgan, F. Launchbury, E. Bancroft, E. Page, E. Castro, Z. Kote-Jarai, A. Aprikian, I. Blanco, V. Clowes, S. Domchek, F. Douglas, D. Eccles, D. G. Evans, M. Harris, J. Kirk, J. Lam, G. Lindeman, G. Mitchell, N. Pachter, C. Selkirk, K. Tucker, J. Zgajnar, R. Eeles, and H. Pandha, "Role of Engrailed-2 (EN2) as a prostate cancer detection biomarker in genetically high risk men," *Scientific Reports*, vol. 3, pp. 1–5, 2013.

[30] H. Pandha, K. D. Sorensen, T. F. Orntoft, S. Langley, S. Hoyer, M. Borre, and R. Morgan, "Urinary engrailed-2 (EN2) levels predict tumour volume in men undergoing radical prostatectomy for prostate cancer," *BJU International*, vol. 110, no. 6B, pp. 287–292, 2012.

[31] R. Morgan, A. Boxall, A. Bhatt, M. Bailey, R. Hindley, S. Langley, H. C. Whitaker, D. E. Neal, M. Ismail, H. Whitaker, N. Annels, A. Michael, and H. Pandha, "Engrailed-2 (EN2): A tumor specific urinary biomarker for the early diagnosis of prostate cancer," *Clinical Cancer Research*, vol. 17, no. 5, pp. 1090–1098, 2011.

[32] P. J. Jandas, J. Luo, K. Prabakaran, F. Chen, and Y. Q. Fu, "Highly stable, love-mode surface acoustic wave biosensor using Au nanoparticle-MoS2-rGO nano-cluster doped polyimide nanocomposite for the selective detection of carcinoembryonic antigen," *Materials Chemistry and Physics*, vol. 246, no. February, p. 122800, 2020. [Online]. Available: https://doi.org/10.1016/j.matchemphys.2020.122800

[33] O. Onen, A. Sisman, N. D. Gallant, P. Kruk, and R. Guldiken, "A urinary Bcl-2 surface acoustic wave biosensor for early ovarian cancer detection," *Sensors (Switzerland)*, vol. 12, no. 6, pp. 7423–7437, 2012.

[34] O. Tigli, L. Bivona, P. Berg, and M. E. Zaghloul, "Fabrication and characterization of a surface-acoustic-wave biosensor in cmos technology for cancer biomarker detection," *IEEE Transactions on Biomedical Circuits and Systems*, vol. 4, no. 1, pp. 62–73, 2010.

[35] J. Du, G. L. Harding, J. A. Ogilvy, P. R. Dencher, and M. Lake, "A study of Love-wave acoustic sensors," *Sensors and Actuators, A: Physical*, vol. 56, no. 3, pp. 211–219, 1996.

[36] E. Gizeli, F. Bender, A. Rasmusson, K. Saha, F. Josse, and R. Cernosek, "Sensitivity of the acoustic waveguide biosensor to protein binding as a function of the waveguide properties," *Biosensors and Bioelectronics*, vol. 18, no. 11, pp. 1399–1406, 2003.

[37] H.-K. Oh, W. Wang, K. Lee, C. Min, and S. Yang, " The development of a wireless Love wave biosensor on 41° YX LiNbO 3 ," *Smart Materials and Structures*, vol. 18, no. 2, p. 025008, 2009.

[38] M. I. Gaso Rocha, Y. Jimenez, F. A., and A. Arnau, "Love Wave Biosensors: A Review," *State of the Art in Biosensors - General Aspects*, 2013.

[39] G. Lindner, "Sensors and actuators based on surface acoustic waves propagating along solid-liquid interfaces," *Journal of Physics D: Applied Physics*, vol. 41, no. 12, 2008.

[40] Y. Y. Chen, J. C. Hsu, and T. T. Wu, "Study on electromechanical coupling coefficients of surface acoustic waves in layered systems," *Journal of the Chinese Institute of Engineers, Transactions of the Chinese Institute of Engineers,Series A/Chung-kuo Kung Ch'eng Hsuch K'an*, vol. 27, no. 6, pp. 823–833, 2004.

[41] Y. J. Hsiao, T. H. Fang, Y. H. Chang, Y. S. Chang, and S. Wu, "Surface acoustic wave characteristics and electromechanical coupling coefficient of lead zirconate titanate thin films," *Materials Letters*, vol. 60, no. 9-10, pp. 1140–1143, 2006.

[42] B. Jakoby and M. J. Vollekoop, "Substrates for zero temperature coefficient Love wave sensors," *IEEE Transactions on Ultrasonics, Ferroelectrics, and Frequency Control*, vol. 47, no. 3, pp. 701–705, 2000.

[43] S. Li, Y. Wan, C. Fan, and Y. Su, "Theoretical study of monolayer and double-layer waveguide love wave sensors for achieving high sensitivity," *Sensors (Switzerland)*, vol. 17, no. 3, 2017.

[44] M. R. Zakaria, U. Hashim, R. Mat Ayub, and T. Adam, "Design and Fabrication of IDT SAW by using conventional lithography technique," *Middle East Journal of Scientific Research*, vol. 18, no. 9, pp. 1281–1285, 2013.

[45] T. T. Wu and I. H. Chang, "Actuating and detecting of microdroplet using slanted finger interdigital transducers," *Journal of Applied Physics*, vol. 98, no. 2, 2005.

[46] N. F. Naumenko, "Optimization of aperture in SAW and STW resonators on langasite," *IEEE International Ultrasonics Symposium, IUS*, vol. 2, no. 2, pp. 2059–2062, 2014.

[47] T. T. Wu, H. T. Tang, Y. Y. Chen, and P. L. Liu, "Analysis and design of focused interdigital transducers," *IEEE Transactions on Ultrasonics, Ferroelectrics, and Frequency Control*, vol. 52, no. 8, pp. 1384–1392, 2005.

[48] J. B. Green and G. S. Kino, "SAW Convolvers Using Focused Interdigital Transducers," *IEEE Transactions on Sonics and Ultrasonics*, vol. 30, no. 1, pp. 43–50, 1983.

[49] A. Siddiqui, R. H. Olsson, and M. Eichenfield, "Lamb wave focusing transducer for efficient coupling to wavelength-scale structures in thin piezoelectric films," *Journal of Microelectromechanical Systems*, vol. 27, no. 6, pp. 1054–1070, 2018.

[50] E. Gizeli, N. J. Goddard, C. R. Lowe, and A. C. Stevenson, "A Novel Love-Plate Acoustic Sensor Utilizing Polymer Overlayers," *IEEE Transactions on Ultrasonics, Ferroelectrics, and Frequency Control*, vol. 39, no. 5, pp. 657–659, 1992.

[51] B. Jakoby and M. J. Vellekoop, "Properties of love waves: Applications in sensors," *Smart Materials and Structures*, vol. 6, no. 6, pp. 668–679, 1997.

[52] D. Greve and M. Herring Jensen, "Modeling Surface Acoustic Wave Sensors," 2018. [Online]. Available: https://www.comsol.com/video/modeling-surface-acoustic-wave-sensors-in-comsol-multiphysics-feb-02-2018

[53] T. Thien, J. David, T. Digest, E. Bresnahan, N. Uas, R. U. S. A. Data, P. Examiner, and R. Kunemund, "United States Patent (19)," no. 19, 1999.

[54] S. Wang, L. Zhang, L. Xie, B. Huang, A. Zhang, J. Du, R. Wu, J. Wang, and Y. K. Yong, "Novel Quartz Crystal Cuts for SAW Substrates with Cubic Frequency-Temperature Relations," *IEEE International Ultrasonics Symposium, IUS*, vol. 2018-Octob, no. March 2019, 2018.

[55] L. Liljeholm, "Electroacoustic evaluation of thin film piezoelectric resonators for frequency control and sensing applications," 2005.

[56] J. F. Rosenbaum, *Bulk Acoustic Wave Theory and Devices*, 1st ed. Boston: Artech House, 1988.

[57] Silicon Labs, "AN1275 : Impedance Matching Network Architectures." [Online]. Available: https://www.silabs.com/documents/public/application-notes/an1275-imp-match-for-network-arch.pdf

[58] A. Vesel, K. Elersic, and M. Mozetic, "Immobilization of protein streptavidin to the surface of PMMA polymer," *Vacuum*, vol. 86, no. 6, pp. 773–775, 2012. [Online]. Available: http://dx.doi.org/10.1016/j.vacuum.2011.07.019

[59] E. A. o. Urology, "SOP Collection of Urine After DRE," pp. 1–6, 2018. [Online]. Available: https://uroweb.org/wp-content/uploads/SOP_EMC_EAU-RF-Collection-of-Urine-after-DRE-for-prostate.pdf

[60] M. I. Newton, P. Roach, and G. McHale, "ST quartz acoustic wave sensors with sectional guiding layers," *Sensors*, vol. 8, no. 7, pp. 4384–4391, 2008.

[61] C. Wu, "Fabrication of surface acoustic wave sensors for early cancer detection," *National Nanotechnology Infrastructure Network*, pp. 28–29, 2006. [Online]. Available: http://www.nnin.org/sites/default/files/files/NNINreu06Wu.pdf

[62] H. F. Pang, Y. Q. Fu, Z. J. Li, Y. Li, J. Y. Ma, F. Placido, A. J. Walton, and X. T. Zu, "Love mode surface acoustic wave ultraviolet sensor using ZnO films deposited on 36° Y-cut LiTaO3," *Sensors and Actuators, A: Physical*, vol. 193, pp. 87–94, 2013. [Online]. Available: http://dx.doi.org/10.1016/j.sna.2013.01.016

[63] Z. Xu and Y. J. Yuan, "Implementation of guiding layers of surface acoustic wave devices: A review," *Biosensors and Bioelectronics*, vol. 99, no. April 2017, pp. 500–512, 2018. [Online]. Available: http://dx.doi.org/10.1016/j.bios.2017.07.060

[64] D. W. Branch and S. M. Brozik, "Low-level detection of a Bacillus anthracis simulant using Love-wave biosensors on 36°YX LiTaO3," *Biosensors and Bioelectronics*, vol. 19, no. 8, pp. 849–859, 2004.

[65] C. Gruber, A. Binder, and M. Lenzhofer, "Fast Phase Analysis of SAW Delay Lines," 2016, vol. 1, pp. 373–382. [Online]. Available: http://link.springer.com/10.1007/978-3-319-47075-7_42

[66] C. Viespe, V. Dinca, G. Popescu-Pelin, and D. Miu, "Love wave surface acoustic wave sensor with laser-deposited nanoporous gold sensitive layer," *Sensors (Switzerland)*, vol. 19, no. 20, 2019.

[67] A. Arnau, *Piezoelectric transducers and applications (Google eBook)*, 2008. [Online]. Available: http://books.google.com/books?id=az1RYaJr5HsC&pgis=1

[68] H. Nakamura, T. Yamada, T. Ishizaki, and K. Nishimura, "A new design concept for low-loss SAW filters based on different-width split-finger SPUDT," *IEEE Transactions on Microwave Theory and Techniques*, vol. 49, no. 4 II, pp. 761–768, 2001.

[69] J. Panel, "3 Tips for RF PCB Layout," 2020. [Online]. Available: https://www.jrpanel.com/engineerhome/keyword/JRPanel__Tips_for_RF_PCB_Layout.html

[70] C. S. Lam, C. S. Lam, Y. C. Wang, Y. C. Wang, S. M. Wang, and S. M. Wang, "A Review of the Recent Development of Temperature Stable Cuts of Quartz for SAW Applications," *Ultrasonics*, vol. 1, pp. 1–7, 2010.

A

Literature Review

Detection of Urinary Prostate Cancer Biomarkers by the means of a Surface Acoustic Wave sensor

a Literature Review

by

M. Zijlmans

Student number: 4691717
Master: Biomedical Engineering
Track: Medical Devices & Bioelectronics

Supervisors:
Prof. dr. P.J. French
Bioelectronics laboratory
EWI faculty
Technical University Delft

Dr. ir E. Korkmaz,
Research group Smart Sensor Sytems
Faculty of Technology, Innovation and Society
The Hague University of Applied Sciences

Assist. Prof. Dr. A. Şişman,
Electrical and Electronics Engineering Department
Faculty of Engineering
Sabanci University
and
Nanotechnology Research and Application Center
Sabanci University

Frontpage image taken from [1]

TU Delft

Acknowledgements

I would like to thank Erdal Korkmaz for creating and facilitating this exciting thesis subject, as well for his great enthusiasm and positive input during the literature study. I would like to thank Paddy French as well for guiding me through the process of writing the literature study and his help organizing this thesis within the TU Delft. Finally, I would like to thank Alper Şişman for his great enthusiasm and expertise during the several insightful meetings that took place during this literature study.

Maarten Zijlmans

Delft, 23-12-2020

Contents

1 Introduction 1
1.1 Motivation . . . 1
1.2 Problem Statement . . . 3
1.3 Report Outline . . . 3

2 Method 4
2.1 On the design of a SAW device . . . 4
2.2 on prostate cancer biomarkers . . . 5

3 SAW sensor 7
3.1 Surface Acoustic Waves . . . 7
3.1.1 sensing change in mass by change in frequency . . . 8
3.2 Wave modes . . . 9
3.2.1 Rayleigh waves . . . 9
3.2.2 Lamb waves . . . 10
3.2.3 Shear Horizontal Surface Acoustic Waves . . . 11
3.2.4 Love waves . . . 12
3.2.5 Choosing the wave mode . . . 12
3.3 Materials . . . 13
3.3.1 substrate . . . 13
3.3.2 Waveguide . . . 14
3.4 IDT design . . . 18
3.4.1 basic IDT configuration . . . 18
3.4.2 IDT electrical properties . . . 18
3.4.3 different IDT configurations . . . 19
3.4.4 Focused IDT configuration . . . 20
3.4.5 Discussion . . . 21
3.5 Conclusion . . . 21

4 Urinary Biomarkers for Prostate Cancer 22
4.1 Prostate Specific Antigen . . . 22
4.2 Engrailed-2 . . . 23
4.3 TMPRSS:ERG . . . 24
4.4 Conclusion . . . 25

Bibliography 26

1 Introduction

1.1. Motivation

Prostate cancer (PCa) is the most prevalent type of cancer under the global male population above the age of 55. There were an estimated 1.211.288 new cases world wide in 2018 [2]. In the Netherlands in 2019, 14.116 men were diagnosed with prostate cancer which make up 12% of the total new cancer cases [3].

In an effort to detect cancer in its early stages of development, many countries are screening males over the age of 50, although this surrounds controversy [4]. Blood tests are used to determine elevated prostate specific antigen (PSA) levels in serum as an indicator of possible presence of PCa, Benign prostate hyperplasia (BPH) also elevates PSA levels, causing these test to have a high number of false positives [5–7]. This does not only increase the time and money going into PCa testing, it also creates the need for more males to undergo further rectal exams and biopsies causing them to experience great discomfort and increase the risk of infection[8].

For several decades, multiple studies are looking into different means for testing on PCa but none have been approved for clinical use [6]. One promising emerging technology is the use of Surface Acoustic Waves (SAW) for biosensing applications [9]. Several studies have investigated the potential use of SAW sensors to detect biomarkers that indicate the presence of breast, ovarian and prostate cancer [10–12].

SAW sensors have piezoelectric substrates that emit a certain surface-bound wave through a guiding layer, which is received at the other end. The difference between the emitted and received frequency of the wave is, among other things, a function of the mass of the guiding layer. Using this effect for sensing properties is known as gravimetric sensing. SAW sensors are used for a wide range of applications, for example as temperature, humidity, pressure, gas and as biosensors [13]. Biosensors have a coat on top of the sensing layer that immobilizes the desired analyte in a solution [1]. Using a layer of antibodies on top of the substrate allows the sensor to detect antibody-specific solutes, for example in urine. Using urine to search for the presence of cancerous tissue within the prostate allows for non-invasive, in vitro examination. There are several known biomarkers in urine that indicate the presence of cancerous tissue in the prostate, making it a promising area of research.

Investigating the possibility to measure urinary PCa biomarkers by the means of a SAW sensor, is the subject of a master thesis that follows this literature review. The goal is to design a SAW sensor

that gives a proof of concept by detecting proteins in fluids with good sensitivity and specificity. In extension, this indicates its ability to detect urinary PCa biomarkers.

1.2. Problem Statement

Using SAW sensor for biochemical sensing is a new area of research and there is no golden standard in the design specifications of the SAW sensor itself and what biomarkers to use. Therefore, this literature review is set out to answer two questions as stated below:

1. What are the relevant design considerations that need to be taken into account to create a surface acoustic wave sensor for the detection of prostate cancer biomarkers dissolved in urine, and what materials can be used to fulfill these requirements?

2. What urinary biomarkers indicate the presence of prostate cancer in the patient with a better sensitivity and specificity than prostate specific antigen?

1.3. Report Outline

First, the method used to gather and assess the relevant literature will be explained. This will be followed by first showing the results related to the design of the SAW device in chapter 3 and then into potential biomarkers that can be used in chapter 4.

2

Method

Because of the distinct fields of research concerning SAW devices and prostate cancer biomarkers, a dichotomy has been made between these topics.

2.1. On the design of a SAW device

Searching for literature on the topic of designing and the use of materials for a SAW device is broad and a lot of different researches need to be found to make validated decisions. Therefore a generic literature review was done by searching for books and other recent literature reviews (<10 years) to get insight on what the current techniques and different designs are and what design choices are to be made. From there on, more specific searches and the snowball method was used to go more in depth on the different design subjects. Search engines used for this were the TU Delft library, Google Scholar and the IEEE database

Selection criteria used to make sure the results were relevant and usefull, are:

- Language: English
- Full text available
- Article, book or chapter
- Online available

Also, some exclusion criteria were selected since the field of Surface Acoustic Waves and SAW-devices include more than is relevant for this review, shown in table 2.1

Table 2.1: Exclusion criteria on SAW design

Exclusion criteria	**Rationale**
Microfluidics	the propagation of fluidics by the mean of SAW require different design criteria then sensing solutes in fluids.
Seismic Surface Acoustic Waves	These results focus on detecting the waves themselves, not using waves as a mean of detection
Communication	SAW device in communication are used as frequency filters and have no relation to sensing

Choices that are to be made when designing a SAW sensor are not only subject to the relevant theory but also dependent on practical issues like the available techniques and materials. This literature review therefore does not make a definitive choice in materials and design. The only exception is the wave mode that is going to be used, since this lies on the very basis of the design and will affect which materials and structures are to be used.

2.2. on prostate cancer biomarkers

For the literature review on the biomarkers, first a broad search on the potential biomarkers of the moment was conducted. From this was concluded that Engrailed-2 and TMPRSS:ERG have the most potential to be usefull in the diagnosis of prostate cancer through urinary detection. Further investigation of these biomarkers, in addition to PSA as a reference, has been done by means of a systematic review, following the PRISMA diagram [14]. Search engines used for this were the TU Delft library, Google Scholar and Pubmed. Search terms are constructed based on table 2.2, which are divided in three categories. First are the keywords which have to be included in the article to be relevant for this review. The second column contains the biomarkers that came out of the exploratory research and the last column contains detection method which are related to SAW devices.

Table 2.2: Search query components

Keywords	**On Biomarker**	**On Detection**
Prostate Cancer OR PCa	PSA OR Prostate Specific Antigen	Surface Acoustic Wave OR SAW
Urine	Engrailed-2 OR EN-2	antigen
	TMPRSS:ERG	immobilization
		capturing

Search queries are constructed by combining the words in the column, seperated by an OR operator. In the first search query only the columns 'Keywords' and 'On Biomarker' are used by combining them with an AND operator. The goal for this query is to gather more in-depth results on the different biomarkers and to assess their sensitivity, specificity and their concentration in urine. For the second search query all three columns are combined with AND operators to assess the viability to use SAW devices for detection of the respective biomarkers. For some search query components a wildcard (*) is used in order to allow for an alternative ending of the word. The resulting search queries are:

- (prostate cancer OR PCa) AND urin* AND (PSA OR prostate specific antigen OR engrailed-2 OR EN-2 OR TMPRSS:ERG)
- (prostate cancer OR PCa) AND urin* AND (PSA OR prostate specific antigen OR engrailed-2 OR EN-2 OR TMPRSS:ERG) AND (surface acoustic wave OR SAW or antigen OR immobilization OR capturing)

After removing duplicates, the articles are screened firstly for their title and then for the abstract. Studies that are not focused on the study of the viability to use the biomarker as an indicator for prostate cancer will be excluded from the results. More details on the inclusion and exclusion criteria are given in table 2.3

Table 2.3: Inclusion and exclusion criteria

Criteria	**Inclusion**	**Exclusion**	**Rationale**
Language	English		The official language of the study is English
Accessibility	Full text is accessible from institute		No budget available for this study. Abstract only will give insufficient insight in used methods and results
Publication Date	After 2010		Detection methods have improved quickly, recent research more relevant
Source Type	Scientific publications		
Type of Research	Classical Article Clinical Study Journal Article	Systematic review Clinical trials Meta-analysis	

3

SAW sensor

In this chapter, the results of the literature search will be summarized and described. First a general explanation of surface acoustic waves will be given, together with how they are created and some fundamental equations that determine the quality of the device. This is followed by different wave modes that can be used, with their respective pros and cons. After a wave mode has been chosen, materials that could be used for the device's different components are described which is followed by description of different transducer designs that can be used.

3.1. Surface Acoustic Waves

SAWs are a subclassification of acoustic waves. Contrary to bulk acoustic waves (BAW), where the wave travels through the bulk of the material, SAWs are confined to the surface of a material. In order to better distinguish between different SAWs, some propose the term surface generated acoustic waves, which can be Lamb waves, pseudo/leaky acoustic waves (PSAW/LSAW) and pure SAW [15]. In this review, the term surface acoustic waves or SAWs will be used, which include Lamb waves and PSAW as well.

The benefit of using SAW sensors over BAWs is that the energy of the wave is confined to the surface of the material, making it more significantly more sensitive when using it for gravimetric sensing.

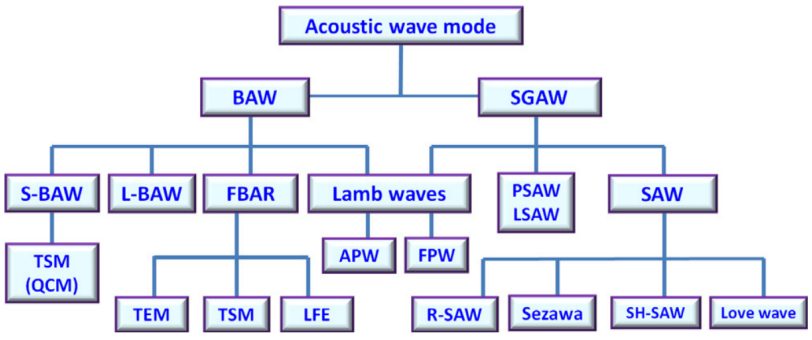

Figure 3.1: Classification of the different wave modes. Figure taken from [15]

SAW devices in general consist of a substrate, interdigital transducers (IDT) for transmitting and receiving the waves and a delay path interfering with the wave (see figure 3.2) [1, 16]. The design of the IDTs create the SAWs where the acoustic energy is strongly confined to the substrate surface.

This makes the wave very sensitive for any changes at the surface like mass loading, viscosity, conductivity, humidity, temperature, and more [1].

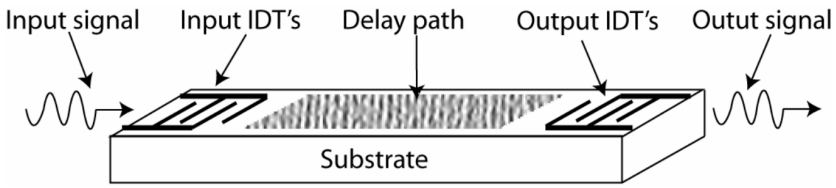

Figure 3.2: Basic design of a SAW device. Picture taken from [16]

3.1.1. sensing change in mass by change in frequency

In general, SAW sensors are very sensitive device which are potentially able to sense a whole range of parameter since they are sensitive to mechanical, chemical, optical or electrical changes on the surface [17, 18]. Acoustic waves have been used for measuring changes in temperature, moisture, strain, pressure, shock, acceleration, flow, viscosity, ionic contaminants, pH levels, electric, magnetic and radiation fields, gas and explosives [15]. More interesting for our application, is that it also has been used to detect biomolecules by binding with biomarkers for detection of for example early stage cancers [1].

Sensing properties All the different applications of SAW sensors measure, in the very essence, changes in propagation velocity of the wave coming from the emitting IDT. This change in velocity affects the frequency of the propagating wave which is measured by the receiving IDT, in accordance with $f_r = v/\lambda$ with f_r the resonant frequency, v the phase velocity and λ the wavelength. The changes in phase velocity can be attributed by [15]:

1. Intrinsic factors/material properties: density, elasticity, phase transformation, viscosity, conductivity, permittivity, changes in carrier concentration and mobility

2. Extrinsic factors: mass loading, temperature, deformation, humidity, pH values, ultraviolet and infra-red radiation, pressure, strain, stress, externally applied electric or magnetic fields and charge injection

The measured resulting change in frequency, as an effect of change in phase velocity, is expressed in the following equation:

$$\frac{\Delta f}{f_o} = \frac{\Delta v}{v_{acoustic}} \tag{3.1}$$

where Δv can be expressed as the sum of changes of phase velocity by each extrinsic factor listed above. For purely gravimetric changes, the frequency change can be expressed as [19]:

$$\Delta f = \frac{2\Delta m f_r^2}{A\sqrt{\rho\mu}} \tag{3.2}$$

Here, μ is the mass/area ratio, ρ the material density, and A the surface area. The sensitivity of the SAW sensor for any change in mass is dependent of the wave mode used, and therefore will be covered in the next section. However, from the equations above it can already be seen that the mass sensitivity is dependent on the resonant frequency and can be enhanced with increasing sensitivity

Electromechanical coupling coefficient An important parameter used to determine the efficiency of the SAW device, is the electromechanical coupling coefficient k^2, which gives the percentage of electrical energy that can be converted in acoustical energy and vice versa and is mainly dependent on the used material. k^2 is given by [15]:

$$k^2 = 2\frac{v_{free} - v_{metal}}{v_{free}} \tag{3.3}$$

where v_{free} and v_{metal} are the free surface and metalized surface phase velocities. The electromechanical coupling factor is largely dependent on material properties and careful selection of the substrate material can enhance the performance of the SAW sensor.

Quality factor The quality factor Q of the device is used to describe the performance of acoustic wave resonators, which is influenced by dielectric losses, ohmic losses, finite lateral size of the resonator, acoustic leakage, surface and interface roughness, and internal friction. More specifically, the quality factor is determined by the ratio between the energy stored and the energy dissipated [20]:

$$Q = \frac{2\pi f_0}{\alpha} = f_0 \frac{\rho_m}{2\pi k^2 \eta} \tag{3.4}$$

Where α is the attenuation coefficient, ρ_m is the material density and η the materials viscosity. The quality factor can also be experimentally determined by [15]:

$$Q = \frac{f_0}{\Delta f_{3dB}} \tag{3.5}$$

Where Δf_{3dB} is the bandwidth at -3dB of the resonance peak of the admittance of f_0

Temperature coefficient of frequency and delay As stated before, temperature can have a significant effect on sensing properties of SAW sensors. Due to increasing temperature, materials can expand and the increased stress which effects the frequency of the wave propagating through the material. This effect is represented by the temperature coefficient of frequency (TCF) and is desired to be as low as possible, to limit sensitivity to temperature. TCF can be theoretically calculated, but is usually experimentally measured by recording changes of frequency as a function of temperature [15]

3.2. Wave modes

When it comes to SAW devices for gravimetric sensors, there are four wave modes that are most often used: Rayleigh waves, Lamb waves, Shear horizontal SAWs and love waves. This section will introduce each of these wave modes and argue the one that will be most beneficial for the use of our purposes.

3.2.1. Rayleigh waves

When considering SAWs for sensing application, usually Rayleigh mode waves are used. Rayleigh waves travel near the surface of solids and have components both longitudinal and perpendicular to the direction it advances, making the waves somewhat elliptical in shape. It has the benefit that consumes little power, is easy to produce and relatively cheap [15]. They are generally more sensitive than other SAW wave modes and are great in gas sensing but not suitable for liquid sensing [21]. Due to the longitudinal component of the wave it excessively dissipates its energy into the liquid, causing it to lose its sensitivity in gravimetric sensing [15]. Because of this, not many SAW sensors use Rayleigh waves when it comes to liquid sensing. There are some studies that do use Rayleigh waves but it requires drying of the liquid on the substrate [21, 22].

The mass-sensitivity of Rayleigh mode SAW devices, is given by [23]:

$$\frac{\Delta f}{\Delta m} = \frac{k f_o^2}{A} \tag{3.6}$$

Where k is a constant of the sensing system Δm is the mass loading and A the area.

Tuning of the waves resonant frequency f_0, is quite easy and results within the range between a few MHz to GHz. By varying the wave velocity and the distance between the IDT digits, the resonant can be tuned [15]:

$$f_0 = \frac{v}{4d} \tag{3.7}$$

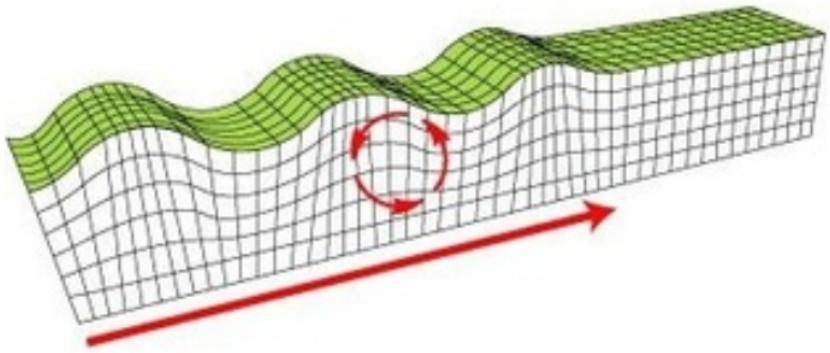

Figure 3.3: Rayleigh wave propagation. Figure taken from [24]

3.2.2. Lamb waves

Lamb waves are pretty similar to Rayleigh waves with components in both longitudinal and perpendicular to the direction of travel. In fact, they can be seen as two Rayleigh waves propagating on each side of the substrate [25].Lamb waves are generated in substrates with thickness less than one wavelength, the penetration depth of a Rayleigh wave. Technically, a Lamb wave can also be considered as a BAW since the substrate is so thin that the wave travels through the whole substrate, for simplicity reasons the Lamb wave will be considered as a SAW throughout this report.

Lamb waves generally have two modes when used in low frequencies [26]. The zero-order antisymmetric mode (A_0), also called Flexural Plate Waves (FPW). This mode has the benefit over Rayleigh waves that its phase velocity is smaller in a liquid medium compared to a solid, confining the wave on the surface.

The second Lamb wave mode is the zero-order symmetric mode (S_0). When the thickness of the substrate approaches zero, the S_0 wave will become purely longitudinal. This causes the energy dissipation into the liquid to be very small which makes S_0 Lamb waves a good candidate for gravimetric liquid sensing [27, 28]. The sensitivity of a Lamb wave device has been investigated by Duhamel, et al. and is given by [29]:

$$S_m = \frac{1}{2(d_C \rho_L + h\rho_m)} \tag{3.8}$$

Where d_C is the characteristic penetration thickness of the membrane and ρ_L and ρ_m is the density of the liquid and the substrate material respectively. In the same paper, Duhamel, et al. also describe d_C as:

$$d_C = \frac{\lambda}{2\pi} \frac{1}{\sqrt{1-(\frac{c_a}{c_L})^2}} \tag{3.9}$$

Where λ is the wavelength, c_a the phase velocity of the wave with the membrane in contact with air and c_L the phase velocity of the wave with the membrane in contact with the liquid.

Unlike Rayleigh waves, tuning the resonance frequency of Lamb waves is difficult. For A_0 mode, f_0 is given by [15]:

$$f_{A_0} = \frac{2\pi h}{\lambda^2} \sqrt{\frac{E}{12(1-\nu^2)\rho}} \frac{1}{\sqrt{\frac{\pi^2 h^2}{3\lambda^2}+1}} \tag{3.10}$$

and for S_0 mode:

$$f_{S_0} = \frac{1}{\lambda} \sqrt{\frac{E}{(1-\nu^2)\rho}} \tag{3.11}$$

Effectively, resonant frequencies of Lamb waves are generally quite low which range from kHz to lower MHz [15].

A downside of the use of Lamb waves is that the substrate needs to be very thin, causing it have a fragile structure. Furthermore, if parameters are not adequately tuned during its design and production it could have radiation loss into the liquid, which might prove to be difficult [15].

Although Lamb wave biosensors have been extensively studied in the 1990s, more recent research show much less report. This is due to the fact that they have a low operation frequency which limits its sensitivity and have fragile structures as mentioned before.

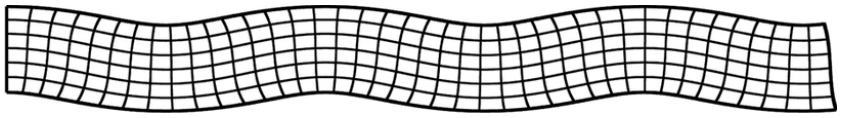

(a) A0 mode Lamb wave

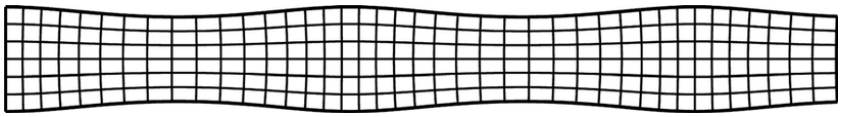

(b) S0 mode Lamb wave

Figure 3.4: Lamb wave propagation. Figures taken from [30]

3.2.3. Shear Horizontal Surface Acoustic Waves

Shear Horizontal Surface Acoustic Waves (SH-SAW) has transversal wave components and not perpendicular causing it to lose little energy into liquids. [15, 31]. Although most of the wave energy is distributed at the surface, a considerable amount is dissipated through the bulk as well, serving as a wave guide. This effect can be reduced by making the substrate thinner, but like the Lamb wave, this will make the structure more fragile. It is also important to note that the waves are confined by both the top and bottom surface of the substrate which means that both sides can be used for gravimetric sensing. This allows for backside sensing as well, allowing the front to be protected from the liquid [25].

In terms of the sensitivity the SH-SAW is similar to Rayleigh, having the same equation [15]:

$$\frac{\Delta f}{\Delta m} = \frac{k f_o^2}{A} \tag{3.12}$$

Also tuning the resonant frequency is given by the same equation as with the Rayleigh waves:

$$f_0 = \frac{v}{4d} \tag{3.13}$$

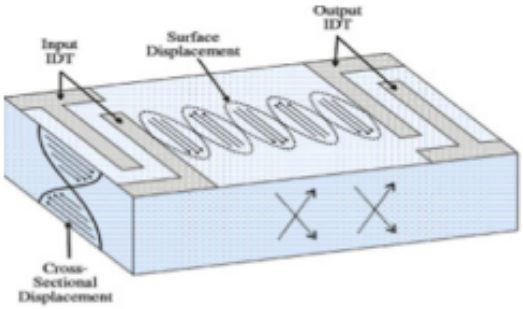

Figure 3.5: Shear horizontal surface acoustic wave propagation. Figure taken from [15]

3.2.4. Love waves

Love waves have attracted a lot of attention when it comes to (bio)chemical sensing in gasses and liquids in the last couple of decades. Love waves are made by creating a SH-SAW in the piezoelectric substrate and adding a dielectric guiding layer with a lower phase velocity on top of the substrate [32] . The difference in phase velocities causes the wave to be confined within the guiding layer causing the amplitude of the waves to decrease exponentially in thickness. This results in the highest mass sensitivity among SAW sensors [15]. Designing such a sensor require careful consideration of the guiding layer thickness, since insertion loss decreases quickly with increasing thickness. Just like SH-SAWs, there is no wave component normal to the surface resulting in no elastic interaction with the fluid allowing for the much higher sensitivity. There is, however, still some interaction with the fluid due to viscous liquid loading that causes small frequency shifts and increases insertion loss, which should be taken into account [33].

The sensitivity of Love wave sensors is represented by the following equation [34]:

$$S_m = \frac{1}{v}\frac{v' - v}{\sigma} = \frac{2\pi}{\lambda}\frac{1}{v}\frac{v' - v}{k\sigma} \tag{3.14}$$

Here

Just like with the SH-SAW and Rayleigh wave, the resonant frequency is given by the equation [15]:

$$f_0 = \frac{v}{4d} \tag{3.15}$$

3.2.5. Choosing the wave mode

Four wave modes have been studies: Rayleigh waves, Lamb waves, SH-SAWs and Love waves. Results show that Rayleigh waves are not suitable for gravimetric sensing in fluids and will therefore not be further considered as a viable option. Lamb waves have been used a lot in the 1990s for gravimetric sensing but lately other wave modes are more common due to its low operation frequency,

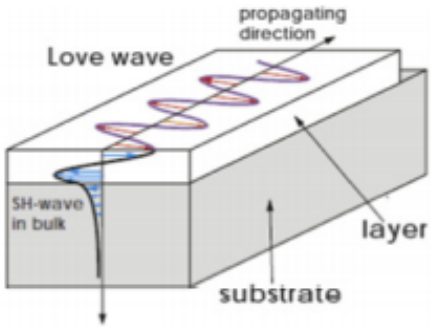

Figure 3.6: Love wave propagation. Figure taken from [15]

which limits sensitivity. SH-SAW wave modes are similar to Rayleigh waves, but with the benefit that it has a low energy dissipation into liquids. On top of that is it easy to produce and have a good sensitivity. Love waves can be seen as an enhanced version of SH-SAW waves where a waveguide on top of the substrate increases sensitivity. For this reason, Love waves will be used for the design of the sensor.

3.3. Materials

3.3.1. substrate

Since the choice for the Love wave requires the need of a 'shielding' waveguide, the substrate itself has some more freedom for the choice of the material. Indeed, when using SH-SAW devices Silicon dioxide is not a viable option for liquid sensing since the big mismatch with the dielectric constant with water, while for Love waves this is less of an concern.

The first and foremost property that the substrate material should have is that it is piezoelectric, such that piezoelectric waves can be excited. Other important parameters are a good electromechanical coefficient (K^2) for a low loss and more sensitive device, a low (TCF) to minimize sensitivity to temperature and the ability to make a purely shear polarized wave for better performance in liquid environments. Common materials used for SAW device substrates are AT- and ST-cut quartz (SiO_2), 36°y-x cut lithium tantalate ($LiTaO_3$), 41 or 128°y-x cut lithium niobate ($LiNbO_3$) [9, 34].

Lithium Niobate Lithium niobate is oftentimes used in combination with ZnO or SiO_2 as a guiding layer. Its very high electromechanical coupling factor with K^2 = 16% [35], makes using a design with this material very attractive since less attention needs to be given to limiting excessive wave damping, as is often the case with other materials. On top of that it also has a high shear wave velocity of 4800 m s^{-1}.However, using this material for the substrate will make the structure less strong since the lithium niobate is a brittle material. On top of that, the device will be very sensitive to temperature since it has a high TCF between 70 and 95 ppm/K [13], although it is possible to compensate for this using an guiding layer material with an opposite sign TCF[36].

Lithium Tantalate Lithium tantalate has a lower TCF, which is between 18 and 32ppm/K [13] . However, just like lithium niobate, lithium tantalate has a very brittle structure which makes production more difficult. Other parameters of litium tantalate are reasonably good. The electromechanical coupling coefficient of lithium tantalate is reasonably high (5% [35] and it has a high shear wave velocity of 4200 m s^{-1}

Quartz From the given parameters, quartz is very suitable to be used as substrate material. First of all, it is the only piezoelectric material that is able to create pure shear polarized waves [37, 38], given the right cut (ST). It also has good temperature characteristics, AT-cut quartz has zero TCF while ST-cut quartz has a TCF of 40 ppm/K which is very low compared to the other discussed materials. [36, 37]. Quartz also has a high shear wave velocity (5050 $\mathrm{m\,s^{-1}}$ for ST-cut, 5099 $\mathrm{m\,s^{-1}}$ for AT-cut) which allows for efficient capturing of the Love wave and low density (2650 $\mathrm{kg\,m^{-3}}$)However, compared to other materials, quartz has quite a low K^2 of 0.2% for ST-cut and 1.4% for AT-cut quartz.

Discussion In this subsection, three of the most commonly used substrate materials are discussed. The use of a waveguide placed on top of the substrate to create a Love wave, allows for less restrictions when choosing the material. For our applications, all three of the materials can be used while still keeping good results and it really depends on which design parameters are deemed more important: electromechanical coupling factor for high sensitivity and efficiency, low TCF to avoid cross-sensitivity, high shear wave velocity for more flexible choice for the waveguide or a material with the purest shear wave for the best performance in liquid environments. Some other considerations that are important to take into account are the structural strength of the material and the difficulty to produce.

Shear wave velocities of all three materials are high and can be used with a wide range of different waveguide materials to produce Love waves, as will be discussed in the next section. The highest electromechanical coupling factor is that of lithium niobate by a large margin, while lithium tantalate still has good performance on that area. However, despite that it has a much lower electromechanical coupling factor, quartz is the only material that is able to make pure shear horizontal wave and therefore also has a good efficiency and sensitivity for mass sensing in liquid media.

When it comes to temperature sensitivity, lithium niobate performs the worst with a high TCF. AT-cut quartz and lithium tantalate have quite similar TCF values and ST-cut quartz performs the best with 0 TCF. However, using ST-cut quartz requires a trade-off since this does not have the pure shear horizontal wave that AT-cut quartz has.

Structurally speaking quartz is the strongest material of them all since lithium tantalate and lithium niobate are relative brittle materials. Using a strong and sturdy material increases its longitivity and the long term stability of measurments. On top of that, quartz is a commonly used material in a lot of manufacturers and is cheap and easy to use.

In conclusion, all three materials are good and viable options to use. Based on our application for liquid sensing and limited resources when it comes to production, quartz seem to be the best option.

3.3.2. Waveguide

Designing a Love wave device requires a guiding layer to capture the generated wave. This confines the propagating wave to stay very close to the surface, effectively increasing the electromechanical coupling factor [35]. The capturing of the wave is achieved when the shear velocity of the guiding layer material is less than that of the substrate [39]. Therefore one of the most important parameters for choosing the waveguide material is the shear wave velocity. Other important parameters include a low material density to limit mass loading, high dielectric constant for liquid sensing efficiency and low acoustic absorption [40]. The latter is effected by the waveguide layer thickness, which also influences the way a Love waves behaves. Since choosing the right thickness is such an important

component of the SAW senor design, this section will first go more in depth on how to choose the waveguide layer thickness after which different commonly used materials are discussed.

Waveguide layer thickness Choosing the thickness of the waveguide is an important part of the SAW sensor design that needs careful consideration. For the conversion of a SH-SAW into a Love wave, the waveguide needs to be sufficiently thin such that as little energy as possible goes lost into the (may it be small) bulk of the waveguide. However, increasing the layer thickness also decreases the phase velocity throughout the material, increasing the energy capture in the guiding layer. Somewhere in between there is an ideal guiding layer thickness.

Gizeli, et. al have studied varying waveguide thicknesses for quartz and lithium tantalate substrates with a Novolac photoresist waveguide [32]. With this study, they evaluated the effect of different waveguide thicknesses on the change in frequency and amplitude of the wave. The results are shown in figures 3.7a and 3.7b. The x-axis represent the normalised thickness which is defined as the ratio of the waveguide thickness divided by the acoustic wavelength in the guiding layer (λ_{Nov}), of which the latter is related to the operating frequencies (104, 108 and 155 MHz) and the acoustic shear velocity (1100 m s^{-1}).

Figure 3.7a shows that for all three devices, using a thin waveguide will result in a velocity of the guided wave that is close to that of the substrate and which results in a small frequency change. Increasing the waveguide thickness, will decrease the velocity and thus a larger frequency drop. The larger frequency drop of quartz (Q155 and Q108 in the legend) compared to lithium tantalate (LT104) is explained by Gizeli, et. al to be due to the larger deference between the acoustic shear velocities of quartz and Novolac than lithium tantalate and Novolac.

Figure 3.7b shows that for quartz, increasing the frequency will increase the wave amplitude until a critical normalized thickness is used ($d/\lambda_{Nov} = 0.15$, d =1.5 µm for Q108 and $d/\lambda_{Nov} = 0.12$, d =0.9 µm for Q155). Below this critical frequency, more acoustic energy is trapped close to the upper surface of the device increasing the acoustic efficiency of the device. A thickness higher than the critical thickness decreases this effect and is explained by Gizeli, et. al to be because the Love wave is guided predominantly inside the Novolac, which is acoustically very lossy compared to piezoelectric materials like that of the substrate. Figure 3.7b shows a different result for the Lithium Tantalate substrate, which is relatively stable up until a normalized thickness around 0.14 (h = 1.5 µm). Gizeli, et al. explain this to be because lithium tantalate has a large piezoelectric coefficient which already guides the wave near the surface instead of diffracting into the bulk. With a normalized thickness of above 0.14 the wave resides mainly in the Novolac layer and experience the same lossy behaviour as with the quartz substrate.

Gizeli, et al. concluded from these results that the critical normalized thickness is an important characteristic of the waveguide material that is independent of the operating frequency or piezoelectric substrate. While desiging the waveguide, it is important to maintain its thcikness below this value. They also concluded that the maximum mass sensitivity would occur for a waveguide thickness which is equal to $h = \lambda_{Nov}/4$.

An ideal waveguide has next to a lower shear wave velocity than the substrate and low acoustic absorption, also high elastic properties, low density, is compatible to the aqueous environment and a uniform surface profile [41]. Another important material property that needs to be taken into account when it comes to liquid sensing, is the dielectric constant. A high dielectric constant helps to confine electric fields generated by the IDTs to the material, even when it is in contact with water

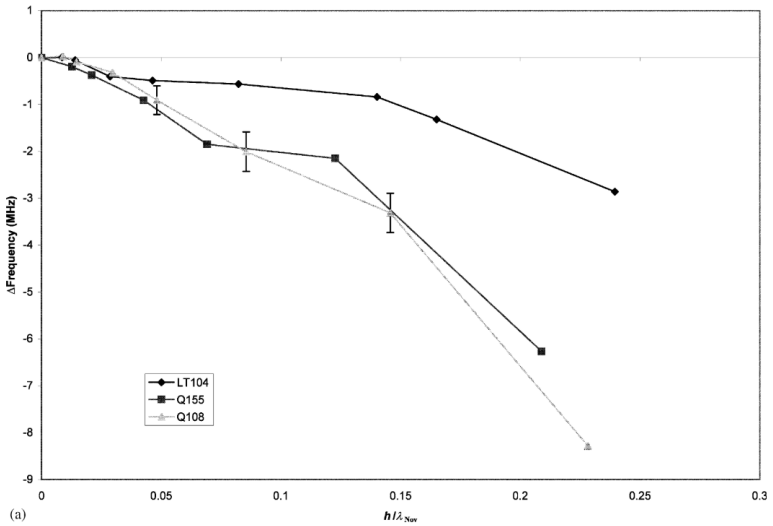

(a) Dependency of wave frequency on normalized waveguide thickness. Figure taken from [32]

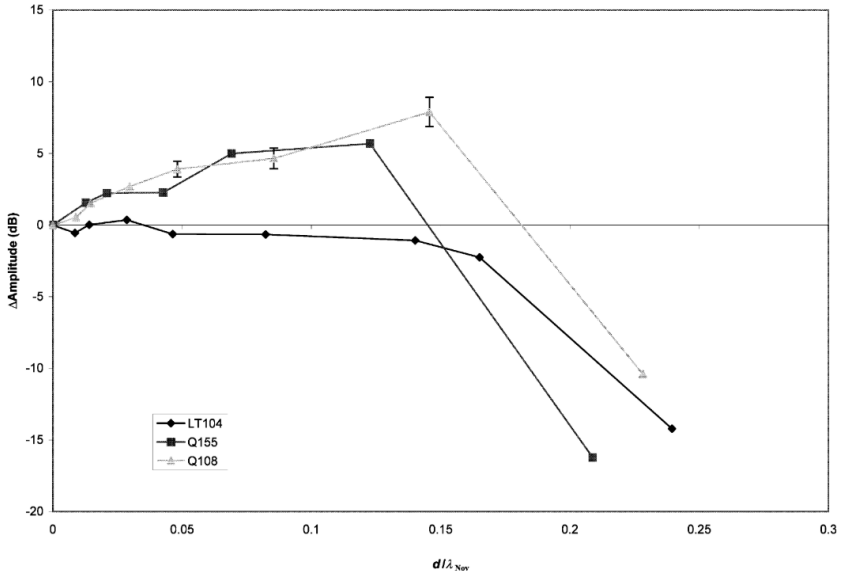

(b) Dependency of wave amplitude on normalized waveguide thickness. Figure taken from [32]

which has a dielectric constant of 75[39]. Materials that are often used as waveguide are polymers, silicon dioxide, zinc oxide and aluminum nitride [15, 35, 42].

Polymers Early Love SAW devices for biochemical sensing applications used mainly polymers as the waveguide material, since they generally have a low shear wave velocity and their high resistance to chemical agents. However, polymers also have high acoustic damping, decreasing the sensitivity [25].

Some often used polymers are PMMA and Novolac photoresist. PMMA has a low shear wave velocity 1100 $\mathrm{m\,s^{-1}}$) low density (1170 $\mathrm{kg\,m^{-3}}$), good elastic properties. and the benefit of protecting the interdigital electrodes[43]. The low shear wave density allows it to make Love waves with a large number of substrate materials. Indeed, all three of the substrate materials listed before can be used in combination with PMMA concerning shear wave velocities.

Rasmussen, et. al compared PMMA to Novolac as a waveguide on a quartz substrate[44]. The frequency response for different polymer thicknesses showed that the velocity of the Love waves are very much alike, indicating similar mechanical properties. No significant difference could be detected on the mass-sensitivities between the two materials. However, the same study showed that devices with a Novolac waveguide have a much better chemical and long-term stability when in contact with a liquid sample.

Silicon dioxide Silicon dioxide is an often used option when it comes to guiding layer material. It has adequately low shear wave velocity, has a good chemical and mechanical resistance and is cheap and easy to produce. However, silicon dioxide has a low dielectric constant ($\epsilon = 3.9$), causing it to lose the energy of created electric fields to its surroundings when used in water.

Zinc oxide ZnO has several of advantages over other materials. It has a decent dielectric constant of 10.4 and alow shear wave velocity (2650 $\mathrm{m\,s^{-1}}$), making it suitable to use as a waveguide on lithium niobate, lithium tantalate and quartz. The reason why a lot of studies use other guiding layer materials is that it is a CMOS contaminant which makes safe production while using ZnO much more difficult [45]. Furthermore, it is very reactive when exposed to liquids making it not suitable for sensing in urine. Some studies use backside sensing, where the guiding layer is not in contact with the liquid but this requires SH-SAW sensing rather than Love wave sensing [25].

Aluminum nitride For that reason, ZnO is often compared to aluminum nitride (AlN) to be used as the material for the guiding layer and it offers a lot of benefits, apart from CMOS compatibility. It has a high phase velocity (11 000 $\mathrm{m\,s^{-1}}$) which increases mass sensitivity and better dielectric properties compared to ZnO [46]. However, creating a good Love wave in will prove to be difficult using aluminum nitride since it has a very high shear wave velocity of 6450 $\mathrm{m\,s^{-1}}$ [42].

It is also possible to add a second guiding layer on top of the first one. Li et al. [47] have tried this by adding a thin gold layer on top of a silicon dioxide waveguide. This decreased the love wave shear velocity significantly and they reported a 72 times more sensitive device compared to the same structure without the gold layer. As an added benefit, gold is an excellent adhesive for protein binding [32].

Discussion This subsection covered the waveguide of a SAW sensor needed for the generation of a Love wave from a SH-SAW. Several materials have been discussed and for different applications there are different materials to choose from. Some materials that are not usable for our application are silicon dioxide and aluminum nitride. Silicon dioxide has a lower dielectric constant than water, causing loss of a large portion of the wave energy into liquids. This will greatly affect the mass sensitivity and renders the device useless for liquid sensing applications. Aluminum nitride has a high number of beneficial properties but it has the large disadvantage of a high shear wave velocity. It is much higher than any of the substrate materials discussed in the previous section and will therefore be unable to create a Love wave.

Zinc oxide is in theory an excellent material to use as a waveguide. It has a low shear wave velocity that is compatible with all three of the potential substrate materials discussed in the previous section and has a good dielectric constant which makes it suitable for liquid sensing. It does however have some practical disadvantages like being a CMOS contaminant and it being reactive to water which reduces its longevity. It is a less than ideal material to produce and use and choosing this as a waveguide material need proper and clean production techniques.

This leaves polymers like PMMA an Novolac as the best and safest options based on this literature reviews for the use as waveguide material. They have a very low shear wave velocity making it compatible with all three of the substrate materials discussed in the previous section.

3.4. IDT design

For creating a surface acoustic wave, careful interdigital transducer design is detrimental. The IDTs have the important task to either transmit or receive the surface acoustic wave. This section will first go a into basic IDT design for general properties, followed by a description of electrical properties of the IDTs. Finally different design configuration will be discussed.

3.4.1. basic IDT configuration

A basic IDT consists of interlocking electrode finger pairs sandwiched into a piezoelectric substrate, as depicted in figure 3.8a. By applying an AC voltage, the substrate will, as a result of the piezoelectric effect, produce the desired SAW propagating in the direction perpendicular to both the direction of the fingers and substrate surface. The interdigital space, the distance between consecutive fingers of the electrodes, corresponds to the wavelength of the transmitted wave. A typical IDT electrode spacing is an integer multiple, or 1/2, 1/3, or 1/4 of the wavelength $\lambda = 2\pi/k$, where k is the wavenumber [9]. This wavelength will determine the resulting resonating frequency of the wave, together with the phase velocity of the wave in the respective materials. At the other end of the guiding layer of the device, the receiving IDT will measure this wave as an oscillating electric potential over its fingers, also by the piezoelectric effect.

(a) Basic (Standard bidirectional)IDT design [15]

(b) Split finger IDT design [15]

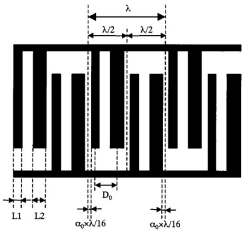

(c) Single Phase Unidirectional Transducer (SPUDT) design [15]

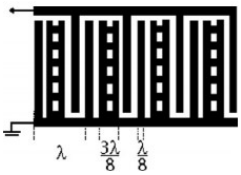

(d) Distributed acoustic reflecting transducer (DART) design [15]

Figure 3.8

The frequency response of a typical IDT design looks similar to figure 3.9. The bandwith of the signal becomes more narrow with increasing numbers of finger pairs in the IDT, enhancing the quality factor Q of the device as shown in equation 3.5. However, it must be taken into consideration that increasing the number of finger pairs, also increases the mass loading, dampening the wave and thus decreases sensitivity [35].

3.4.2. IDT electrical properties

The input IDTs admittance ($Y_a = G_a + jB_a$) describe the effect of the acoustically induced charges on the transducers as a result of the piezoelectric properties of the substrate material and can be

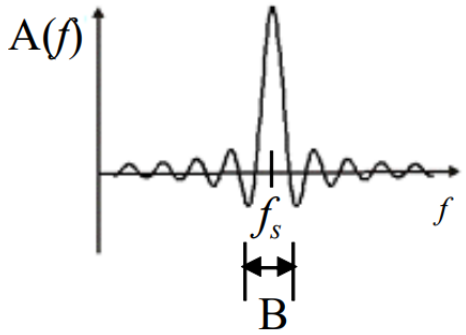

Figure 3.9: typical frequency response of an IDT. Picture taken from [35]

characterized by an equivalent circuit as shown in figure 3.10 [48]. The static capacitance between the fingers is represented by C_t, typically the dominating imaginary part. G_a represents the power that goes into the surface wave, and for good efficiency needs to be as high as possible. The materials internal resistance are represented by R_s and take into account the ohmic losses within the IDT structure. When subjected to a liquid an additional conductance G_t can be added which is ideally as little as possible. This can be done by shielding the IDT structure from the liquid, although this will reduce the efficency in electro-acoustic power conversion as the shielding generally increases insertion loss. Additionally, liquid loading will increase C_t and decrease G_a but this time shielding will not limit this effect [48].

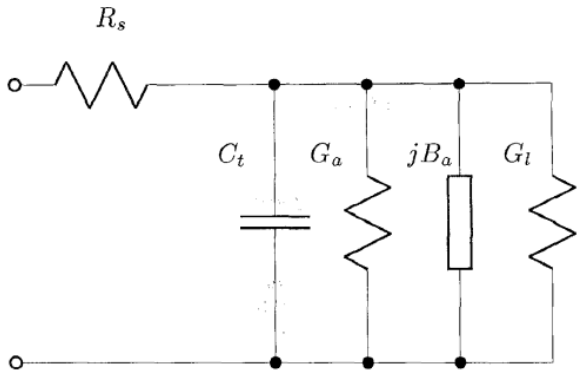

Figure 3.10: Equivalent circuit for the IDT admittance. Figure taken from [48]

3.4.3. different IDT configurations

A major problem with basic IDT design, is that it transmits waves in both directions. Considering its application in a SAW device, this results in a 3 dB loss of energy since it only needs to go into one direction [49].

One way this can be solved is by using reflectors. These are structures placed in the same configuration with equal interdigital space as IDTs behind the transmitting and/or receiving transducers. Usually the reflector IDTs also have less finger pairs than the transmitting and receiving IDTs. Including the reflectors into the device design will allow for a very narrow low-loss pass band, but will also increase the design difficulty significantly [35]. There are also different IDT configurations designed to enhance the performance and directionality [15, 16, 50]. Common alternative designs include split IDTs (figure 3.8b). The configuration of the fingers increase directionality slightly since they reflect back some of the waves, but are much less effective then using reflectors.

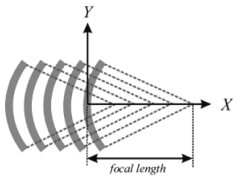

(a) Circular arc IDT design. Picture taken from [55]

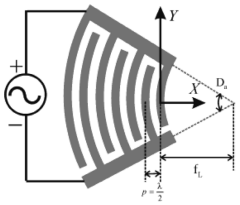

(b) Concentric IDT design. Picture taken from [55]

Figure 3.11

More effective is the Single Phase Unidirectional Transducer (figure 3.8c), first designed by Nakamura et al. (2001)[51] The difference in finger width increase the reflectively of the IDTs and increase the directionality, making the IDT much more efficient. However, the finger width need to be carefully manufactured, as they found the optimal width of the fingers to be $\lambda/4$ for the thick fingers and $\lambda/8$ for the thin fingers, with a combined four fingers per wavelength. Several studies have followed up with a study to redesign the original SPUDT, some of which with success [52, 53].

Another IDT designed to include reflectivity for uni-directionality is the Distributed Acoustic Reflecting Transducer (DART design). Reflective elements are distributed over the entire IDT in both the propagation and normal direction [54] Segmentation of within the transducers allow for control over the reflectivity of the transducer, achieving more design flexibility [15]

3.4.4. Focused IDT configuration

Focused IDTs (FIDTs) were first described by Kharusi and Farnell in 1972 [56]. The circular shape of the IDTs allows for focusing of the wave into a smaller surface area, increasing the wave's intensity. Focusing of the SAWs is made possible by superposition of SAW modes with different propagation angles [57]. In order to focus a beam at a single point O, IDTs need a shape that coincides with concentric wavepoints with O as the centre.

When talking about FIDT, there is a distinguishment between circular-arc shape and a concentric shape (see figure 3.11a and 3.11b). Circular arc IDTs create SAWs into a narrow and long beam, rather than a into single focal point like concentric IDTs

For designing a circular arc IDT, Wu et al. [55] showed that important parameters to take into account are the degree of the arcs and the geometric focal length and number of finger pairs in the IDT. Increasing the degree of arc, will increase the compression of the beam into a small line but will have no significant effect on the amplitude. When the degree of arc is too small, however, will cause the amplitude field to have no obvious peak.If the geometric focal length is too small, will make the amplitude field become unstable. When the geometric focal length is increased to the point of stability, increasing it more will have no significant effect.They have also showed, that the number of finger pairs are not really important in terms of focusing properties, but more finger pairs will increase the amplitude of the wave. Wu et al. showed similar results for the concentric IDTs.

In a different study, de Lima, et. al experimentally evaluated focused concentric FIDTs on a GaAs substrate [57]. From this study, it is important to note that the conversion efficiency between electrical and acoustic power of FIDTs is less than that of linear IDTs since their design is not optimized to improve rf coupling. Still, they showed superior capabilities of FIDTs compared to linear IDTs by measuring much larger SAW amplitudes despite of the less efficient power conversion.

De Lima, et. al also compared in the same study the focusing efficiency of double finger IDTs and single finger IDTs. The best performance was measured for the double finger IDTs due to better reflection properties [57].

3.4.5. Discussion

Different interdigital transducer designs have been discussed in this section. For the good power efficiency and high sensitivity it is to have increased directivity. This can be done by several parralel IDT configurations like the split finger, SPUDT and DART design but the most efficient way is to use a focused IDT configuration. The circular shape of the IDTs will create either a focal point or a focused beam (for a concentric or circular arc IDT, respectively) and allows for more wave energy to go into a more confined area. Different design considerations for IDTs are discussed like the number of finger pairs, degree of arc and geometric focal length but it is difficult to determine what values should be used since this depends on the geometry of the device.

3.5. Conclusion

In this chapter, the different design considerations relating to a SAW biosensor that is suitable for liquids have been discussed. First it was explained how SAW devices operate parameters were established that describe the performance of the device. The most important ones are using materials with a high electromechanical coupling coefficient, obtaining high quality factor by having a narrow bandwidth and a material with high attenuation coefficient and choosing materials with a low TCF. Furthermore, when sensing in liquid, performance is improved when using a waveguide material that has a dielectric constant close to that of water ($\epsilon = 80$).

Different wave modes that were considered to use for the SAW device were Rayleigh, Lamb, SH-SAW and Love waves. Love waves showed the best properties for our application because of the suitability for sensing in fluid, strong structure and high sensitivity.

Next, the materials for the substrate and waveguide layer were discussed. Suitable materials for the substrate are lithium niobate, lithium tantalate and quartz. All three materials will be suitable for our purposes and will have good performance, although quartz showed to be the best option. The waveguide layer can consist of polymers like PMMA and Novolac, silicon dioxide, aluminum nitride or zinc oxide. Silicon dioxide loses too much power into the liquid reducing sensitivity and aluminum nitride had too high of a shear wave velocity rendering both unsuitable for our purposes. Although zinc oxide is able to create good Love mode waves, it is highly reactive to water and is a CMOS contaminant. The resulting decrease in longevity and more complex fabricating makes zinc oxide a less then ideal material to use. Polymers like PMMA and especially Novolac showed to have the best characteristics and will perform good on the conversion of SH-SAW waves into Love waves for liquid biosensing purposes.

Finally, different IDT designs were discussed that are used to transmit and receive the surface acoustic waves. The highest efficiency and mass-sensitivity can be reached using focused IDTs. This can be either a circular arc IDT or a concentric IDT. The best choice will depend on the geometry of the SAW device.

4

Urinary Biomarkers for Prostate Cancer

The selection process of the systematic review can be viewed in figure 4.1. In total 45 papers have been selected for detailed analysis. From these, 17 papers were deemed fit to use for the review. Five papers have been selected on PSA, 7 papers on EN-2 and 5 papers on TMPRSS2:ERG. Since there were no papers found on the sensitivity and specificity of detecting PSA in urine, the selection criteria for this biomarker is broadened to include detection in serum as well. This section will first go more in depth about the biomarkers itself, followed by the results of the systematic review on the sensitivity and specificity.

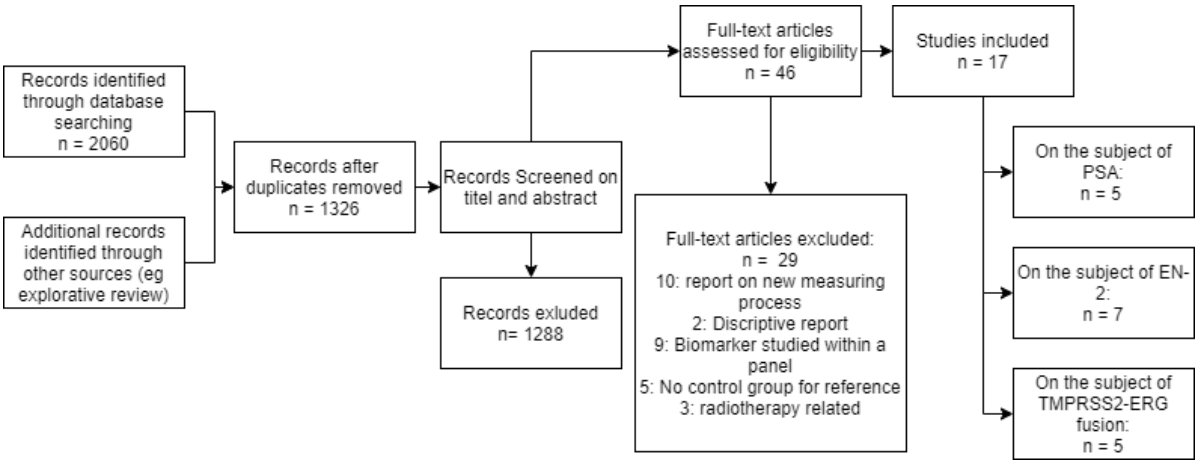

Figure 4.1: Selection process of the systematic research

4.1. Prostate Specific Antigen

One of the most well-known and researched biomarkers for the detection of PCa, is Prostate Specific Antigen (PSA). It was fist discovered in 1970 by R.J. Ablin, et al. [58] and was the first FDA approved biomarker for early detection of PCa. Later on, it also started regulated screening. This was a big step in the diagnosis of prostate cancer and the proportion of patients having advanced disease at diagnosis was decreased by 80%, while the PCa mortality rate was decreased by over 42%. [59].

However, PSA screening is also subject to a lot of critique [60]. Although it is true that prostate cancer prevalence has increased, it has also caused overtreatment in patient with low-risk PCa patients because it is not effectively able to distinguish between prostate cancer and benign prostate-hyperplasia which also increases PSA levels [5, 6]. Since PSA is known not to be very specific (which

will be covered more in detail below), a positive PSA test will result in further testing of the patient. Oftentimes this will be done by prostate biopsy, which is invasive and is not only uncomfortable to the patient, but can also lead to bleeding and infections [8]. There are some PSA-derivative tests available, but are subject to the same limitations of PSA itself: increased prostate volume will also elevate the levels.

This asks for a trade off when choosing the cut-off value between having either a high sensitivity and low specificity or vice versa. Usually, a cut-off value of 4.0 ng/mL or higher is used for screening purposes.

Results of the systematic review concerning PSA can be viewed in table 4.1. Although most studies show a good sensitivity, the specificity is low in nearly every study. One outlier is shown by Salami, et al. which can be attributed to the fact that they have used a significantly higher cutoff concentration in order to increase specificity at the cost of sensitivity.

It is noteworthy that in the last ten years, not much research has been done on the sensitivity and specificity of PSA as a biomarker for Prostate Cancer, only four researches have been found in this systematic review. However, these studies are in line what have been the established sensitivity and specificity of earlier research as is shown in a different literature review conducted by Harvey, et. al [61]. They conducted a systematic review on literature on PSA accuracy between and 2008. They found that sensitivities ranged from 79-100% and specificities from 6-66%. This review shows that the sensitivity and specificity, depending on the cutoff concentration and detection method, for most studies is between 70.8-92.3% and a specificity between 14.2-27.3%.

Table 4.1: Listed results of independent papers on the sensitivity and the specificity of PSA as a biomarker for prostate cancer

Source	**Sensitivity**	**Specificity**	**Cutoff**	**Detection Method**
B. Donald-Buri (2016) [62]	92.3%	26.9%	4.0 ng/mL	Not mentioned
F. Coelho (2015) [63]	70.8%	27.3%	5.56 ng/mL	Real-Time PCR
C. Chang (2015) [64]	Not mentioned	19.1%	2.0 ng/mL	immunoassay analyzer
S. Agnihotri (2014) [65]	97%	14.2%	5.0 ng/mL	ELISA
S.S. Salami (2013) [66]	40%	93%	10.0 ng/mL	Real-Time PCR

4.2. Engrailed-2

En-2 is a homeodomain-containing transcription factor involved in the progression of PCa [67]. Normally it is involved in early embryonic development but it is re-expressed in prostate cancer [68]

Results of the systematic review related to urinary Engrailed-2 as a biomarker for Prostate Cancer are shown in table 4.2. It is apparent that there is no good consensus between researches on the effectivity of using urinary EN-2 as a biomarker for PCa based on these results. Two of the three

most recent studies have not reported any significance with control, one of which did not report the detection method used to evaluate EN-2 levels.

An explanation for this, is evident from the research of Marszall, et al. He compared urinary EN-2 levels in patients with prostate cancer and benign prostate hyperplasia before and after a urinary prostate massage. They report no significant correlation between EN-2 levels and the Gleason score, which is a metric to describe the malignancy of a prostatic tumor. However, when urine samples were collected after a prostatic massage, EN-2 levels were highly elevated and a clear significant distinction could be made between patient with PCa and BPH [69]. Indeed, the studies done by do Carmo Silva, et al. and Donald-Buri, et al. have done no prostatic massage before collecting urine samples [62, 70].

The cut-off concentration of urinary EN-2 values in Marszall's study is much lower than other studies used. Besides using the manufacturers' specified cut-off point, no further explanation is found what could cause this large difference. Most likely it is due to different methodology used by the manufacturers' ELISA kits.

Table 4.2: Listed results of independent papers on the sensitivity and the specificity of Engrailed-2 as a biomarker for prostate cancer

Source	**Sensitivity**	**Specificity**	**Cut-off value**	**Detection Method**
J.D. do Carmo Silva (2019) [70]	No significant difference with control			ELISA
E. Gómez-Gómez (2019) [71]	Only report significant elevation of EN-2 levels			ELISA
B. Donald-Buri (2016) [62]	No significant difference with control			Not mentioned
M.P. Marszall (2016) [69]	79%	81%	0.31 ng/mL	ELISA
E. Killick (2013) [72]	66.7%	89.3%	42.5 ng/mL	ELISA
H. Pandha (2012) [73]	70%	No control	42.5 ng/mL	ELISA
R. Morgan (2011) [68]	66.2%	88.2%	42.5 ng/mL	semi-quantative RT-PCR and immuno-histochemistry

4.3. TMPRSS:ERG

Transmembraneprotease, serine 2 (TMPRSS): erythroblastosis virus E26 oncogene homolog (ERG) fusion has been known for several year to be a gene fusion that is highly specific to prostate cancer [74].

Based on the results of the systematic review in table 4.3, it can be seen that TMPRSS2:ERG has excellent specificity. Especially compared to PSA the number of false positives using this biomarker will be much lower. This is due to the fact that the gene fusion is not seen in any tissue other than

cancerous prostate tissue which also leads to the benefit that it does not require a cut-off concentration to indicate PCa [75]. However, not all prostate tumors have the tendency to invade the prostate ductal system, resulting in fewer cells in urine what explains the low sensitivity [76]. Similar results have been gathered by a literature review of Fujita, et. al, reporting a prevelance of TMPRSS2-ERG in 30-50% in patients with localized prostate cancer [77]. Therefore it will have to be used as a part of a panel with other biomarkers in order to produces effective results .

Table 4.3: Listed results of independent papers on the sensitivity and the specificity of urinary TMPRSS2:ERG fusion as a biomarker for prostate cancer

Source	**Sensitivity**	**Specificity**	**Detection Method**
N.B. Delongchamps (2015) [76]	39%	93%	RT-qPCR
P. Bories (2013) [78]	62%	93%	RT-PCR
S.S. Salami (2013) [79]	67%	87%	RT-PCR
R. Sabaliauskaite (2012) [80]	58%	81%	RT-PCR
Nguyen (2011) [81]	34.8%	100%	qPCR

A big disadvantage of TMPRSS2:ERG when it comes to detection by the means of a SAW device is the complexity of the pre-processing that is desired. In order to detect the presence of the TMPRSS2:ERG gene fusion transcription is required in multiple steps. Therefore it is not straightforward to use as in putting a urine sample on the substrate and waiting for it to attach to deposited antigens, as is the case with EN-2 and PSA. For example Sabaliauskaite, et al. took the urine samples and first had to extract total RNA, remove Genomic DNA, dissolve the RNA in RNase-free water before being able to revers transcribe it using RT-PCR [80].

4.4. Conclusion

Three biomarkers have been studied for their sensitivity and specificity: PSA, EN-2 and TMPRSS2:ERG fusion, of which the latter two purely for their presence in urine. Compared two each other, PSA has the lowest specificity resulting in a high number of false positives. TMPRSS2:ERG has the highest specificity but some papers report a low sensitivity. Furthermore, using TMPRSS2:ERG fusion as a urinary biomarker for our purposes needs transcription and is thus less suitable. EN-2 has both a high sensitivity and specificity, given that a prostate massage has been applied before urine sample collection. Therefore EN-2 shows to be the better option to choose when it comes to urinary biomarker detection of prostate cancer by the means of a SAW sensor

Bibliography

[1] K. Länge, B. E. Rapp, and M. Rapp, "Surface acoustic wave biosensors: A review," Analytical and Bioanalytical Chemistry, vol. 391, no. 5, pp. 1509–1519, 2008.

[2] GCO, "Estimated number of new cases in 2018, worldwide, males, ages 55+," 2018.

[3] KWF, "Prostaatkanker in cijfers," vol. 2008, p. 2020, 2015.

[4] Harvard Health Publishing, "The pros and cons of PSA screening," 2010.

[5] T. Pejcic, J. Hadzi-Djokic, M. Acimovic, C. Topuzovic, B. Milkovic, and A. Janjic, "Urinary prostate specific antigen: Is the clinical use likely?," Acta chirurgica Iugoslavica, vol. 52, no. 4, pp. 69–74, 2005.

[6] D. Wu, J. Ni, J. Beretov, P. Cozzi, M. Willcox, V. Wasinger, B. Walsh, P. Graham, and Y. Li, "Urinary biomarkers in prostate cancer detection and monitoring progression," Critical Reviews in Oncology/Hematology, vol. 118, no. May, pp. 15–26, 2017.

[7] M. R. Downes, J. C. Byrne, S. R. Pennington, M. J. Dunn, J. M. Fitzpatrick, and R. W. G. Watson, "Urinary markers for prostate cancer," BJU International, vol. 99, no. 2, pp. 263–268, 2007.

[8] F. M. Wagenlehner, E. Van Oostrum, P. Tenke, Z. Tandogdu, M. Çek, M. Grabe, B. Wullt, R. Pickard, K. G. Naber, A. Pilatz, W. Weidner, and T. E. Bjerklund-Johansen, "Infective complications after prostate biopsy: Outcome of the Global Prevalence Study of Infections in Urology (GPIU) 2010 and 2011, A prospective multinational multicentre prostate biopsy study," European Urology, vol. 63, no. 3, pp. 521–527, 2013.

[9] D. B. Go, M. Z. Atashbar, Z. Ramshani, and H. C. Chang, "Surface acoustic wave devices for chemical sensing and microfluidics: A review and perspective," Analytical Methods, vol. 9, no. 28, pp. 4112–4134, 2017.

[10] O. Onen, A. Sisman, N. D. Gallant, P. Kruk, and R. Guldiken, "A urinary Bcl-2 surface acoustic wave biosensor for early ovarian cancer detection," Sensors (Switzerland), vol. 12, no. 6, pp. 7423–7437, 2012.

[11] O. Tigli, L. Bivona, P. Berg, and M. E. Zaghloul, "Fabrication and characterization of a surface-acoustic-wave biosensor in cmos technology for cancer biomarker detection," IEEE Transactions on Biomedical Circuits and Systems, vol. 4, no. 1, pp. 62–73, 2010.

[12] F. Zhang, S. Li, K. Cao, P. Wang, Y. Su, X. Zhu, and Y. Wan, "A microfluidic love-wave biosensing device for PSA detection based on an aptamer beacon probe," Sensors (Switzerland), vol. 15, no. 6, pp. 13839–13850, 2015.

[13] B. Liu, X. Chen, H. Cai, M. A. Mohammad, X. Tian, L. Tao, Y. Yang, and T. Ren, "Surface acoustic wave devices for sensor applications," Journal of Semiconductors, vol. 37, no. 2, pp. 1–9, 2016.

[14] D. Moher, A. Liberati, J. Tetzlaff, D. G. Altman, D. Altman, G. Antes, D. Atkins, V. Barbour, N. Barrowman, J. A. Berlin, J. Clark, M. Clarke, D. Cook, R. D'Amico, J. J. Deeks, P. J. Devereaux, K. Dickersin, M. Egger, E. Ernst, P. C. Gøtzsche, J. Grimshaw, G. Guyatt, J. Higgins, J. P. Ioannidis, J. Kleijnen, T. Lang, N. Magrini, D. McNamee, L. Moja, C. Mulrow, M. Napoli, A. Oxman, B. Pham,

D. Rennie, M. Sampson, K. F. Schulz, P. G. Shekelle, D. Tovey, and P. Tugwell, "Preferred reporting items for systematic reviews and meta-analyses: The PRISMA statement," PLoS Medicine, vol. 6, no. 7, 2009.

[15] Y. Q. Fu, J. K. Luo, N. T. Nguyen, A. J. Walton, A. J. Flewitt, X. T. Zu, Y. Li, G. McHale, A. Matthews, E. Iborra, H. Du, and W. I. Milne, "Advances in piezoelectric thin films for acoustic biosensors, acoustofluidics and lab-on-chip applications," Progress in Materials Science, vol. 89, pp. 31–91, 2017.

[16] S. Cular, "Designs and applications of surface acoustic wave sensors for biological and chemical sensing and sample handling," , no. October, p. 269, 2008.

[17] L. A. Kuznetsova and W. T. Coakley, "Applications of ultrasound streaming and radiation force in biosensors," Biosensors and Bioelectronics, vol. 22, no. 8, pp. 1567–1577, 2007.

[18] J. W. Grate, S. J. Martin, and R. M. White, "Acoustic Wave Microsensors," Analytical Chemistry, vol. 65, no. 21, 1993.

[19] G. Sauerbrey, "Verwendung von Schwingquarzen zur Wägung dünner Schichten und zur Mikrowägung," Zeitschrift für Physik, vol. 155, no. 2, pp. 206–222, 1959.

[20] A. Arnau, Piezoelectric transducers and applications (Google eBook). 2008.

[21] M. Agostini, G. Greco, and M. Cecchini, "A Rayleigh surface acoustic wave (R-SAW) resonator biosensor based on positive and negative reflectors with sub-nanomolar limit of detection," Sensors and Actuators, B: Chemical, vol. 254, pp. 1–7, 2018.

[22] G. De Simoni, G. Signore, M. Agostini, F. Beltram, and V. Piazza, "A surface-acoustic-wave-based cantilever bio-sensor," Biosensors and Bioelectronics, vol. 68, pp. 570–576, 2015.

[23] D. A. Buttry and M. D. Ward, "Measurement of Interfaclal Processes at Electrode Surfaces with the Electrochemical Quartz Crystal Microbalance," Chemical Reviews, vol. 92, no. 6, pp. 1355–1379, 1992.

[24] Science Learning Hub, "Seismic waves," 2007.

[25] M. J. Vellekoop, "Acoustic wave sensors and their technology," Ultrasonics, vol. 36, no. 1-5, pp. 7–14, 1998.

[26] J. W. Grate, S. W. Wenzel, and R. M. White, "Flexural Plate Wave Devices for Chemical Analysis," Analytical Chemistry, vol. 63, no. 15, pp. 1552–1561, 1991.

[27] M. J. S. Lowe, R. E. Challis, and C. W. Chan, "The transmission of Lamb waves across adhesively bonded lap joints," The Journal of the Acoustical Society of America, vol. 107, no. 3, pp. 1333–1345, 2000.

[28] P. Muralt, N. Ledermann, J. Paborowski, A. Barzegar, S. Gentil, B. Belgacem, S. Petitgrand, A. Bosseboeuf, and N. Setter, "Piezoelectric micromachined ultrasonic transducers based on PZT thin films," IEEE Transactions on Ultrasonics, Ferroelectrics, and Frequency Control, vol. 52, no. 12, pp. 2276–2288, 2005.

[29] R. Duhamel, L. Robert, H. Jia, F. Li, F. Lardet-Vieudrin, J. F. Manceau, and F. Bastien, "Sensitivity of a Lamb wave sensor with 2 μm AlN membrane," Ultrasonics, vol. 44, no. SUPPL., 2006.

[30] C. Willberg, S. Duczek, J. M. Vivar-Perez, and Z. A. Ahmad, "Simulation methods for guided wave-based structural health monitoring: A review," Applied Mechanics Reviews, vol. 67, no. 1, 2015.

[31] N. Barié and M. Rapp, "Covalent bound sensing layers on surface acoustic wave (SAW) biosensors," Biosensors and Bioelectronics, vol. 16, no. 9-12, pp. 979–987, 2001.

[32] E. Gizeli, F. Bender, A. Rasmusson, K. Saha, F. Josse, and R. Cernosek, "Sensitivity of the acoustic waveguide biosensor to protein binding as a function of the waveguide properties," Biosensors and Bioelectronics, vol. 18, no. 11, pp. 1399–1406, 2003.

[33] G. Kovacs, M. J. Vellekoop, R. Haueis, G. W. Lubking, and A. Venema, "A love wave sensor for (bio)chemical sensing in liquids," Sensors and Actuators: A. Physical, vol. 43, no. 1-3, pp. 38–43, 1994.

[34] J. Liu and S. He, "Properties of Love waves in layered piezoelectric structures," International Journal of Solids and Structures, vol. 47, no. 2, pp. 169–174, 2010.

[35] M. I. Gaso Rocha, Y. Jimenez, F. A., and A. Arnau, "Love Wave Biosensors: A Review," State of the Art in Biosensors - General Aspects, 2013.

[36] B. Jakoby and M. J. Vollekoop, "Substrates for zero temperature coefficient Love wave sensors," IEEE Transactions on Ultrasonics, Ferroelectrics, and Frequency Control, vol. 47, no. 3, pp. 701–705, 2000.

[37] B. Jakoby, J. Bastemeijer, and M. J. Vellekoop, "Temperature-compensated Love-wave sensors on quartz substrates," Sensors and Actuators, A: Physical, vol. 82, no. 1, pp. 83–88, 2000.

[38] B. Jakoby and M. Vellekoop, "Reducing the temperature sensitivity of Love-wave sensors," in 1998 IEEE Ultrasonics Symposium. Proceedings (Cat. No. 98CH36102), vol. 1, pp. 447–450, IEEE, 2011.

[39] F. Josse, F. Bender, and R. W. Cernosek, "Guided shear horizontal surface acoustic wave sensors for chemical and biochemical detection in liquids," Analytical Chemistry, vol. 73, no. 24, pp. 5937–5944, 2001.

[40] J. Du, G. L. Harding, J. A. Ogilvy, P. R. Dencher, and M. Lake, "A study of Love-wave acoustic sensors," Sensors and Actuators, A: Physical, vol. 56, no. 3, pp. 211–219, 1996.

[41] H.-K. Oh, W. Wang, K. Lee, C. Min, and S. Yang, " The development of a wireless Love wave biosensor on 41° YX LiNbO 3 ," Smart Materials and Structures, vol. 18, no. 2, p. 025008, 2009.

[42] M. Demiguel-Ramos, T. Mirea, J. Olivares, M. Clement, J. Sangrador, and E. Iborra, "Assessment of the acoustic shear velocity in SiO2 and Mo layers for acoustic reflectors," 2014 European Frequency and Time Forum, EFTF 2014, pp. 36–39, 2015.

[43] C. Viespe, V. Dinca, G. Popescu-Pelin, and D. Miu, "Love wave surface acoustic wave sensor with laser-deposited nanoporous gold sensitive layer," Sensors (Switzerland), vol. 19, no. 20, 2019.

[44] A. Rasmusson and E. Gizeli, "Comparison of Poly(methylmethacrylate) and Novolak waveguide coatings for an acoustic biosensor," Journal of Applied Physics, vol. 90, no. 12, pp. 5911–5914, 2001.

[45] Y. Q. Fu, J. K. Luo, N. T. Nguyen, A. J. Walton, A. J. Flewitt, X. T. Zu, Y. Li, G. McHale, A. Matthews, E. Iborra, H. Du, and W. I. Milne, "Advances in piezoelectric thin films for acoustic biosensors, acoustofluidics and lab-on-chip applications," Progress in Materials Science, vol. 89, pp. 31–91, 2017.

[46] M. Z. Aslam, V. Jeoti, S. Manzoor, M. Hanif, and M. Junaid, "An aluminium nitride based multilayer structure for Love mode surface acoustic wave devices," Semiconductor Science and Technology, vol. 35, no. 11, 2020.

[47] S. Li, Y. Wan, C. Fan, and Y. Su, "Theoretical study of monolayer and double-layer waveguide love wave sensors for achieving high sensitivity," Sensors (Switzerland), vol. 17, no. 3, 2017.

[48] B. Jakoby and M. Vellekoop, "Analysis and Optimization of Love Wave Liquid Sensors," IEEE Transactions on Ultrasonics, Ferroelectrics, and Frequency Control, vol. 45, no. 5, pp. 1293–1302, 1998.

[49] D. Smith and J. Johnson, "Surface-acoustic-wave directional coupler for apodization of integrated acoustooptic filters," IEEE Transactions on Ultrasonics, Ferroelectrics and Frequency Control, vol. 40, pp. 22–25, 1 1993.

[50] A. Mamishev, K. Sundara-Rajan, Fumin Yang, Yanqing Du, and M. Zahn, "Interdigital sensors and transducers," Proceedings of the IEEE, vol. 92, pp. 808–845, 5 2004.

[51] H. Nakamura, T. Yamada, T. Ishizaki, and K. Nishimura, "A new design concept for low-loss SAW filters based on different-width split-finger SPUDT," IEEE Transactions on Microwave Theory and Techniques, vol. 49, no. 4 II, pp. 761–768, 2001.

[52] S. Lehtonen, V. P. Plessky, C. S. Hartmann, and M. M. Salomaa, "SPUDT filters for the 2.45 GHz ISM band," IEEE Transactions on Ultrasonics, Ferroelectrics, and Frequency Control, vol. 51, no. 12, pp. 1697–1702, 2004.

[53] C. Fu, K. Lee, K. Lee, S. S. Yang, and W. Wang, "A stable and highly sensitive strain sensor based on a surface acoustic wave oscillator," Sensors and Actuators, A: Physical, vol. 218, pp. 80–87, 2014.

[54] T. Kodama, H. Kawabata, H. Sato, and Y. Yasuhara, "Design of low–loss saw filters employing distributed acoustic reflection transducers," Electronics and Communications in Japan (Part II: Electronics), vol. 70, no. 9, pp. 32–44, 1987.

[55] T. T. Wu, H. T. Tang, Y. Y. Chen, and P. L. Liu, "Analysis and design of focused interdigital transducers," IEEE Transactions on Ultrasonics, Ferroelectrics, and Frequency Control, vol. 52, no. 8, pp. 1384–1392, 2005.

[56] M. S. Kharusi and G. W. Farnell, "On Diffraction and Focusing in Anisotropic Crystals," Proceedings of the IEEE, vol. 60, no. 8, pp. 945–956, 1972.

[57] M. M. De Lima, F. Alsina, W. Seidel, and P. V. Santos, "Focusing of surface-acoustic-wave fields on (100) GaAs surfaces," Journal of Applied Physics, vol. 94, no. 12, pp. 7848–7855, 2003.

[58] R. J. Ablin, W. A. Soanes, P. Bronson, and E. Witebsky, "Precipitating antigens of the normal human prostate," Reproduction, vol. 22, pp. 573–574, 8 1970.

[59] W. J. Catalona, "History of the discovery and clinical translation of prostate-specific antigen," Asian Journal of Urology, vol. 1, no. 1, pp. 12–14, 2014.

[60] J. T. Wei, "Urinary biomarkers for prostate cancer," Current Opinion in Urology, vol. 25, pp. 77–82, 1 2015.

[61] P. Harvey, A. Basuita, D. Endersby, B. Curtis, A. Iacovidou, and M. Walker, "A systematic review of the diagnostic accuracy of prostate specific antigen," BMC Urology, vol. 9, no. 1, pp. 1–9, 2009.

[62] K. B. Donald-Buri, K. Campus, K. Patel, S. Lecturer, E. N. Fish, B. Donald-buri, and P. Musau, "Evaluating Engrailed-2 and cytokines in urine with serum PSA as potential biomarkers in patients with prostatism," Tech. Rep. 12, 2016.

[63] F. F. Coelho, F. L. Guimarães, W. L. R. Cabral, P. G. O. Salles, E. C. Mateo, L. M. Nogueira e Nogueira, C. E. C. Fonseca, and K. B. Gomes, "Expression of PCA3 and PSA genes as a biomarker for differential diagnosis of nodular hyperplasia and prostate cancer.," Genetics and molecular research : GMR, vol. 14, pp. 13519–13531, 10 2015.

[64] C.-C. Chang, Y.-C. Lee, H.-W. Tsai, S.-C. Yii, T.-H. Yen, and F.-Y. Chu, "Diagnostic Role of Serum Free-to-Total Prostate Specific Antigen (PSA) Ratio in Prostate Cancer with Serum Total Concentration of PSA below 4 ng/mL.," Asian Pacific journal of cancer prevention : APJCP, vol. 16, no. 13, pp. 5261–5264, 2015.

[65] S. Agnihotri, R. D. Mittal, R. Kapoor, and A. Mandhani, "Raising cut-off value of prostate specific antigen (PSA) for biopsy in symptomatic men in India to reduce unnecessary biopsy.," The Indian journal of medical research, vol. 139, pp. 851–856, 6 2014.

[66] S. S. Salami, F. Schmidt, B. Laxman, M. M. Regan, D. S. Rickman, D. Scherr, G. Bueti, J. Siddiqui, S. A. Tomlins, J. T. Wei, A. M. Chinnaiyan, M. A. Rubin, and M. G. Sanda, "Combining urinary detection of TMPRSS2:ERG and PCA3 with serum PSA to predict diagnosis of prostate cancer.," Urologic oncology, vol. 31, pp. 566–571, 7 2013.

[67] Q. Li, S. Lu, X. Li, G. Hou, L. Yan, W. Zhang, and B. Qiao, "Biological function and mechanism of miR-33a in prostate cancer survival and metastasis: via downregulating Engrailed-2," Clinical and Translational Oncology, vol. 19, no. 5, pp. 562–570, 2017.

[68] R. Morgan, A. Boxall, A. Bhatt, M. Bailey, R. Hindley, S. Langley, H. C. Whitaker, D. E. Neal, M. Ismail, H. Whitaker, N. Annels, A. Michael, and H. Pandha, "Engrailed-2 (EN2): A tumor specific urinary biomarker for the early diagnosis of prostate cancer," Clinical Cancer Research, vol. 17, no. 5, pp. 1090–1098, 2011.

[69] M. P. Marszałł, W. Sroka, M. Adamowski, P. Słupski, P. Jarzemski, J. Siódmiak, and G. Odrowąż-Sypniewska, "Engrailed-2 protein as a potential urinary prostate cancer biomarker: a comparison study before and after digital rectal examination.," European journal of cancer prevention : the official journal of the European Cancer Prevention Organisation (ECP), vol. 24, pp. 51–56, 1 2015.

[70] J. Do Carmo Silva, S. Vesely, V. Novak, H. Luksanova, R. Prusa, and M. Babjuk, "Is Engrailed-2 (EN2) a truly promising biomarker in prostate cancer detection?," Biomarkers, vol. 25, pp. 34–39, 1 2019.

[71] E. Gómez-Gómez, J. M. Jiménez-Vacas, S. Pedraza-Arévalo, F. López-López, V. Herrero-Aguayo, D. Hormaechea-Agulla, J. Valero-Rosa, A. Ibáñez-Costa, A. J. León-González, R. Sánchez-Sánchez, T. González-Serrano, M. J. Requena-Tapia, J. P. Castaño, J. Carrasco-Valiente, M. D. Gahete, and R. M. Luque, "Clinical Medicine Oncogenic Role of Secreted Engrailed Homeobox 2 (EN2) in Prostate Cancer," mdpi.com, 2019.

[72] E. Killick, R. Morgan, F. Launchbury, E. Bancroft, E. Page, E. Castro, Z. Kote-Jarai, A. Aprikian, I. Blanco, V. Clowes, S. Domchek, F. Douglas, D. Eccles, D. G. Evans, M. Harris, J. Kirk, J. Lam, G. Lindeman, G. Mitchell, N. Pachter, C. Selkirk, K. Tucker, J. Zgajnar, R. Eeles, and H. Pandha, "Role of Engrailed-2 (EN2) as a prostate cancer detection biomarker in genetically high risk men," Scientific Reports, vol. 3, pp. 1–5, 2013.

[73] H. Pandha, K. D. Sorensen, T. F. Orntoft, S. Langley, S. Hoyer, M. Borre, and R. Morgan, "Urinary engrailed-2 (EN2) levels predict tumour volume in men undergoing radical prostatectomy for prostate cancer," BJU International, vol. 110, no. 6B, pp. 287–292, 2012.

[74] F. Sanguedolce, A. Cormio, M. Brunelli, A. D'Amuri, G. Carrieri, P. Bufo, and L. Cormio, "Urine TMPRSS2: ERG Fusion Transcript as a Biomarker for Prostate Cancer: Literature Review.," Clinical genitourinary cancer, vol. 14, pp. 117–121, 4 2016.

[75] J. N. Eskra, D. Rabizadeh, C. P. Pavlovich, W. J. Catalona, and J. Luo, "Approaches to urinary detection of prostate cancer," Prostate Cancer and Prostatic Diseases, vol. 22, pp. 362–381, 9 2019.

[76] N. B. Delongchamps, P. Younes, L. Denjean, M. Zerbib, and P.-N. Bories, "TMPRSS2-ERG fusion transcripts expression in patients referred for prostate biopsy: combining detection in urine and needle rinse material.," World journal of urology, vol. 33, pp. 807–811, 6 2015.

[77] K. Fujita and N. Nonomura, "Urinary biomarkers of prostate cancer," International Journal of Urology, vol. 25, no. 9, pp. 770–779, 2018.

[78] P.-N. Bories, P. Younes, M. Zerbib, L. Denjean, T. Popovici, L. Cynober, and N. B. Delongchamps, "TMPRSS2-ERG fusion transcripts in matched urine and needle rinse material after biopsy for the detection of prostate cancer.," Clinical chemistry, vol. 59, pp. 245–251, 1 2013.

[79] S. S. Salami, F. Schmidt, B. Laxman, M. M. D. Regan, D. S. Rickman, D. Scherr, G. Bueti, J. Siddiqui, S. A. Tomlins, J. D. T. Wei, A. M. Chinnaiyan, M. A. Rubin, and M. G. Sanda, "Combining urinary detection of TMPRSS2:ERG and PCA3 with serum PSA to predict diagnosis of prostate cancer," 2013.

[80] R. Sabaliauskaite, S. Jarmalaite, D. Petroska, D. Dasevicius, A. Laurinavicius, F. Jankevicius, and J. R. Lazutka, "Combined analysis of TMPRSS2-ERG and TERT for improved prognosis of biochemical recurrence in prostate cancer," Genes Chromosomes and Cancer, vol. 51, pp. 781–791, 8 2012.

[81] P. N. Nguyen, P. Violette, S. Chan, S. Tanguay, W. Kassouf, A. Aprikian, and J. Z. Chen, "A panel of TMPRSS2:ERG fusion transcript markers for urine-based prostate cancer detection with high specificity and sensitivity," European Urology, vol. 59, no. 3, pp. 407–414, 2011.

B

Flow Chart

B.1. Starting material

Use 500 µm ST-cut Quartz wafer, at least single side polished with the following specification:

Type:	Quartz
Orientation:	ST
Thickness	500 µm
Diameter	100 mm
Finishing	Double side polished (single side polished is also possible)

Processing steps:

1. Cleaning
2. Aluminium sputtering
3. Cleaning
4. Etching
5. Cleaning
6. PMMA spinning
7. Dicing
8. Plasma Etching for surface activation
9. Wire Bonding
10. Transport

1. Wafer Cleaning – SAL lab Location: Wet benches SAL 5- Location of HNO3.
   (a) Prepare in a polymer beaker a HNO3 (99%) bath, enough to submerge all the wafers
   (b) prepare a beaker with DI-water, enough to submerge all the wafers
   (c) Place the wafers in the wafer holder
   (d) submerge the wafers into the beaker for 10 minutes
   (e) After ten minutes, rinse the wafers in DI-water for 10-15 minutes
   (f) Use the spinner to dry the wafers
   (g) . Safely store the solution in a fume hood (don't forget to label it) since we will have to reuse it after metalization (if the metalization is done right after this step). Allowed time to keep the chemical in this area is max 2 days. After this time, you have to drain and clean the chemicals.
2. Metalization (Trikon Sigma 204 Dealer): 50nm pure Al Since we are using pure Aluminum, check with Johannes van Wingerden that this is loaded in depB (not a standard source material).
   (a) Check that the cassette is free to use and the cassette chamber is at atmospheric pressure. Completely open the door so that the arm has enough space to come out of the chamber
   (b) Check if the machine has been used in the last two hours. If this is not the case, place a dummy wafer in the first slot.
   (c) Since quartz wafers are used, manual selection of the wafers need to be used. Make sure this is done for you beforehand.
   (d) Take the cassette off the shelf and put the wafers in the slots. Make sure that the back sides are facing the H-tube.
   (e) Use the wafer aligner such that all primary flats are facing downwards
   (f) Put the cassette back onto the shelve and make sure it is placed correctly
   (g) On the screen, load the cassette and close the door.
   (h) . If a dummy wafer is included, select for the first wafer the recipe _TargetClean_350C
   (i) Deposit 50 nm pure Al at 350 °C.
   (j) Once all the wafers are done, eject the wafers and wait for the message that it is okay to open the door
   (k) Remove the wafers back to the corresponding wafer box. Do a visual inspection.
   (l) Put the cassette back onto the shelf and once it is placed correctly load the cassette on the screen
   (m) Close the door manually
   (n) Abort all used blocks
   (o) Once the message "abort" is shown, click on the control block and set all used blocks to idle
   (p) Log off
3. Wafer Cleaning – SAL lab. Location: Wet benches SAL 5- Location of HNO3.
   (a) Take the solution made in step 1
   (b) prepare a beaker with DI-water, enough to submerge all the wafers
   (c) Place the wafers in the wafer holder
   (d) submerge the wafers into the beaker for 10 minutes
   (e) After ten minutes, rinse the wafers in DI-water for 10-15 minutes
   (f) Once done, place the wafers back in the cassette
   (g) Use the spinner to dry the wafers
   (h) The same cleaning steps will be done later on in the process (step 9). If possible, safely store the beaker under the fume hood for later use (don't forget to label it). Otherwise dispose of the HNO3 using the water jet system. Allowed time to keep the chemical in this area is max 2 days. After this time, you have to drain and clean the chemicals.

4. Photo resist coating (EVG120 Coater-developer):
   (a) Check if the relative humidity is (48 ± 2
   (b) Put the wafers in the carrier labeled coater. To avoid scratching, let the polished side of the first wafer face the frontside and put it in a slot. Do the same for the other wafers working backwards (counting the slots down to 1 until you have no wafers left)
   (c) Align the wafers with the aligner. Make sure that the primary flats are all facing upwards
   (d) Deposit the carrier on the machine. Make sure it is placed correctly and that it is stable by wobbling it
   (e) On the computer, load the coater and select the slot with wafers in them
   (f) Select the 1_Co - 3012 - 1,4µm 1_Co - 3027 – 2.3 µm Recipe
   (g) Press OK to start coating process
   (h) Once the machine is done, take the carrier and put the wafers back with your own carrier
5. Alignment and exposure ('SUSS MicroTec MA/BA8 mask aligner)
   (a) For this process only one mask will be used so there is no zero layer or alignment marks necessary
   (b) Load the Mask in the machine
   (c) Use Front side exposure with hard contact
   (d) We are going to expose 1,4µm SPR3012 2.3 µm 3027 Calculate the exposure time by consulting the contact aligner exposure energy data log
6. Development (EVG120 Coater-developer)
   (a) Repeat process step for photo resist coating, but now use the developer cassette. The process consists of a post-exposure bake at 115 °C for 90 seconds, developing with Shipley MF322 with a single puddle process, and a hard bake at 100 °C for 90 seconds.
   (b) Use program "1-Dev - SP".
7. Aluminium wet etching – wet bench Etching line- CR100- Al etching at 35 degrees
   (a) Use at the wet bench the Aluminum etch bath
   (b) Load the wafers in the corresponding wafer holder
   (c) Take the wafers out and dip the wafers in the etchant for 20 seconds. 50 nm of aluminum will be lost
   (d) Rinse in di-water bath and start the program
8. Photoresist removal – wet bench acetone bath
   (a) Move the wafers into the acetone wafer holder
   (b) Drop the wafers in 40 degree acetone
   (c) submerge the wafers for 1 minute in the acetone beaker to dissolve the photoresist
   (d) Slowly take out the wafers and air dry the acetone off.
9. Wafer cleaning: HNO3 99% metal. Location: Wet benches SAL 5- Location of HNO3
   (a) Place the wafers in the wafer holder
   (b) submerge the wafers into the HNO3 bath for 10 minutes
   (c) in the meantime, fill a bin with diwater
   (d) After ten minutes, rinse the wafers in DI-water for 10-15 minutes
   (e) Once done, place the wafers back in the cassette
   (f) Use the spinner to dry the wafers
   (g) If necessary, dispose of the HNO3 using the water jet system

10. IDT dimension measurement: SEM tool
    (a) Place the wafers in the SEM microscope
    (b) Sample different IDT fingers and measure their thickness, to validate the production process.
11. Dicing with a scriber – MEMS lab
    (a) Dice the wafer in chips of 10x10mm in the wafer dicer
    (b) Rinse the chips with di-water and dry with a nitrogen gun
12. PMMA deposition (480 nm, Manual spinner and bake plate) - Polymer Lab:
    (a) Stick a chip with the backside onto a carrier wafer with double-sided carbon tape
    (b) Dispense 1 mL of PMMA/anisole solution in a clean beaker
    (c) Start the spinner and log in
    (d) Load recipe: 1400 rpm for 30 seconds, 500rpm/s ramp
    (e) Place the carrier wafer with the chip on the chuck and make sure the wafer is centered
    (f) Dispense PMMA/anisole solution on the wafer and start the spinning process
    (g) After spinning, cure the PMMA on the baker plate with the following parameters
        i. Hard contact
        ii. Temperature: 100 degrees C
        iii. Time: 1 minutes
    (h) Remove the chip from the carrier wafer
    (i) Remove wafer and repeat process for next wafers
13. Etching of PMMA at contact pads – MEMS lab
    (a) Fill a beaker with acetone
    (b) Take the chips with a tweezer and carefully submerge the top and bottom part just a bit such that the only the contact pads are exposed. Keep it for 1 minute in this position
    (c) Try with a dummy device if it is also possible to use droplets of acetone locally which is followed by a demi water rinse

    The Following steps will be done in batches, to avoid too much time between surface activation and biochemical coupling. The following steps should be done within 24 hours. If after the first batch it shows that more can be done in one day than feel free to do just that
14. Surface activation – Polymer lab
    (a) Use the ATTO low plasma tool in the polymer lab. Follow the manual for the correct setup
    (b) Put each individual chip on a carrier wafer with double-side Kapton tape
    (c) 3. Parameters:
        i. Operating frequency 40kHz
        ii. Power: 200 W
        iii. Pressure 75 Pa
        iv. Exposure time: 10s
15. Wire bonding and packaging – MEMS lab
    (a) Use double sided tape to fix the sensor chips to the PCB
    (b) Using the PCB connection drawing, connect the SAW connection pads to those of the PCB
16. Transport to Erasmus
    (a) Put the PCB's in a box and go immediately by train to the Erasmus MC Lab for further processing

C

Spectrum Analyzer Results

C.1. 400MHz input

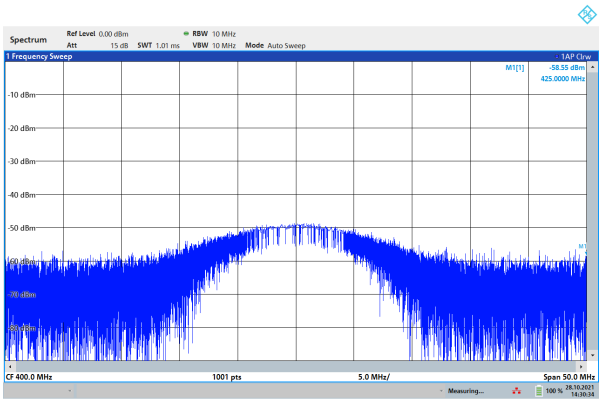

50-5000

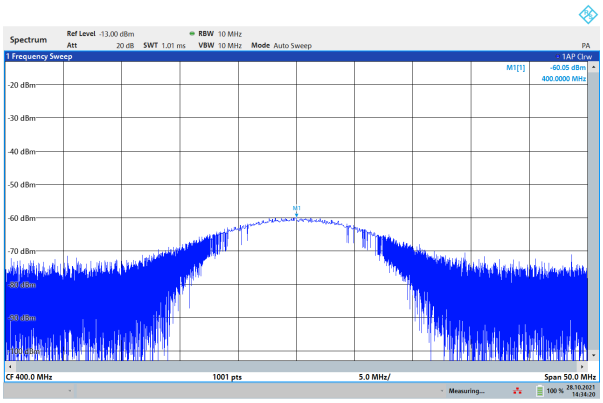

25-1000

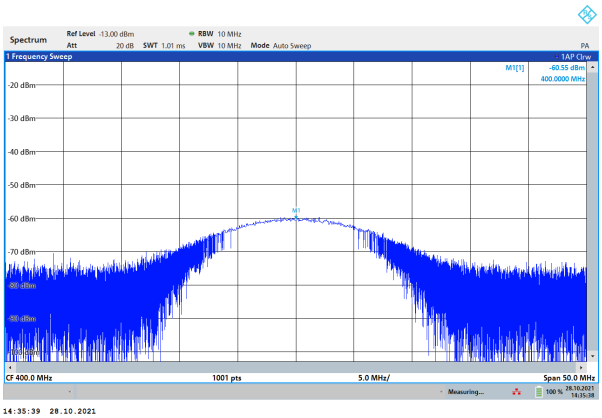

(a) 50-500

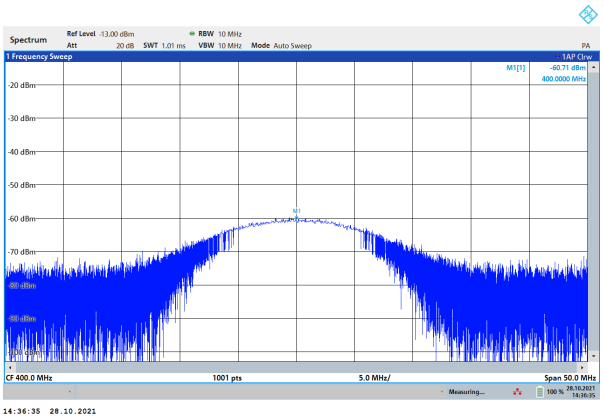

75-1000

C.2. 900MHz input frequency

C.3. 1.4GHz input frequency

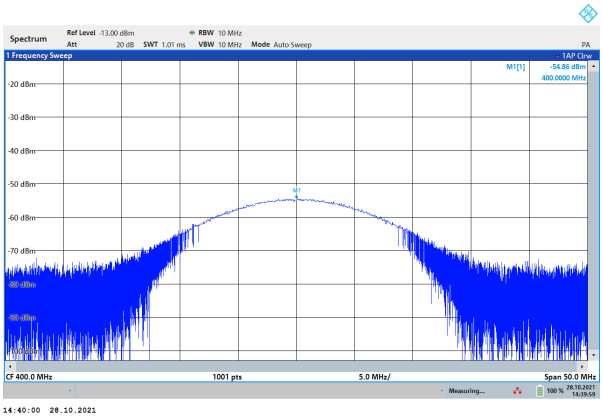

25-5000

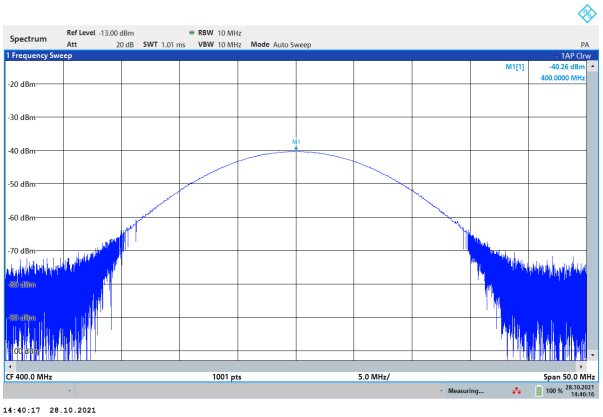

25-5000

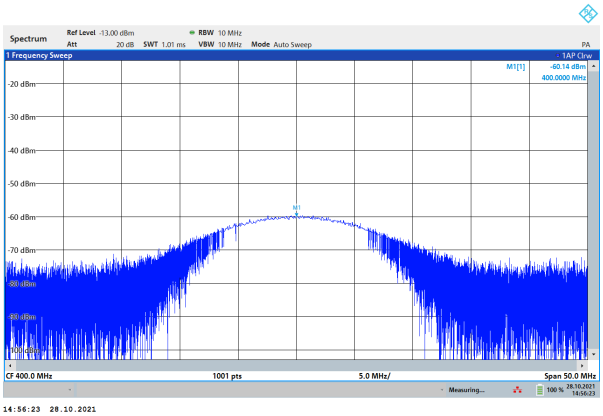

25-5000

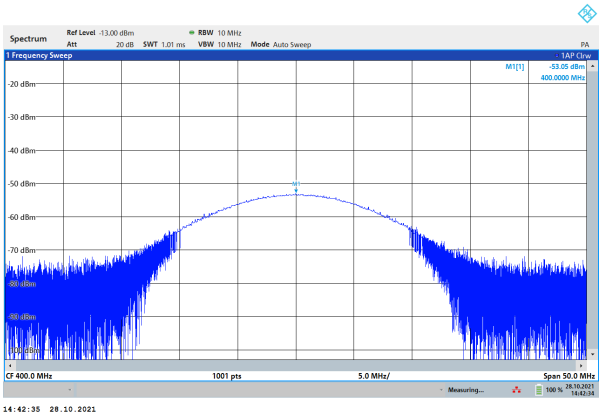

75-5000

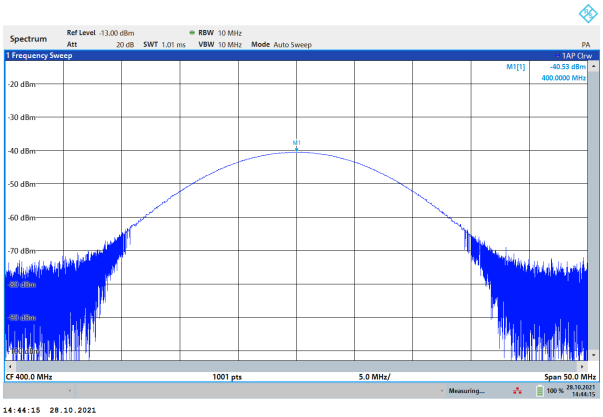

75-5000

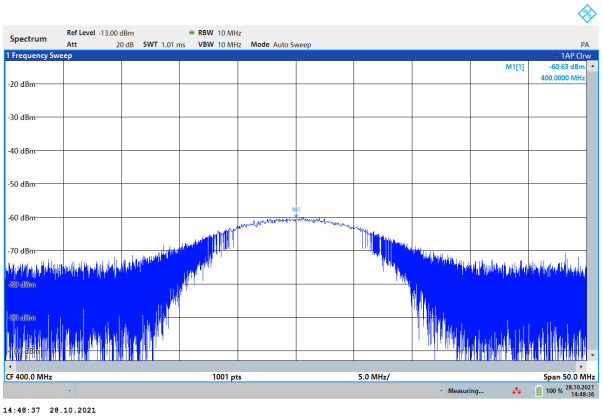

75-500

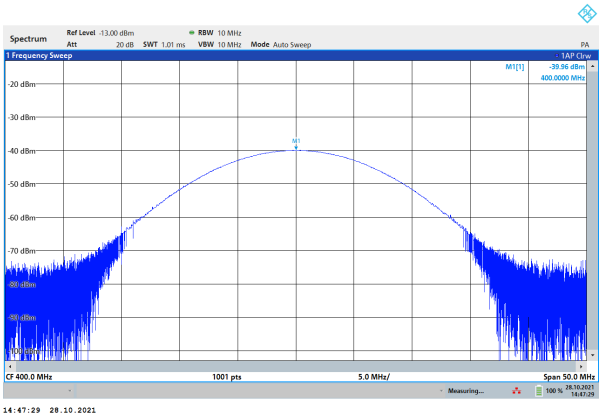

75-500

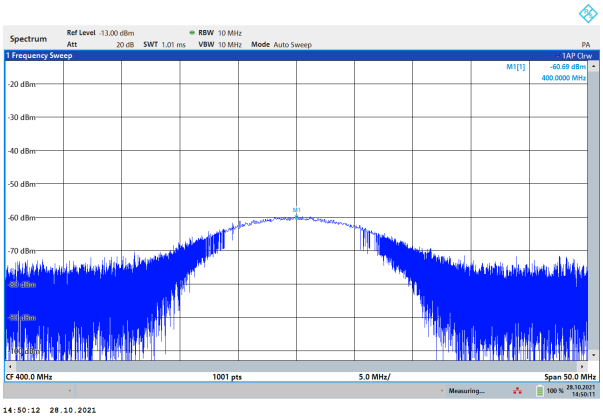

50-1000

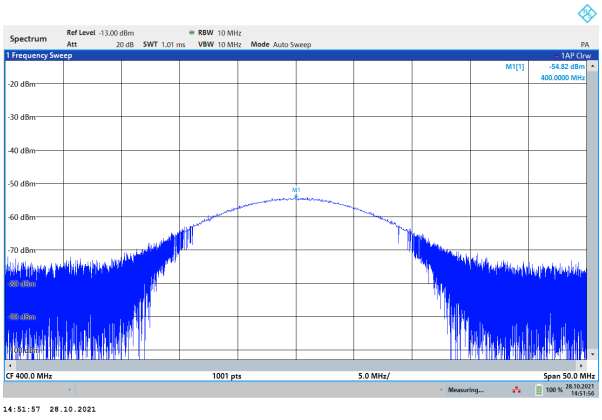

50-1000

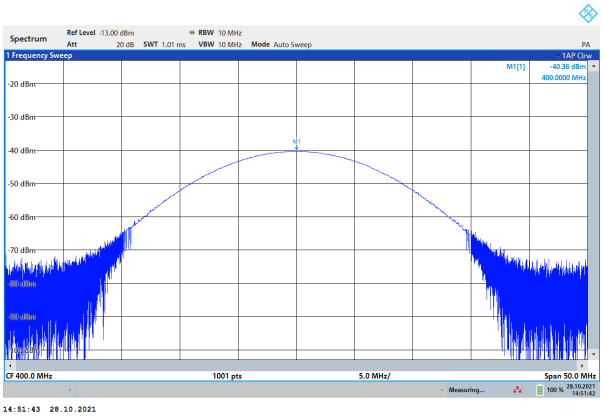

50-1000

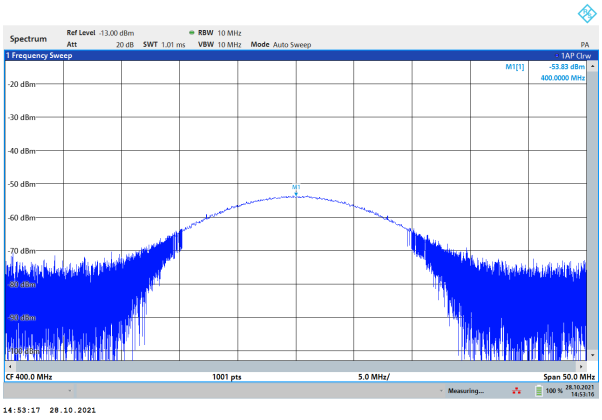

25-500

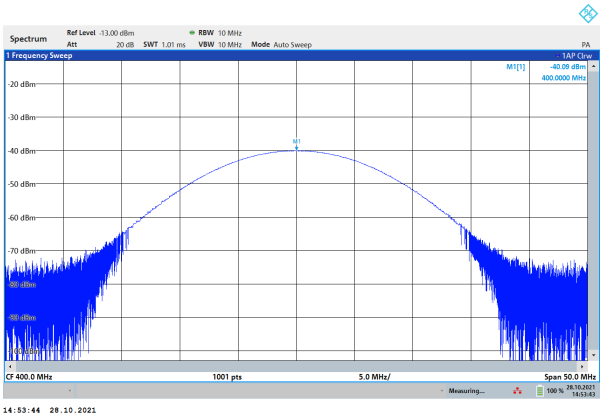

25-500

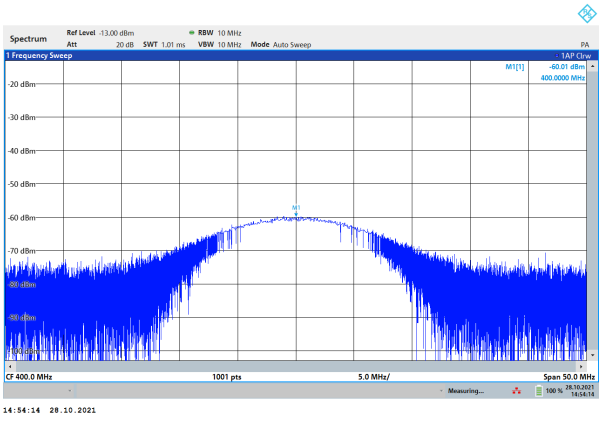

25-500

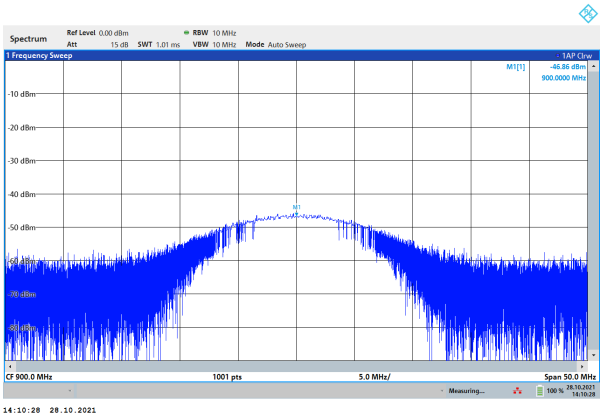

50-5000

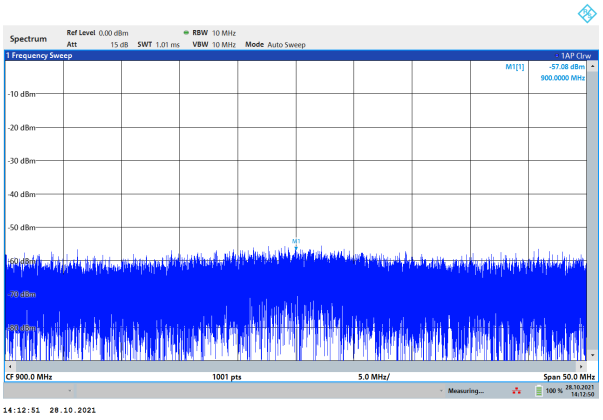

25-1000

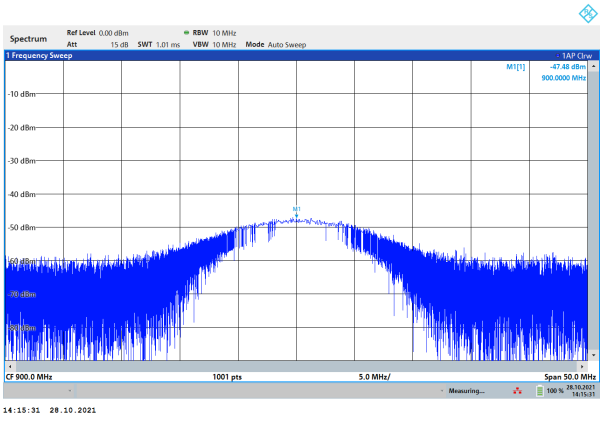

(a) 50-500

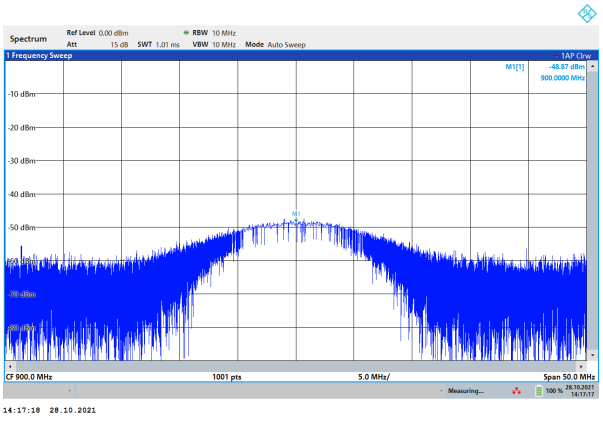

75-1000

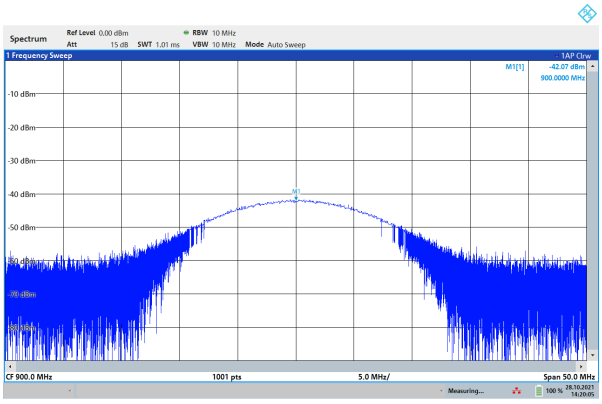

25-5000

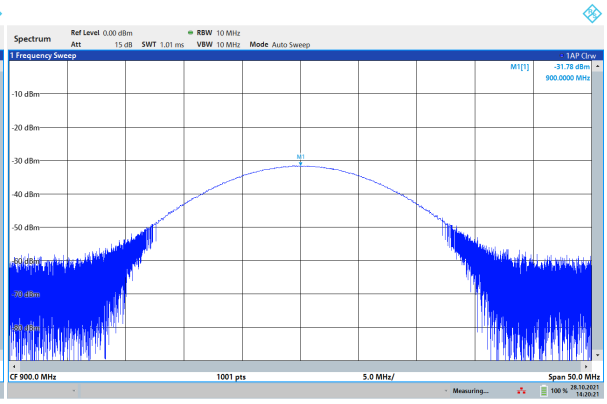

25-5000

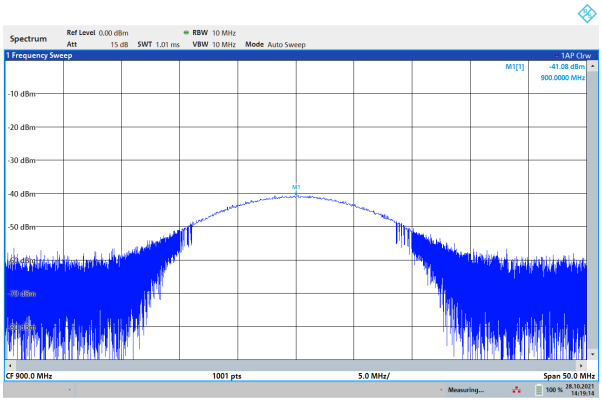

25-5000

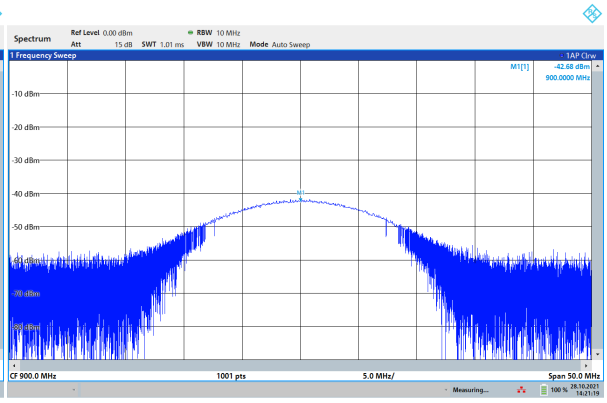

75-5000

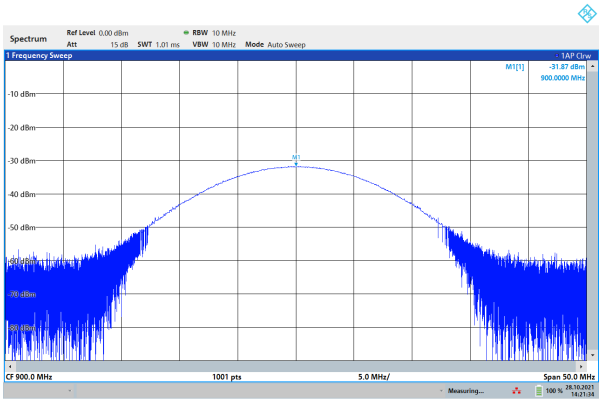

75-5000

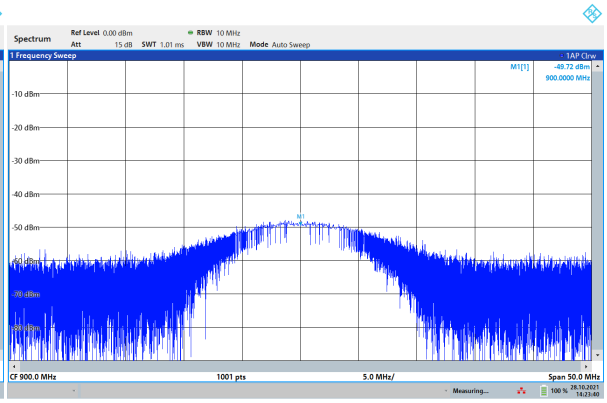

75-500

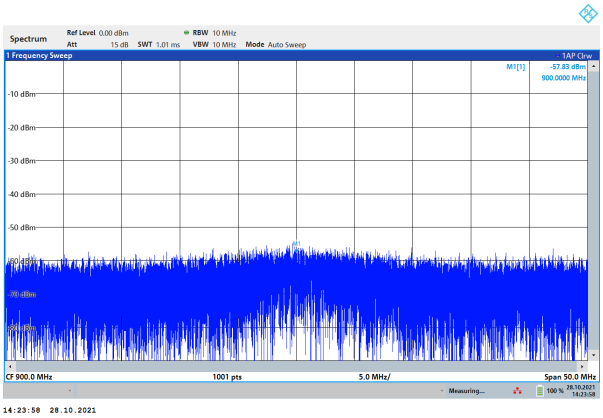

75-500

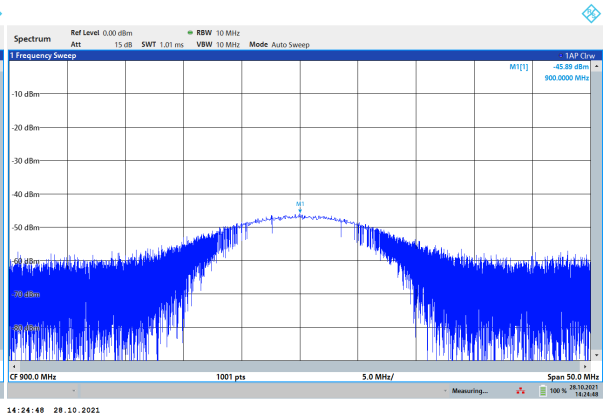

50-1000

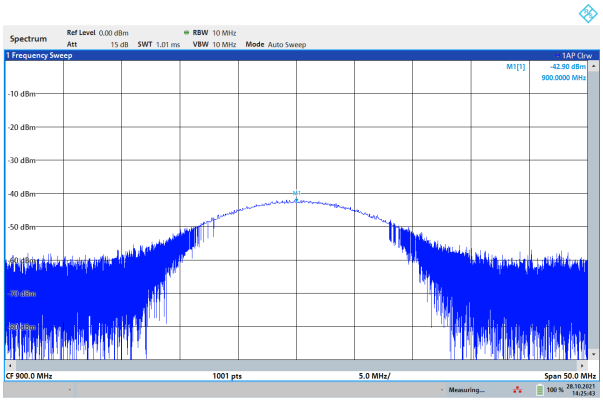

50-1000

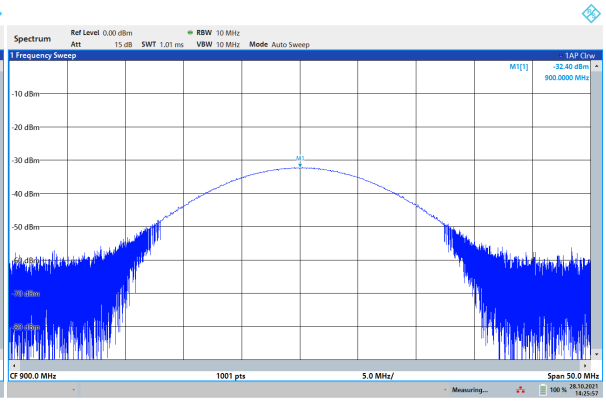

50-1000

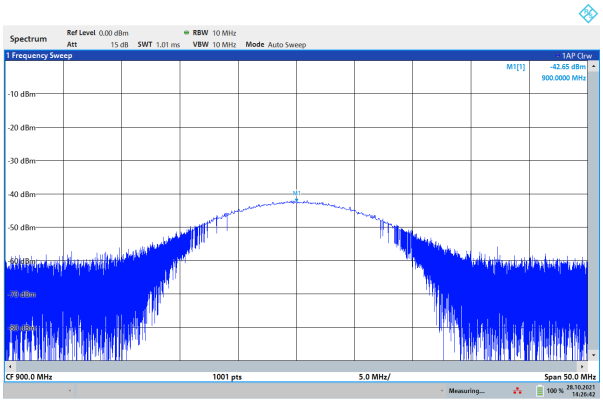

25-500

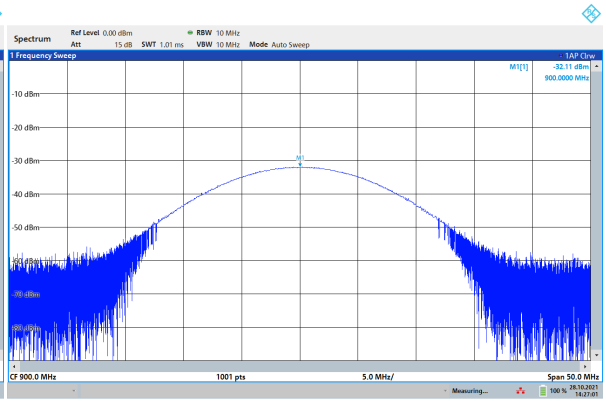

25-500

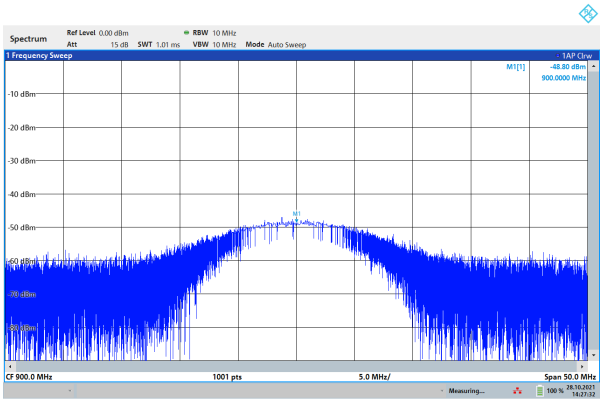

25-500

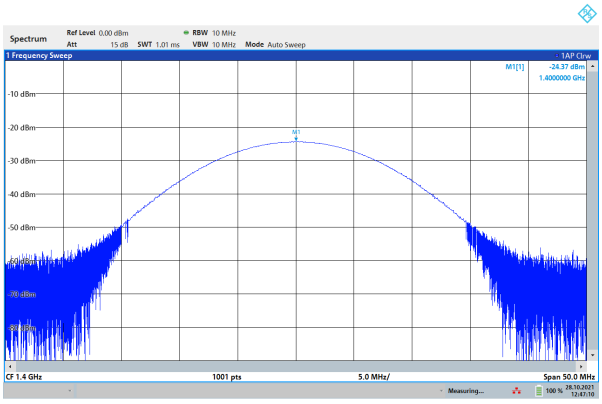

50-5000

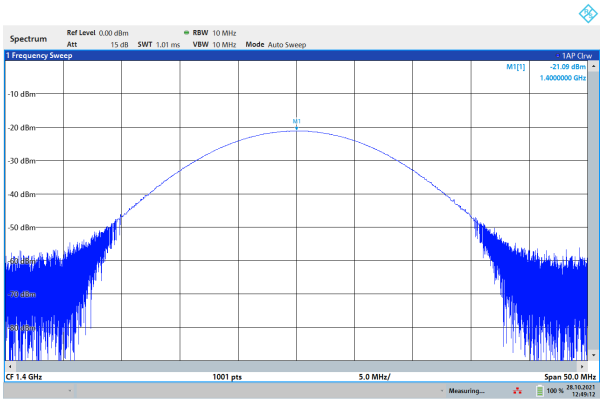

25-1000

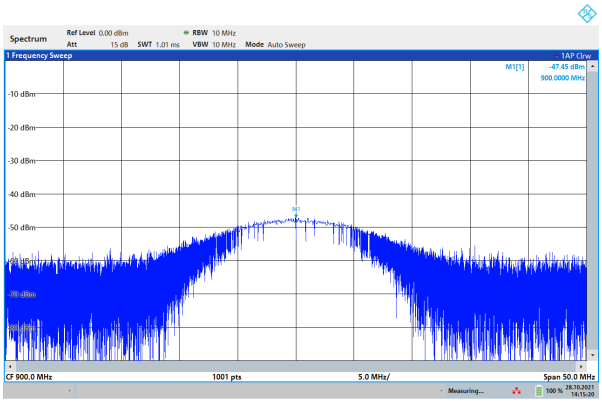

(a) 50-500

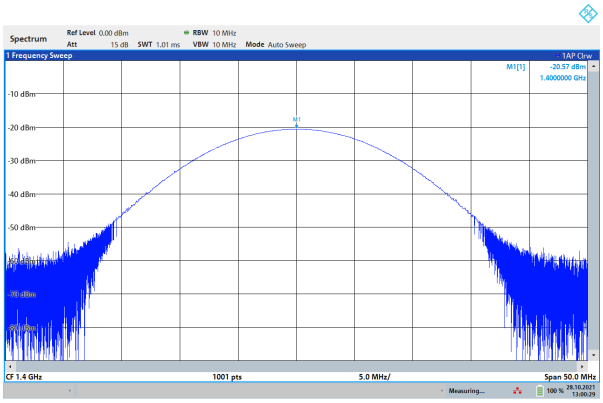

75-1000

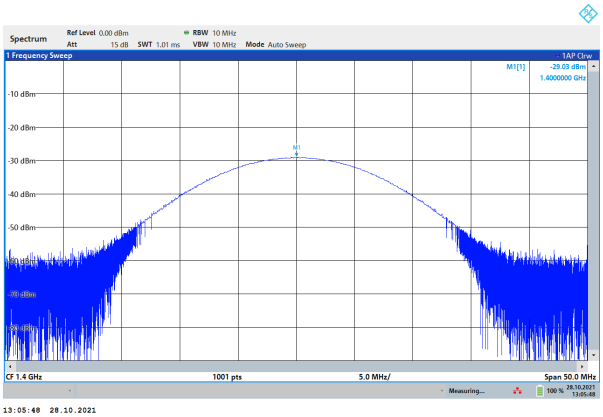

25-5000

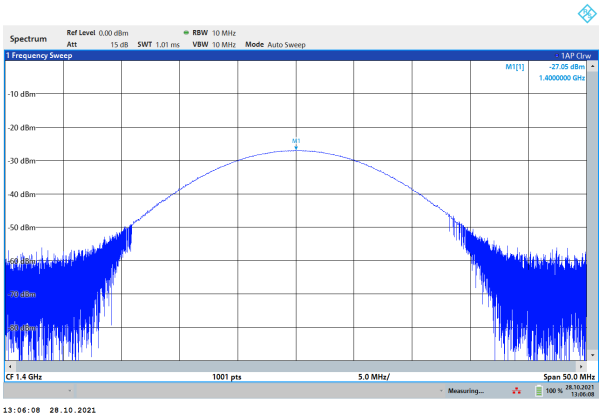

25-5000

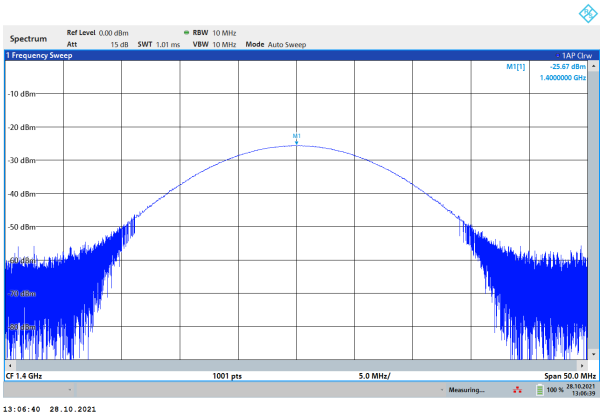

25-5000

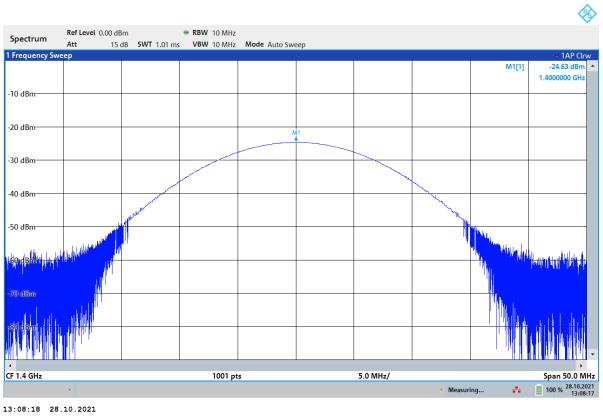

75-5000

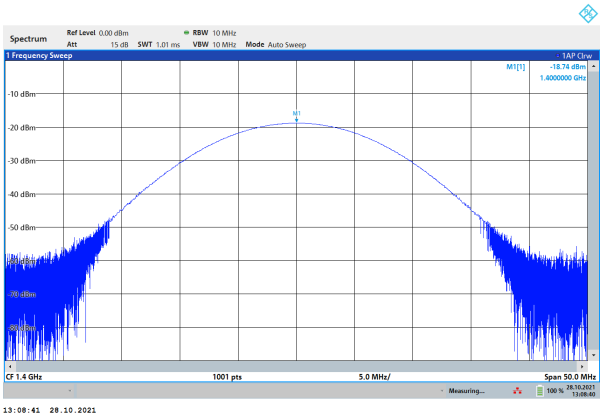

75-5000

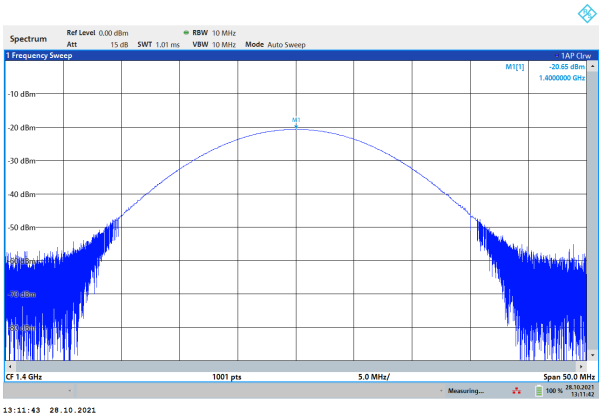

75-500

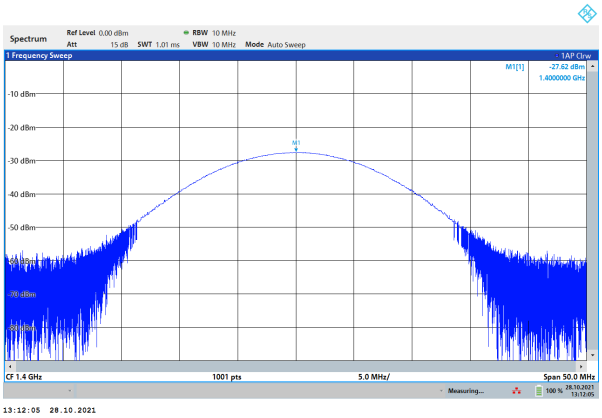

75-500

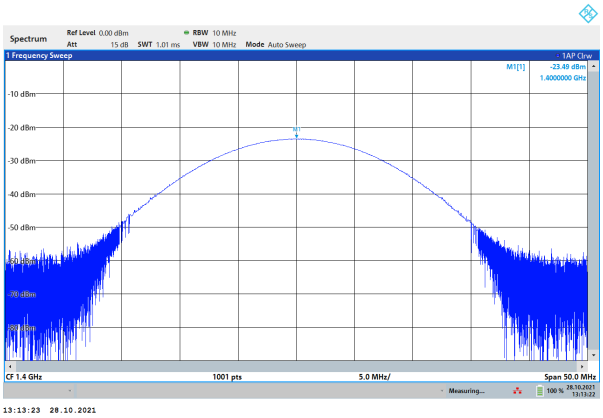

50-1000

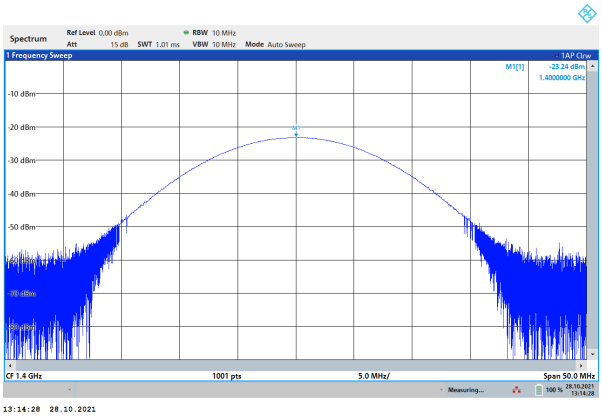

50-1000

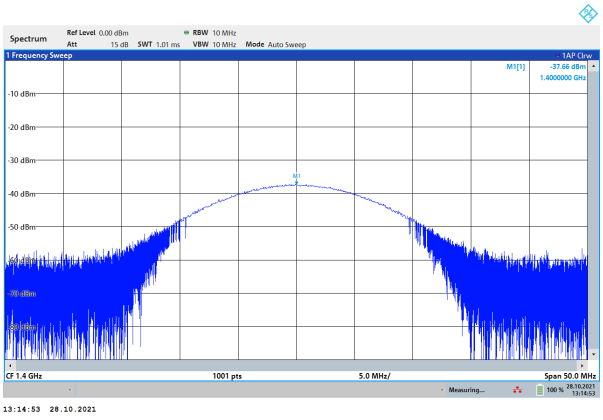

50-1000

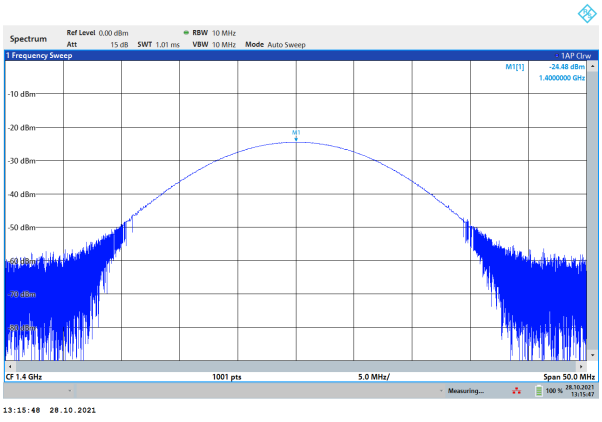

25-500

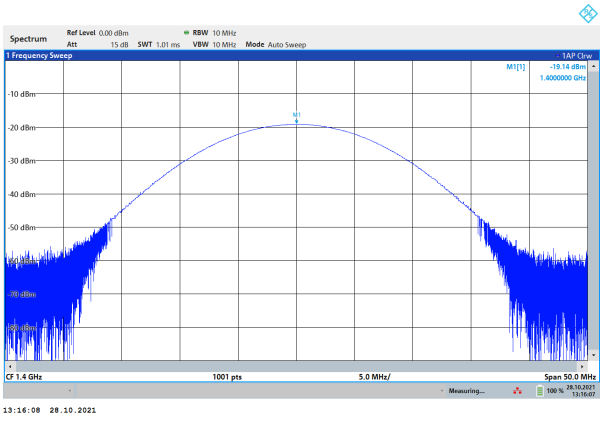

25-500

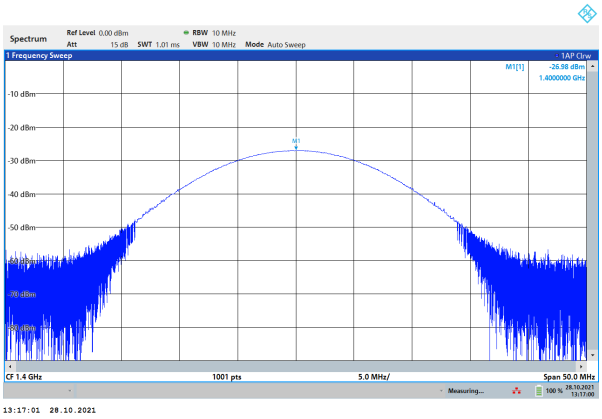

25-500